SELECTIVE MODE EXCITATION IN SPECIALTY WAVEGUIDES USING MICRO OPTICAL ELEMENTS

by

WALEED SOLIMAN MOHAMMED
B.S. Cairo University, 1996
M.S. Cairo University, 1999
M.S. University of Central Florida, 2001

A dissertation submitted in partial fulfillment of the requirements
for the degree of Doctoral of Optics
in the College of Optics and Photonics/CREOL
at the University of Central Florida
Orlando, Florida

Fall Term
2004

ABSTRACT

Although optical fibers and specialty waveguides are the base of majority of today's telecom and light delivery applications, fabrication deformation, nonlinearity and attenuation limit the bandwidth of the data being transmitted or the amount of power carried by these systems. One-way to overcome these limitations without changing the fibers design or fabrication is to engineer the input light in order to excite a certain mode or a group of modes with unique optical properties. Diffractive and micro optics are highly effective for selectively coupling light to specific modes. Using micro optics, mode selective coupling can be achieved through several matching schemes: phase only, phase and amplitude, or phase, amplitude and polarization. The main scope of this work is the design and fabrication of novel optical elements that overcome the limitations of these light delivery systems, as well as the characterization and analysis of their performance both experimentally and using numerical simulation.

To my parents

ACKNOWLEDGMENTS

First, I would like to acknowledge my advisor, Dr. Eric Johnson, for all the help and support during the years of my Ph.D. work. I was lucky to start with him from scratch. I have learned a lot during the establishment of our labs. But the memories of the empty lab with a table in there still have their own beauty.

I would like also to thank from inside my heart the people who became close to me and made these years much easier specially: Sakoolkan Boonruang, Robert Iwanow, Fumiyo Yoshino, Martina Atanassova, Ference Szcepoc, Mahesh Pitchumani, Te-Yuan Chung, Mohamed Abdel Rahman, Amar Amouri, Camilo Lopez, George Siganakis, Adela Apostol, Erdem Ultrain, and Bojan Resan.

TABLE OF CONTENTS

LIST OF FIGURES

LIST OF TABLES

LIST OF ACRONYMS/ABBREVIATIONS

AVA	Automatic Variable Aperture
BAA	Beam Acceptance Aperture
CCD	Charge-Coupled Device
EBL	Electron Beam Lithography
EBPG	Electron Beam Pattern Generator
FD-BPM	Finite Difference Beam Propagation Method
FIB	Focused Ion Beam
HGW	Hollow-Glass Waveguide
HWHM	Half Width Half Maximum
ICP	Inductively Coupled Plasma
IPA	Isopropanole
IR	Infra-Red
LMIS	Liquid Metal Ion Source
LP	Linearly Polarized
MCF	Multicore Fiber
MIBK	Methyl Isobutyl Ketone
MMF	Multimode Fiber
MOP	Method Of Projection
PCF	Photonic Crystal Fiber

PMMA	Polymethyl Methacrylate
PR	Photo-Resist
RIE	Reactive Ion Etching
SEM	Scanning Electron Microscope
SMF	Single Mode Fiber
SMM	Scattering Matrix Method
STEM	Scanning Transmission Electron Microscope
TE	Transverse Electric
TEM	Transmission Electron Microscope
TM	Transverse Magnetic
UV	Ultra Violet

CHAPTER ONE: INTRODUCTION

In 1930 Heinrich Lamm was the first to report the transmission of light through a bundle of transparent rods. His work was followed by several experiments by Holger Moeller in 1951 and Abraham van Heel in 1954. All early fibers were bare. Van Heel was the first to introduce the cladding region. By 1960, glass-clad fiber had an attenuation of 1 decibel per meter. Since the demonstration of the first low-loss optical fiber in 1972 by Corning Glass Works, there has been a continuous stream of technological improvements designed to reduce impairments due to propagation loss, nonlinearity and dispersion. This stream of fiber technology led the industry from multimode fibers to single mode fibers, and on to specialty fibers.

Specialty fibers are defined as optical fibers designed to have special functions that are different from standard telecommunication fibers. Unique materials and fiber structures along with new processing techniques allowed the refractive index to vary across the fiber, to have several cores combined within the same cladding, and air core fibers to be coated with thin layers of metal/dielectric. Examples of specialty fibers are: graded index fiber, polarization maintaining fiber, multi core fiber, hollow waveguides and photonic crystal fibers.

When guiding light in these specialty fibers, the light propagates in different modes. Each mode is characterized by its amplitude, phase and polarization profile. Some of these modes have unique properties that can be useful for certain applications such as

telecommunication and light delivery systems. Therefore, it is important to develop modeling techniques to investigate the modal properties of these fibers. Accordingly, several studies have been carried out in modeling the light propagating inside different specialty fibers as well as their modal properties.

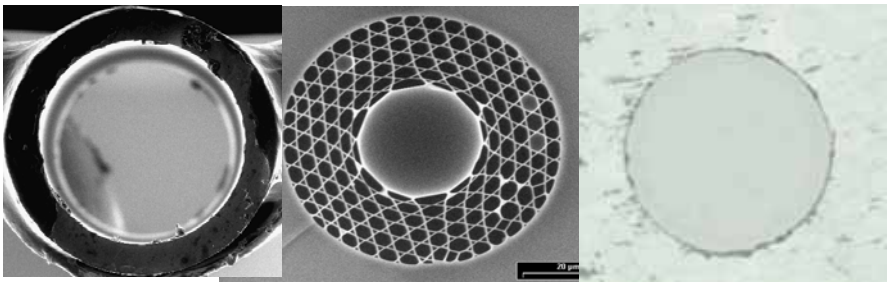

Figure 1. 1: Cross sections of three specialty fibers hollow waveguide, photonic crystal fiber and multimode fiber.

Photonic Crystal Fibers (PCF's) are examples of specialty fibers that attracted much interest in the recent years due to their unusual wave-guiding properties [1]. PCF is formed of periodical pattern of air rods in a dielectric medium. The light is guided or localized in a deformation produced intentionally in the pattern. Quite a few analytical techniques have been published in this field. Figotin et al. [2] used plane wave expansion to study the localization of light in a three dimensional photonic crystal structure when a defect is introduced inside this structure. E Centeno et al. [3] used a full vectorial scattering matrix method to study the localization of light inside a two dimensional photonic crystal. Knight et al. [4] reported the waveguiding properties of the PCF's using

the effective index method. Ferrando et al. [5] presented a full-vectorial analysis of the guided higher-order modes in PCF's.

In comparison to PCF's, multicore fiber (MCF) consists of a few cores placed close to each other to increase the coupling between them. This coupling between the cores modifies the modal property in each core correspondingly. Chang et al. [6] demonstrated a full vectorial modal solution of MCF structures using circular harmonic expansions. Wrage et al. [7] presented numerical and experimental determination of the coupling constant in a MCF when the cores are placed in a ring geometry for mode locked high power fiber laser applications. However, nonlinearity of the cores material restricts the maximum transmitted power.

Hollow waveguides present an attractive alternative to other solid-core infra-red (IR) fibers such as step index fiber and MCF. Key features of hollow guides are: their ability to transmit wavelengths well beyond 20 μm; their inherent advantage of having an air core for high-power laser delivery; and their relatively simple structure and potential low cost [8]. Initially these waveguides were developed for medical and industrial applications involving the delivery of CO_2 laser radiation, but more recently they have been used to transmit incoherent light for broadband spectroscopic and radiometric applications. In general, hollow waveguides enjoy the advantages of high laser power thresholds, low insertion loss, no end reflection, ruggedness, and small beam divergence. Potential disadvantages, however, include an additional loss on bending and a small NA. Nevertheless, they are today one of the best alternatives for both chemical and

temperature sensing as well as for power delivery in IR laser surgery or in industrial laser delivery systems Researchers have done much work in the area of light and mode coupling in these specialty fibers [8].

In 1984 M. Miyagi et al. [9] presented a design of a dielectric coated metallic cylindrical hollow waveguide with the emphasis of low-loss transmission of the HE_{11} mode. Modal structures and transmission properties were clarified for this hollow waveguide by using a normalized surface impedance and admittance. M. Miyagi et al. [10] and S. Abe et al. [11] calculated the bending losses in hollow glass waveguides by relating the power attenuation coefficient to the bending curvature and the normalized impedance of the waveguide.

For the specialty fibers presented above, selective excitation of certain modes with proper optical properties can improve the performance of this system or add an extra functionality to it. This requires designing proper coupling techniques. Kyung Shick et al. [12] presented analytically that the polarization mode coupling between any two linearly polarized (LP) core modes is possible by appropriately adjusting the grating parameters. The grating was created by pressing a two-mode fiber with a groove plate. In this scheme, the mode coupling is achieved by modifying the propagation constant of the light to match that of the desired mode. Derived from this concept, Laurent Vaissie et al [13] presented another selective mode excitation technique through a non-axial evanescent coupling between two highly asymmetric side polished fibers: single mode fiber (SMF) and graded index fiber. Side polishing the fibers allows one to manipulate

the evanescent field near the core of the fiber. Selective excitation of high order azimuthal modes is achieved by appropriately tilting the SMF. Another application of mode excitation in side polished SMF was presented by Russel et al. [14]. The key element in their design is a photoresist grating placed on the surface of a side polished SMF. This grating fiber-coupler was used as a high resolution spectrometer.

These coupling schemes require introducing changes in the existing fiber system such as side polishing and writing gratings in the core or the side of the fiber. Engineering the input light technique, in contrast, can be applied to the existing fiber systems without changing their structure. It only requires adding extra optical components in front of the input facet of the fiber. The purpose of these elements is to alter the phase distribution of the input light at one or more planes along the path of the input light. This phase modulation of the input light manipulates the properties of the field at the input facet of the fiber such as: phase, amplitude and polarization profiles. If one or more of these properties matches that of a certain mode or a set of modes, selective mode excitation is achieved. For this to occur, proper design of the optical components and selection of there locations are required.

Micro elements play a great role in realizing these optical components required to achieve mode selective excitation. For instance, Ghafoori et al. [15] and Fu Yong [16] demonstrated the analysis and fabrication of micro lenses to couple light to single mode fiber. The aim of these micro lenses is to maximize the power coupled to the fundamental mode in a SMF. Conversely, Eric Johnson et al [17] presented a novel diffractive vortex

lens to couple the light to higher order azimuthal modes to avoid the central deformation of the refractive index profile in graded index fibers.

CHAPTER TWO: VISION OF RESEARCH

In the previous chapter we introduced the mode selective excitation by engineering the light at the input of the fiber system. This excitation is achieved through placing proper optical components in the path of the input light. The design of these optical components depends on the structure of the fiber in use as well as the desired mode or set of modes. Choosing this mode or set of modes is a key feature in improving the performance of any optical fiber system, that requires modal analysis and modeling of the light guided in this system. Accordingly, the process of achieving selective mode excitation can be divided into four main parts: modal analysis and modeling of the guided light in these fibers, designing the proper optical components, fabrication of these components, and characterization of their performance in the system.

This work focuses on the selective excitation of certain modes in multimode fiber, few modes fibers, multicore fibers, and hollow cylindrical waveguides for different applications. For example, a multimode fiber, when attached to a single mode fiber, can be utilized as a condensing lens if only radially symmetric modes are excited and the fiber is cut to a proper length. In addition, it can be used as a displacement sensor by measuring the light coupled back to the single mode fiber. This coupling scheme does not require additional optical components. In comparison, coupling the light to a certain higher order linearly polarized mode in few modes fibers requires at least one phase element. Among the first higher order modes, LP_{11} and LP_{21} preserve a minimal intensity

in the central region of the fiber. If selectively excited, these modes can be used to improve the gain properties of the optical fiber amplifiers. Another area of interest where specialty fibers play a great role is light delivery systems. However, these fibers suffer major drawbacks that, in many cases, reduce their performance. The hollow cylindrical waveguide, for instance, suffers of high bending and transmission loss. One way to reduce these losses is to selectively couple the input light to the TE_{01} mode which sustains a TE polarization around the inner wall of the core. This requires a coupling scheme that alters amplitude, phase and polarization due to the degeneracy of the TE_{01} with the TM_{01} mode. Alternatively, multicore fibers suffer of core material nonlinearity that sets a limit on the maximum amount of power being transmitted. This effect can be reduced if the power is spread over a larger area across the fiber. The spreading of the power is made possible by selective coupling to a certain high order mode with field profile which satisfies this power criterion. Finally, integration of micro-optical elements into actual devices presents numerous challenges to the optical engineer. Therefore, prototyping integrated micro-optics is somewhat prohibitive due to cost and complexity. A natural solution to this is the ability to write the optical element into the device without resorting to the prototyping of an optical element followed by an active alignment. One such method of fabrication is through the use of a Focused Ion Beam (FIB).

The main strategy of this research is to first realize the proper modes in each of these fiber systems. The second step is to design optical components that maximize the excitation of these modes. Developing a fabrication procedure for the designed coupling

components comes next. The final phase is to characterize the fabricated components experimentally and confirm the results with numerical simulations.

CHAPTER THREE: MODELING OF SPECIALTY FIBERS

In this chapter we develop several calculation methods with the aim of determining the guided modes in the different fiber systems mentioned in the previous chapters. For the multimode fiber (MMF), one can obtain an analytical modal solution using the linearly polarized modes approximation. On the other hand, multicore fiber and hollow waveguide require a full vectorial solution. In this section we briefly illustrate three different methods to calculate the modal properties of the multimode fiber, multicore fiber and hollow cylindrical waveguide. We will also explain the three dimensional finite difference beam propagation method.

3.1. Multimode Fibers

The multimode fiber is a standard optical fiber structure that supports a large number of modes due to its large core size. Each mode is defined by its propagation constant, β, and field profile. These profiles and propagation constants can be calculated by solving a boundary condition problem at the core cladding interface taking into consideration the continuity of the tangential field components. Applying the separation of variables and solving for linearly polarized modes, the field distribution of the guided modes, $\overline{\psi}_{v,m}(r,\theta,z)$, can be written in terms of the core radius, r_a, and propagation constant, β, as follows [18]

$$\overline{\psi}_{\nu,m}(r,\theta,z)=\begin{cases} A J_m(u_{\nu,m}\dfrac{r}{r_a})\cos(m\theta)e^{-i\beta_{\nu,m}z}\hat{x} & r\le a \\ A\dfrac{J_m(u_{\nu,m})}{K_m(w_{\nu,m})}K_m(w_{\nu,m}\dfrac{r}{r_a})\cos(m\theta)e^{-i\beta_{\nu,m}z}\hat{x} & r>a \end{cases}. \tag{3.1}$$

In equation (3.1), $u_{\nu,m}$ and $w_{\nu,m}$ are the normalized transverse propagation constants inside the core, and in the cladding respectively. They are related to the fiber parameters and the propagation constant, β, through the following relation

$$u_{\nu,m}=r_a\sqrt{k_o{}^2 n_{core}{}^2-\beta_{\nu,m}{}^2}\ \text{and}\ w_{\nu,m}=r_a\sqrt{\beta_{\nu,m}{}^2-k_o{}^2 n_{clad}{}^2}\,, \tag{3.2}$$

where n_{core} and n_{clad} are the core and cladding refractive indexes respectively. In addition, the suffixes ν and m are the indices for the guided radial and azimuthal components respectively. N and $2M+1$ are the total number of radial and azimuthal modes respectively. The values of these normalized transverse propagation constants for each guided mode can be obtained by solving the following characteristic equation [18]

$$\frac{J_m(u)}{uJ_{m-1}(u)}=-\frac{K_m(w)}{wK_{m-1}(w)}. \tag{3.3}$$

3.1.1. Numerical Example: Few Modes Step Index Fiber

In these calculations, we considered a single mode Corning SMF 28 which is a single mode at 1550 nm, and supports four modes at a wavelength of 632.8 nm. Using equations (3.1) and (3.3), the amplitude and phase distributions of the first three higher order linearly polarized modes are depicted in Figure (3.1).

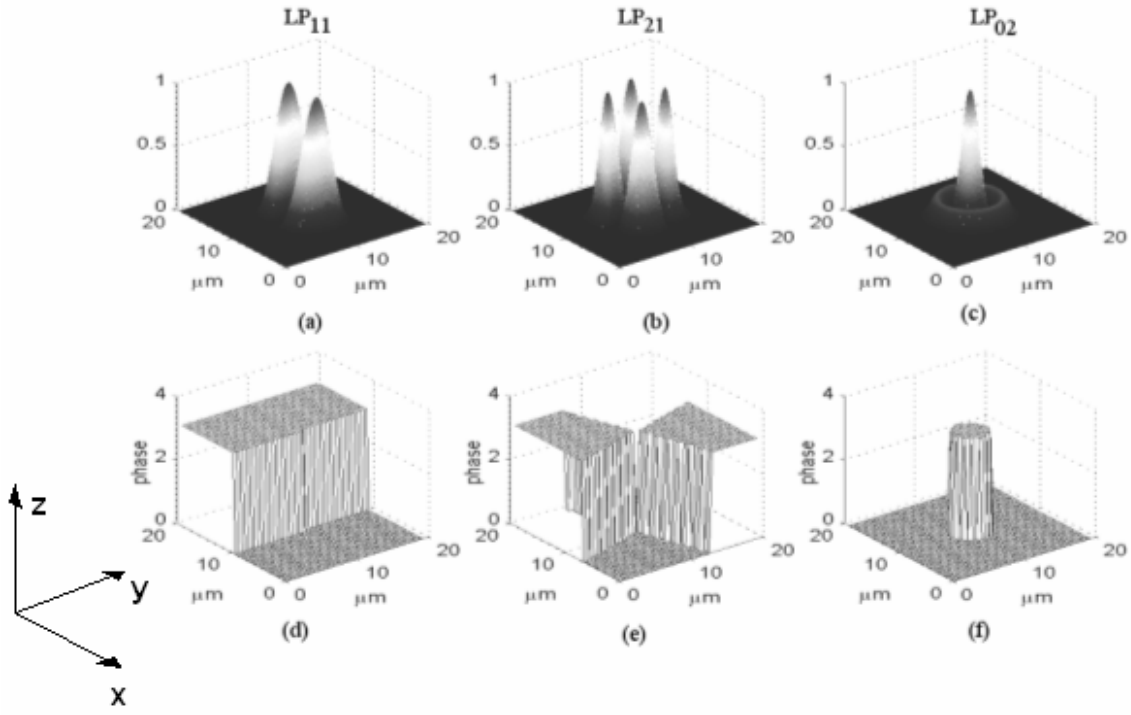

Figure 3. 1: Intensity distributions of the first three higher order modes in few modes fiber at λ=633 nm. (a) LP_{11} (b) LP_{21} (c) LP_{02} and phase distributions of the first three higher order modes (d) LP_{11} (e) LP_{21} and (f) LP_{02}.

For a larger core fiber, the number of guided modes increases. For a standard multimode fiber the number of modes is approximated by $V^2/2$, where V is the, so called, v number of the fiber [18]. Modes are not excited equally. The strength of each mode is strongly dependant on the incident beam profile. This dependence is represented by the coupling efficiency, which is defined as the amount of power coupled to each mode relative to the input one. The square root of this quantity is the field excitation constant. Thus, for a specific input beam profile the field distribution at a specific plane across the fiber is a superposition of the guided modes profiles weighted with the excitation constants taking into consideration the phase gained due to propagation as depicted in Figure (3.2). This superposition is referred to as multimode interference. In Figure (3.2) the Intensity distribution at distance z_1 differs from the one at L although the excitation coefficients of the guided modes do not change while propagating. This difference in the intensity profiles is due to the fact that each mode acquires a different phase while propagating a distance $L-z_1$ as each travels with different propagation constant β as presented in equation (3.1).

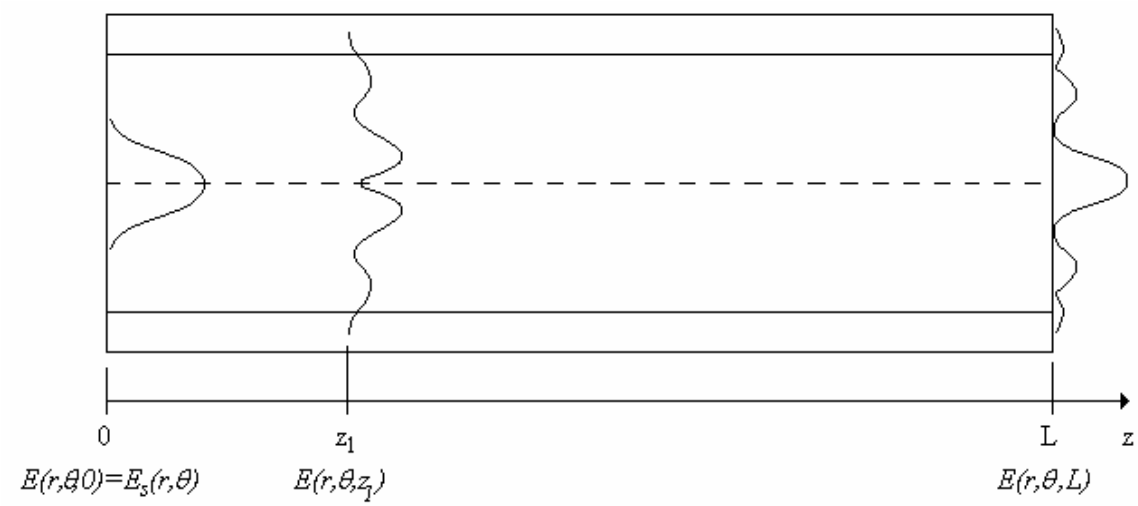

Figure 3. 2: Intensity distribution representation of the light propagating along the MMF due to multimode interference.

3.1.2. Multimode Interference

At any distance, z, along the MMF, the total field distribution is represented as a linear summation of the guided modes in this fashion

$$E(r,\theta,z)=\begin{cases}\sum_{v=1}^{N}\sum_{m=-M}^{M} c_{v,m}\,J_m(u_{v,m}\frac{r}{r_a})\cos(m\theta)\,e^{-i\beta_{v,m}z}\,\hat{x} & r\le a\\ \sum_{v=1}^{N}\sum_{m=-M}^{M} c_{v,m}\,\frac{J_m(u_{v,m})}{K_m(w_{v,m})}K_m(w_{v,m}\frac{r}{r_a})\cos(m\theta)\,e^{-i\beta_{v,m}z}\,\hat{x} & r>a\end{cases}. \quad (3.4)$$

In equation (3.4), $c_{v,m}$ is the field excitation constant. The value of this constant is the

square root of the power coupling coefficient, $\eta_{v,m}$, which is defined as follows

$$\eta_{v,m} = \frac{\left| \int_0^{2\pi} \int_0^{\infty} E_s(r,\theta) \psi_{v,m}(r,\theta) r dr d\theta \right|^2}{\int_0^{2\pi} \int_0^{\infty} |E_s(r,\theta)|^2 r dr d\theta \int_0^{2\pi} \int_0^{\infty} |\psi_{v,m}(r,\theta)|^2 r dr d\theta}. \quad (3.5)$$

In equation (3.5), $E_s(r,\theta)$ is the field distribution at the input facet of the MMF. At the entrance of the MMF, $z=0$, the source field is mapped into the different guided modes, neglecting the cladding modes. Each mode is weighted with the excitation coefficient described above. If E_s is radially symmetric then the value of the overlap integral in (3.5) goes to zero for the modes with a nonzero value of m. This is due to the cosine term in equation (3.4). Omitting these modes, only radial modes will be excited. This is the key feature of utilizing the MMF as a condensing lens as will be described later.

3.2. Scattering Matrix method for modal calculations of Multi-core fiber

Multicore fiber is a collection of step index cores sharing the same cladding region as shown in Figure (3.3). The separation between these cores is very small. Due to the strong coupling between the cores, the individual modes of each fiber split into several sub-modes called supermodes. The number of these super modes depends on the number of cores, symmetry of the structure and the mode order.

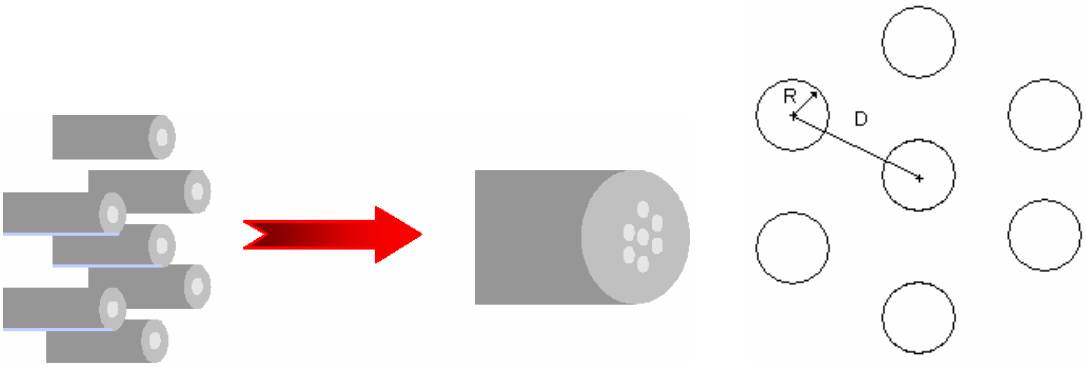

Figure 3. 3: The construction of a standard seven cores multicore fiber.

To utilize this specialty fiber structure a full vectorial wave propagation equation has to be solved in an inhomogeneous medium

$$\nabla \times \nabla \times \mathbf{E}(r,\phi,z) - \omega^2 \mu_o \varepsilon(r,\phi)\mathbf{E}(r,\phi,z) = 0\,. \tag{3.6}$$

The solution of equation (3.6) can be carried by solving two homogeneous wave equations inside and outside the individual cores as follows

$$\begin{aligned} \nabla \times \nabla \times \mathbf{E}(r,\phi,z) - \omega^2 \mu_o \varepsilon_{\mathrm{I}} \mathbf{E}(r,\phi,z) = 0 \\ \nabla \times \nabla \times \mathbf{E}(r,\phi,z) - \omega^2 \mu_o \varepsilon_{\mathrm{II}} \mathbf{E}(r,\phi,z) = 0 \end{aligned}\,. \tag{3.7}$$

In equation (3.7) ε_{I} and $\varepsilon_{\mathrm{II}}$ are the permittivity of the core and cladding regions. These two equations are coupled through the boundary conditions around each core-cladding

interface. One way to solve these equations is to expand the field using a set of orthogonal functions. The selection of these functions depends on the geometry of the structure. Besides, the number of these expansions depends on the required precision. For example, a Fourier expansion represents the field as a sum of plane waves with different direction of propagations and complex amplitudes. Typically, one requires a large number of expansion terms in order to achieve reasonable precision. However, selecting another set of expansion functions might reduce this number dramatically, thus the calculations time and complexity. For instance, the multicore fiber structure can be represented by a set of cylinders placed at certain locations. To accurately calculate the field distribution across this structure using a Fourier expansion, one requires a large number of plane waves. On the other hand, the scattering matrix method (SMM) uses cylindrically symmetric expansion functions. The selection of cylindrically symmetric functions reduces the number of expansions and the computation effort. Moreover, SMM simplifies the effect of the structure geometry to one matrix the so called scattering matrix. Thus, the field at any point of space can be calculated using this matrix. That eliminates sampling and resolution constraints while numerically computing the field distribution across the fiber.

3.2.1. Scattering Matrix Method

Scattering Matrix Method (SMM) is used to solve the set of coupled equations

(3.7) for the guided supermodes [19] to [21]. Using SMM, the structure is represented by cylinders of infinite length. Each cylinder is defined by its center coordinates, radius and refractive index as depicted in Figure (3.4).

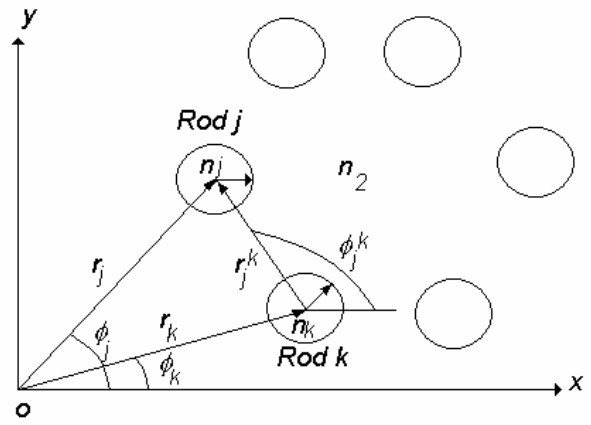

Figure 3. 4: Geometry representation of a general multicore fiber structure.

In this structure each core, of index j, is defined by its location vector $\boldsymbol{r_j}$ measured from a reference point $\boldsymbol{O}$, a refractive index n_j and a radius R_j. Using this representation the total field around each core is the sum of two main components: the local incident field, E^{loc}, and cladding field, E^s. The local incident field is the sum of the evanescent field from the surrounding cores that couples back to that core. The cladding field is the evanescent field due to the guidance inside that core. Figure (3.5) depicts the field representation around two cores.

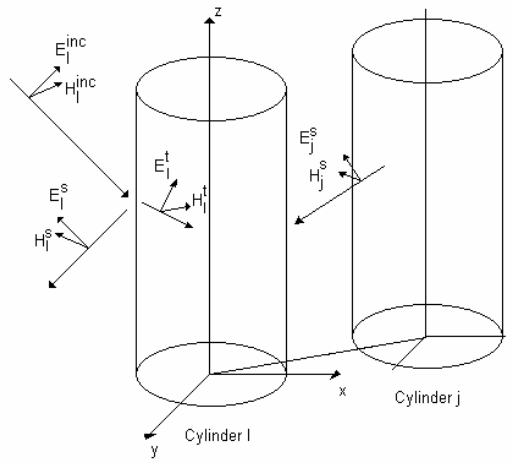

Figure 3. 5: Fields representation around the cores of the multicore fiber.

Due to the geometry of the structure the fields are represented by cylindrical symmetric expansion functions as follows [22]

$$\overline{F}(r,\phi,z) = \overline{F}(r,\phi)e^{i(\varpi t-\beta z)}. \tag{3.8}$$

In equation (3.8), $\overline{F}$ represents the z components of both the Electric and Magnetic Fields

$$\overline{F} = \begin{pmatrix} E_z \\ H_z \end{pmatrix}.$$

The propagation constant, β, corresponds to the z component of the wave vector

according to the coordinates shown in Figure (3.5). The figure shows three field components around rod *j*, the cladding light, the local incident light, and the transmitted , or guided, light. The fields are represented by their respective Fourier-Hankel expansions [22] in equations (3.9) through (3.11)

$$\overline{F}^{s}(r,\phi)=\sum_{j=1}^{N_{rods}}\sum_{m=-N_m}^{N_m}\overline{b}_m H_m^{(2)}(\chi_1\ r_j)\cdot e^{im\phi_j},\qquad \overline{b}_m=\begin{pmatrix}b_m^e\\ b_m^h\end{pmatrix}, \tag{3.9}$$

$$\overline{F}_j^{loc}(r,\phi)=\sum_{m=-N_m}^{N_m}\overline{a}_m J_m(\chi_1\ r_j)\cdot e^{im\phi_j},\qquad \overline{a}_m=\begin{pmatrix}a_m^e\\ a_m^h\end{pmatrix}, \tag{3.10}$$

$$\overline{F}_j^{t}(r,\phi)=\sum_{m=-N_m}^{N_m}\overline{c}_m J_m(\chi_2\ r_j)\cdot e^{im\phi_j},\qquad \overline{c}_m=\begin{pmatrix}c_m^e\\ c_m^h\end{pmatrix}. \tag{3.11}$$

The superscripts ***e*** and ***h*** represent the electric and magnetic fields respectively. The angle ϕ_j is measured from the reference point ***O*** to the center of rod *j*. χ_1 and χ_2 are the tangential components of the wave vector outside and inside the core respectively. They are related to β through the following equation

$$\chi_i=\sqrt{k_o^{\,2}n_i^{\,2}-\beta^2},\quad i=1,2\,. \tag{3.12}$$

However, we must apply the boundary conditions to each core. In order to calculate the

field components in equations (3.9) through (3.11), we need first to apply the boundary conditions at the core-cladding interface at each core, $r=R$, as shown in Figure (3.4). Applying the continuity of the z components of the fields we get the following set of equations

$$\begin{pmatrix} \frac{J_m(\chi_1 R)}{J_m(\chi_2 R)} & 0 \\ 0 & \frac{J_m(\chi_1 R)}{J_m(\chi_2 R)} \end{pmatrix} \cdot \bar{a}_m + \begin{pmatrix} \frac{H_m^{(2)}(\chi_1 R)}{J_m(\chi_2 R)} & 0 \\ 0 & \frac{H_m^{(2)}(\chi_1 R)}{J_m(\chi_2 R)} \end{pmatrix} \cdot \bar{b}_m = \bar{c}_m \quad . \tag{3.12}$$

From the continuity of the ϕ components of the electric and magnetic fields, expressed as a function of the z components of the fields, we get the following equations

$$\begin{pmatrix} \frac{\omega\varepsilon_1}{\chi_1} J_m'(\chi_1 R) & \frac{i\beta m}{R\,\chi_1^2} J_m(\chi_1 R) \\ \frac{i\beta m}{R\,\chi_1^2} J_m(\chi_1 R) & \frac{\omega\mu}{\chi_1} J_m'(\chi_1 R) \end{pmatrix} \cdot \bar{a}_m + \begin{pmatrix} \frac{\omega\varepsilon_1}{\chi_1} H_m^{(2)'}(\chi_1 R) & \frac{i\beta m}{R\,\chi_1^2} H_m^{(2)}(\chi_1 R) \\ \frac{i\beta m}{R\,\chi_1^2} H_m^{(2)}(\chi_1 R) & \frac{\omega\mu}{\chi_1} H_m^{(2)'}(\chi_1 R) \end{pmatrix} \cdot \bar{b}_m = . \begin{pmatrix} \frac{\omega\varepsilon_2}{\chi_2} J_m'(\chi_2 R) & \frac{i\beta m}{R\,\chi_2^2} J_m(\chi_2 R) \\ \frac{i\beta m}{R\,\chi_2^2} J_m(\chi_2 R) & \frac{\omega\mu}{\chi_2} J_m'(\chi_2 R) \end{pmatrix} \cdot \bar{c}_m \tag{3.13}$$

We can combine equations (3.12) and (3.13) in a matrix form taking into account all the expansion coefficients to get the following vector equations

$$\overline{\overline{A}}_1 \cdot \bar{a} + \overline{\overline{B}}_1 \cdot \bar{b} = \bar{c}\,, \tag{3.14}$$

$$\overline{\overline{A}}_2 \cdot \bar{a} + \overline{\overline{B}}_2 \cdot \bar{b} = \overline{\overline{C}}_2 \cdot \bar{c}\,, \tag{3.15}$$

where $\bar{a} = \begin{pmatrix} a_1^e \\ \vdots \\ a_M^e \\ a_1^h \\ \vdots \\ a_M^h \end{pmatrix}$, $\bar{b} = \begin{pmatrix} b_1^e \\ \vdots \\ b_M^e \\ b_1^h \\ \vdots \\ b_M^h \end{pmatrix}$, $\bar{c} = \begin{pmatrix} c_1^e \\ \vdots \\ c_M^e \\ c_1^h \\ \vdots \\ c_M^h \end{pmatrix}$, $\overline{\overline{A}}_1, \overline{\overline{B}}_1, \overline{\overline{A}}_2, \overline{\overline{B}}_2$ and $\overline{\overline{C}}_2$ are square matrixes and M

is the number of expansion coefficients. These matrixes are defined as

$$\overline{\overline{A}}_1 = \begin{pmatrix} \dfrac{\bar{\bar{J}}(\chi_1 R)}{\bar{\bar{J}}(\chi_2 R)} & 0 \\ 0 & \dfrac{\bar{\bar{J}}(\chi_1 R)}{\bar{\bar{J}}(\chi_2 R)} \end{pmatrix}$$

$$\overline{\overline{B}}_1 = \begin{pmatrix} \dfrac{\overline{\overline{H}}^{(2)}(\chi_1 R)}{\bar{\bar{J}}(\chi_2 R)} & 0 \\ 0 & \dfrac{\overline{\overline{H}}^{(2)}(\chi_1 R)}{\bar{\bar{J}}(\chi_2 R)} \end{pmatrix}, \tag{3.16}$$

$$\overline{\overline{A}}_2 = \begin{pmatrix} \frac{\omega\varepsilon_1}{\chi_1}\overline{\overline{J}}'(\chi_1 R) & \frac{i\beta m}{R\,\chi_1^2}\overline{\overline{J}}(\chi_1 R) \\ \frac{i\beta m}{R\,\chi_1^2}\overline{\overline{J}}(\chi_1 R) & \frac{\omega\mu}{\chi_1}\overline{\overline{J}}'(\chi_1 R) \end{pmatrix}$$

$$\overline{\overline{B}}_2 = \begin{pmatrix} \frac{\omega\varepsilon_1}{\chi_1}\overline{\overline{H}}^{(2)'}(\chi_1 R) & \frac{i\beta m}{R\,\chi_1^2}\overline{\overline{H}}^{(2)}(\chi_1 R) \\ \frac{i\beta m}{R\,\chi_1^2}\overline{\overline{H}}^{(2)}(\chi_1 R) & \frac{\omega\mu}{\chi_1}\overline{\overline{H}}^{(2)'}(\chi_1 R) \end{pmatrix}, \qquad (3.17)$$

$$\overline{\overline{C}}_2 = \begin{pmatrix} \frac{\omega\varepsilon_2}{\chi_2}\overline{\overline{J}}'(\chi_2 R) & \frac{i\beta m}{R\,\chi_2^2}\overline{\overline{J}}(\chi_2 R) \\ \frac{i\beta m}{R\,\chi_2^2}\overline{\overline{J}}(\chi_2 R) & \frac{\omega\mu}{\chi_2}J'(\chi_2 R) \end{pmatrix}$$

$$\overline{\overline{J}} = \begin{pmatrix} J_{-\frac{M}{2}} & \dots & 0 \\ \vdots & . & \vdots \\ 0 & \dots & J_{\frac{M}{2}} \end{pmatrix} \quad and \quad \overline{\overline{H}}^{(2)} = \begin{pmatrix} H^{(2)}_{-\frac{M}{2}} & \dots & 0 \\ \vdots & . & \vdots \\ 0 & \dots & H^{(2)}_{\frac{M}{2}} \end{pmatrix}.$$

Solving equations (3.14) and (3.15), a linear relation between the cladding light expansion coefficients vector, *b*, and the local incident one, *a*, can be obtained as follows

$$\overline{b} = \overline{\overline{S}} \cdot \overline{a}\,, \qquad (3.18)$$

where

$$\overline{\overline{S}} = (\overline{\overline{C}}_2^{-1}\overline{\overline{B}}_2 - \overline{\overline{B}}_1)^{-1} \cdot (\overline{\overline{C}}_2^{-1}\overline{\overline{A}}_2 - \overline{\overline{A}}_1)\,. \qquad (3.19)$$

In equations (3.18) and (3.19), $\overline{\overline{S}}$ is a square matrix of dimensions $(2 \cdot N_m + 1) \cdot N_{rods} \times (2 \cdot N_m + 1) \cdot N_{rods}$ which represents the scattering matrix of the multicore fiber. This matrix relates the guided field to the local incident one on each core. The geometry of the structure is implicitly included in the matrix $\overline{\overline{S}}$ as the fields in (3.9) through (3.11) are expanded around the centers of each core. The field inside the cores can be related to the local incident field through the following relation

$$\overline{c} = \overline{\overline{S}}_2 \cdot \overline{a}\,, \tag{3.20}$$

where

$$\overline{\overline{S}}_2 = (\overline{\overline{B}}_2^{-1}\overline{\overline{C}}_2 - \overline{\overline{B}}_1^{-1})^{-1} \cdot (\overline{\overline{B}}_2^{-1}\overline{\overline{A}}_2 - \overline{\overline{B}}_1^{-1}\overline{\overline{A}}_1)\,. \tag{3.21}$$

Although the information regarding the geometry of the structure is hidden in $\overline{\overline{S}}$, we still need to calculate the cross talk between the cores. Recalling that the locally incident field on core *j* is defined as the summation of the cladding light around all the cores except *j* and the incident field, one can the following formula for the local field

$$\begin{aligned} E_j^{loc} &= \sum_{k \neq j} E_k^s \\ \sum_m^M a_m^e J_m(\chi_1 r_j)\, e^{iq\phi_j} &= \sum_{k \neq j} \sum_q^M b_q^e H_q^{(2)}(\chi_1 r_k)\, e^{iq\phi_j} \end{aligned}\,. \tag{3.22}$$

In equation (3.22) the input field is set to zero in order to solve for the allowed propagating modes. Applying the expansion of $H_q^{(2)}(\chi_1 r_k)\, e^{iq\phi_j}$ around r_j, [22]

$$H_q^{(2)}\left(a\left|r-r'\right|\right)e^{im\phi(|r-r'|)} = \sum_m^M J_m(ar)\, e^{im\phi(r)} H_{m-q}^{(2)}\left(ar'\right)e^{i(m-q)\phi(r')} \tag{3.23}$$

to equation (3.22) we get the following relation between the local incident and the cladding field coefficients

$$\bar{a}_m = \sum_{k\neq j}\sum_q^M \bar{b}_m\, T_{m,q,j,k}, \quad T_{m,q,j,k} = e^{i(q-m)\phi_{kl}^{jk}} H_{m-q}^{(2)}(\chi_1 r_k^j)\,. \tag{3.24}$$

This can be written in the following vector form

$$\bar{a} = \overline{\overline{T}} \cdot \bar{b}\,. \tag{3.25}$$

In equation (3.25), $\overline{\overline{T}}$ represents the cross talk between the cores. Recalling the linear relation between $\bar{a}$ and $\bar{b}$ in equation (3.18), we can write equation (3.25) as follows

$$\begin{aligned} &\overline{\overline{M}}_s(\beta).\bar{b} = 0, \\ &\overline{\overline{M}}_s(\beta) = (\bar{\bar{I}} - \overline{\overline{S}} \cdot \overline{\overline{T}}) \end{aligned}, \tag{3.26}$$

where I is the identity matrix. Equation (3.26) represents an Eigen-value problem for which the Eigen-value is zero. Using the linear relation between the local incident field and the guided field in equation (3.20), equation (3.26) can be rewritten in terms of the guided field coefficient as follows

$$\overline{\overline{M}}_{MCF}(\beta).\bar{c} = 0, \tag{3.27}$$

where

$$\overline{\overline{M}}_{MCF} = (\bar{\bar{I}} - \overline{\overline{S}}_2 \cdot \overline{\overline{T}} \cdot \overline{\overline{S}} \cdot \overline{\overline{S}}^{-1}{}_2). \tag{3.28}$$

The solution of the Eigen-value problem in (3.27) can be accomplished by first finding the zeros of the determinant of $\overline{\overline{M}}_{MCF}(\beta)$. This requires applying an iterative technique to search for the complex roots of the determinant. To accelerate the convergence process, we first evaluate the determinant, $\left|\overline{\overline{M}}_{MCF}(\beta)\right|$, over the range

$$\frac{2\pi\sqrt{\varepsilon_{II}}}{\lambda} < \beta < \frac{2\pi\sqrt{\varepsilon_{I}}}{\lambda}. \tag{3.29}$$

For the values of β near the complex zero, the amplitude of the determinant drops dramatically as depicted in Figure (3.6).

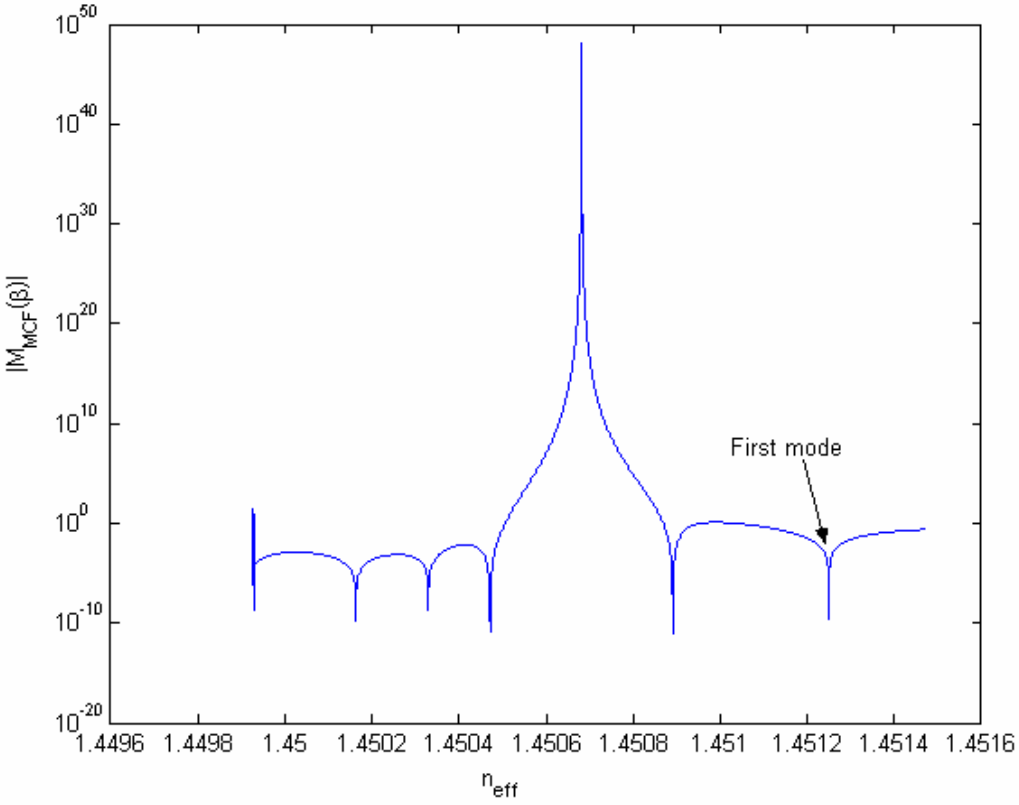

Figure 3. 6: The evaluation of $\left|\overline{\overline{M}}_{MCF}(\beta)\right|$ over the range of the effective refractive indices between $\sqrt{\varepsilon_{II}}$ and $\sqrt{\varepsilon_{I}}$.

The graph in Figure (3.6) is plotted as a function of the effective refractive index defined as $\frac{\beta}{\lambda}$. The figure shows five locations where the amplitude of the determinant drops dramatically. At these locations, the value of β is the closest to the real part of the actual complex root. To find the complex value of the propagation constant, we used the false position method. First, we define two initial points around the real value of β that

minimizes the determinant $\left|\overline{\overline{M}}_{MCF}(\beta)\right|$. Using these values, the complex value of β can be obtained through this recursive formula

$$\beta = \beta_1 - \left|\overline{\overline{M}}_{MCF}(\beta_1)\right| \cdot \left(\frac{\beta - \beta_1}{\left|\overline{\overline{M}}_{MCF}(\beta)\right| - \left|\overline{\overline{M}}_{MCF}(\beta_1)\right|} \right). \tag{3.30}$$

In equation (3.30), the initial value of β and β_1 are complex. The number of these zeros corresponds to the total number of non-degenerate modes.

3.2.2. Numerical Example: Super Modes in Multicore fiber

As a numerical example, we solved equation (3.27) for a seven-core multicore fiber with core to core spacing of 10.5 μm and core radii of 3.5 μm. The core material is considered to be doped fused silica and the cladding is pure fused silica. The operating wavelength is 1.33 μm. This configuration gives a v number of 2.64 for each fiber. Figure (3.7) shows the intensity distributions of the guided supermodes.

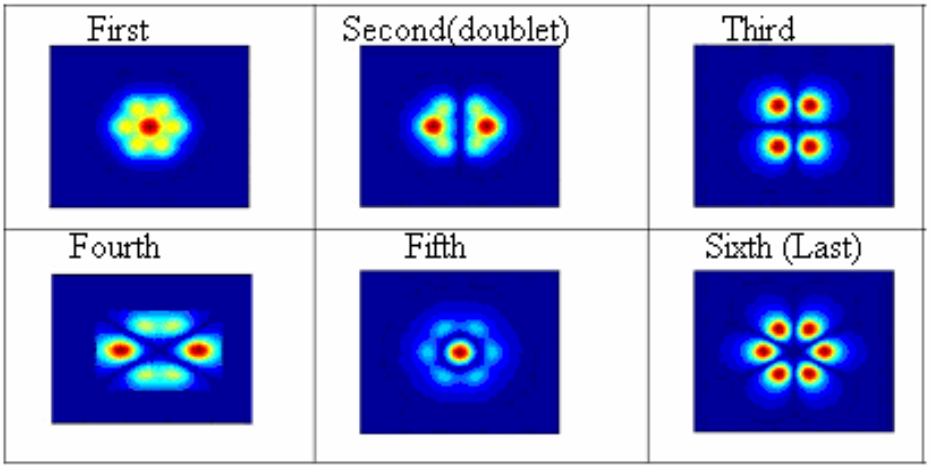

Figure 3. 7: The fundamental supermodes for seven core fiber of fused silica cladding and doped fused silica cores at 1.33 μm operating wavelength. The spacing between the cores is 10.5 μm and core radii of 3.5 μm.

3.3. Hollow waveguide

There are two main structural differences between hollow and solid waveguides. The first is that in hollow waveguides, the solid core is replaced by air or gas. The second is that the cladding of the waveguide is frequently opaque at the operation wavelength. Most of the energy being guided by the hollow waveguide is confined in the core region. The reflectivity of the wall is the most significant parameter determining the performance of a waveguide. A hollow waveguide reflecting wall surface can be dielectric, metal or a more complex dielectric-coated metal structure used to maximize the reflection. The

losses in these structures are due to the less than perfect reflections of the propagating energy at the wall/core interface. Due to the large number of reflections from the wall, any small reflection loss will be greatly amplified [23] and [24].

3.3.1. Modal calculations in cylindrical hollow-glass waveguide (HGW)

Here we are presenting an approximate modal solution of the hollow-glass waveguide structure depicted in Figure (3.8). In this solution we assume that the metallic layer is a perfect conductor and we neglect the thin dielectric layer. Thus the problem is simplified to a metallic cylindrical waveguide as presented in Figure (3.9).

Glass (n_g)	1.4533
Ag (n_{Ag})	11 + i 61.4
AgI (n_{AgI})	2.1
Plastic (n_p)	1.54
AgI Thickness (d_{AgI})	1.25 (μm)
Ag Thickness (d_{Ag})	0.65 (μm)
Glass wall thickness (d_g)	50 (μm)
Plastic coating thinckness (d_p)	165 (μm)

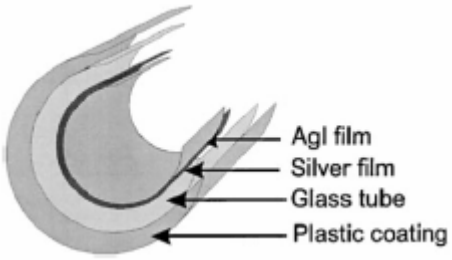

Figure 3. 8: Dielectric coated metallic waveguide structure and materials parameters at 1.55 μm wavelength.

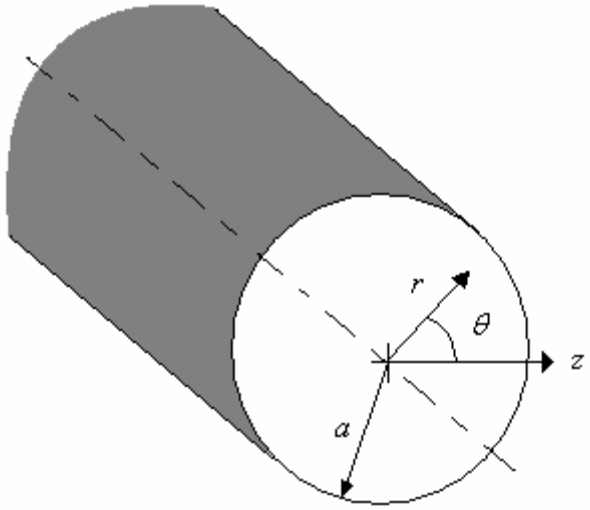

Figure 3. 9: Simplified representation of the HGW by a metallic cylindrical waveguide.

The modes that can be supported in such structure are transverse electric (TE^z) and transverse magnetic (TM^z) modes [25]. The TE^z modes can be derived using the following vector potential representations

$$\begin{aligned} \mathbf{A} &= 0 \\ \mathbf{F} &= \hat{a}_z F_z(r,\theta,z) \end{aligned}. \tag{3.31}$$

However, the vector potential **F** must satisfy the wave propagation equation

$$\frac{\partial^2 F_z}{\partial r^2} + \frac{1}{r}\frac{\partial F_z}{\partial r} + \frac{1}{r^2}\frac{\partial^2 F_z}{\partial \theta^2} + \frac{\partial^2 F_z}{\partial z^2} + \beta^2 F_z = 0\,. \tag{3.32}$$

The solution of equation (3.32) for the geometry in Figure (3.9), using the constraint that the field should be finite everywhere, is demonstrated in this form

$$F_z(r,\theta,z) = A_{mn} J_m(\beta_r r)\left[C_2 \cos(m\theta) + D_2 \sin(m\theta)\right] e^{-i\beta_z z} . \tag{3.33}$$

In equation (3.33), C_2 and D_2 are constants. However, m takes only discrete values under the boundary condition that the fields must repeat every 2π radians in θ as shown below

$$m = 0, 1, 2, ... \tag{3.34}$$

In equation (3.33), β_r and β_z are the transverse and longitudinal propagation constants of the guided mode. They are related through the following equation

$$\beta_z^2 + \beta_r^2 = \beta^2 . \tag{3.35}$$

To obtain values of these propagation constants for the different guided modes, we need to apply the following boundary condition

$$E_\theta(r = a,\theta,z) = 0 . \tag{3.36}$$

In terms of the potential vector F_z, this boundary condition can be written as

$$E_\theta(r=a,\theta,z)=\frac{1}{\varepsilon}\frac{\partial F_z}{\partial r}=\beta_r\frac{A_{mn}}{\varepsilon}J'_m(\beta_r a)[C_2\cos(m\theta)+D_2\sin(m\theta)]e^{-i\beta_z z}=0 \qquad (3.37)$$

which is only satisfied provided that

$$J'_m(\beta_r a)=0\Rightarrow\beta_r=\frac{\chi'_{mn}}{a}, \qquad (3.38)$$

where χ'_{mn} is the nth zero of the derivative of the Bessel function J_m of the first kind of order m. Using equation (3.35), the longitudinal propagation constant β_z is

$$(\beta_z)_{mn}=\sqrt{\beta^2-\left(\frac{\chi'_{mn}}{a}\right)^2}\ . \qquad (3.39)$$

Finally, the electric field components can be written as [25]

$$E_\theta(r,\theta,z)=\frac{1}{\varepsilon}\frac{\partial F_z}{\partial r}=\beta_r\frac{A_{mn}}{\varepsilon}J'_m(\beta_r r)[C_2\cos(m\theta)+D_2\sin(m\theta)]e^{-i\beta_z z}=0\,, \qquad (3.40)$$

$$E_r(r,\theta,z)=\frac{1}{\varepsilon r}\frac{\partial F_z}{\partial\theta}=-A_{mn}\frac{m}{\varepsilon r}J_m(\beta_r r)[-C_2\sin(m\theta)+D_2\cos(m\theta)]e^{-i\beta_z z}=0 \qquad (3.41)$$

$$E_z(r,\theta,z)=0. \qquad (3.42)$$

The TM^z modes can be derived in a similar manner by letting

$$\begin{aligned}\mathbf{A} &= \hat{a}_z A_z(r,\theta,z)\\ \mathbf{F} &= 0\end{aligned}. \tag{3.43}$$

Again, the potential A_z has to satisfy the wave propagation equation. Applying the boundary conditions that the tangential field components have to be zero at $r=a$, the field has to be finite everywhere, and the field has to repeat every 2π radian cahnge of θ, we obtain the following solutions of the propagation constants

$$\begin{aligned}\beta_r &= \frac{\chi_{mn}}{a}\\ (\beta_z)_{mn} &= \sqrt{\beta^2 - \left(\frac{\chi_{mn}}{a}\right)^2},\end{aligned} \tag{3.44}$$

where χ_{mn} is the n^{th} zero of the Bessel function J_m of the first kind of order m. The electric field components can be written as [25]

$$E_r(r,\theta,z) = \frac{-j}{\omega\mu\varepsilon}\frac{\partial^2 A_z}{\partial r\partial z} = -B_{mn}\frac{\beta_r\beta_z}{\omega\mu\varepsilon}J'_m(\beta_r r)\left[C_2\cos(m\theta) + D_2\sin(m\theta)\right]e^{-i\beta_z z} \tag{3.45}$$

$$E_\theta(r,\theta,z) = \frac{-j}{\omega\mu\varepsilon r}\frac{\partial^2 A_z}{\partial\theta\partial z} = -B_{mn}\frac{m\beta_z}{\omega\mu\varepsilon r}J_m(\beta_r r)\left[-C_2\sin(m\theta) + D_2\cos(m\theta)\right]e^{-i\beta_z z} \tag{3.46}$$

$$E_z(r,\theta,z) = \frac{-j}{\omega\mu\varepsilon r}\left(\frac{\partial^2}{\partial z^2} + \beta^2\right)A_z = -jB_{mn}\frac{\beta_r^2}{\omega\mu\varepsilon}J_m(\beta_r r)\left[C_2\cos(m\theta) + D_2\sin(m\theta)\right]e^{-i\beta_z z}.$$

(3.46)

Using the above procedures and for the operating wavelength of 1.55 μm, the transverse field components of the electric field as well as the polarization distributions of the TE_{01} and TE_{02} are depicted in Figure (3.10).

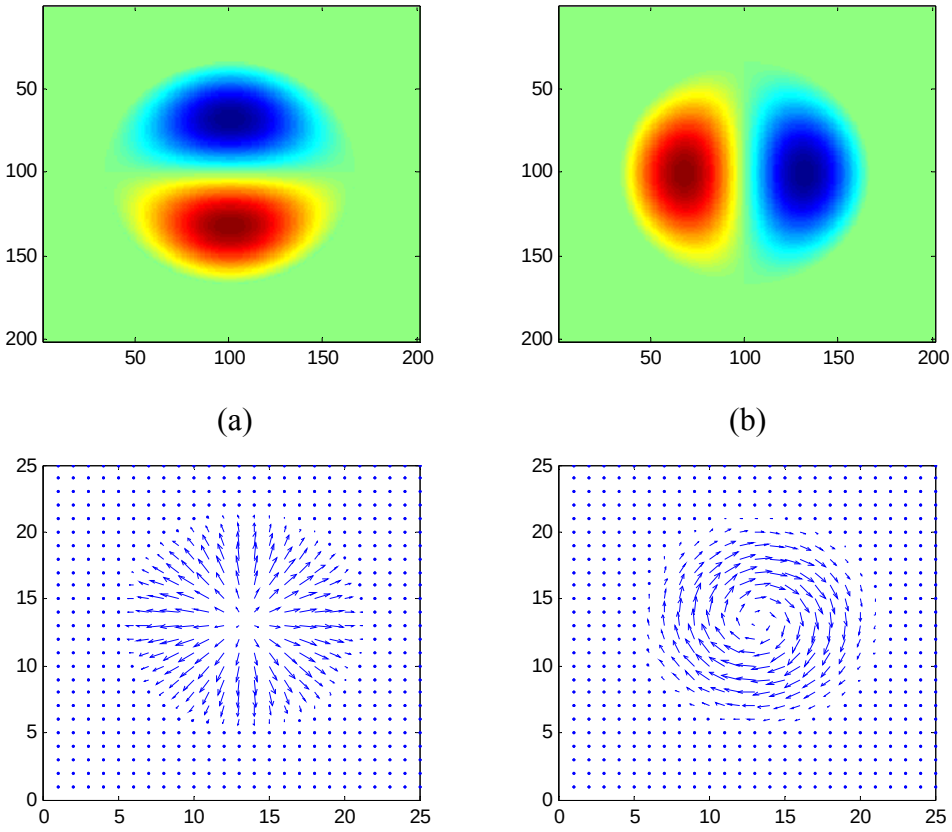

Figure 3. 10: The (a) E_x and (b) E_y field distribution for the TE01 mode. (c) The electric field polarization of TM01 and (d) TE01 respectively.

3.3.2. Loss mechanism in hollow waveguide

This section derives a first order formulation of the hollow waveguide losses through Fresnel refection calculation at the core/wall interface. Figure (3.8) presents the structure and material properties of a dielectric-coated circular hollow waveguide structure. Using the ray optics approach, any guided mode can be represented by an angle, α, and a polarization status. As depicted in Figure (3.11) the angle θ is the complement of α. The reflection loss at core/wall interface can be calculated using Fresnel reflection coefficient for the multi layer structure shown in Figure (3.12).

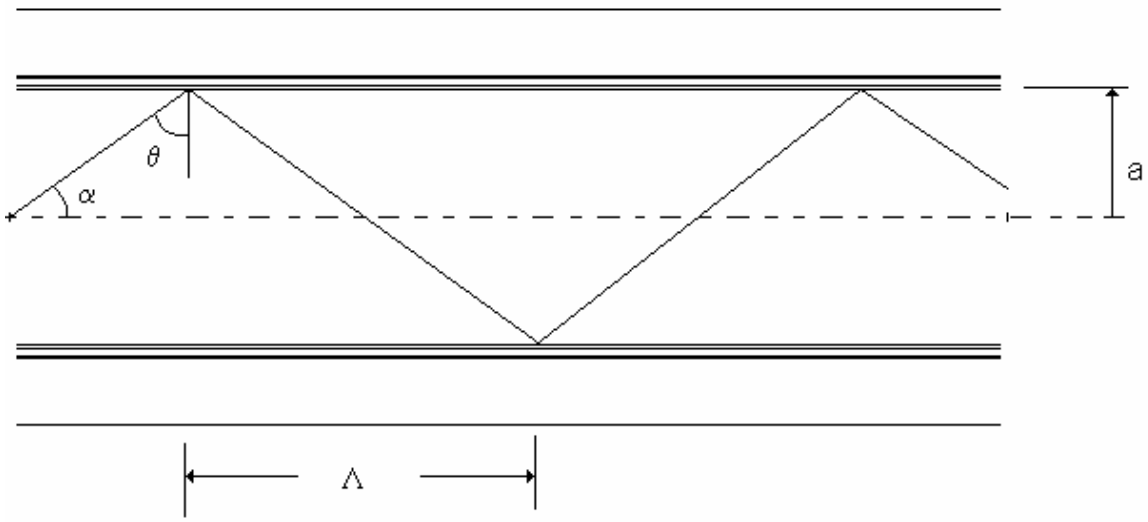

Figure 3. 11: The optical path of a guided mode in the fiber.

For any guided mode the mode angle, α, can be calculated as follows

$$\alpha_{mn} = \tan^{-1}\left(\frac{(\beta_r)_{mn}}{(\beta_z)_{mn}}\right), \tag{3.47}$$

and the incident angle θ_{mn} is

$$\theta_{mn} = \frac{\pi}{2} - \alpha_{mn}. \tag{3.48}$$

The Fresnel reflection of the multilayer structure presented in Figure (3.12) can be calculated as follows

$$\Gamma = \left|\frac{Z(0) - Z_{0,air}}{Z(0) + Z_{0,air}}\right|^2, \tag{3.49}$$

where

$$Z(0) = Z_{o,AgI}\frac{Z(d_{AgI}) - jZ_{o,1}\tan\left(k_o n_{AgI}\cos(\theta_{AgI})d_{AgI}\right)}{Z_{o,AgI} - jZ(z_{AgI})\tan\left(k_o n_{AgI}\cos(\theta_{AgI})d_{AgI}\right)}, \tag{3.50}$$

$$Z(d_{AgI}) = Z_{o,Au}\frac{Z(d_{Au}) - jZ_{o,Au}\tan\left(k_o n_{Au}\cos(\theta_{Au})d_{Au}\right)}{Z_{o,Au} - jZ(z_{Au})\tan\left(k_o n_{Au}\cos(\theta_{Au})d_{Au}\right)}, \tag{3.51}$$

$$Z(d_{Au}) = Z_{o,glass}\frac{Z(d_{glass}) - jZ_{o,1}\tan\left(k_o n_g\cos(\theta_{glass})d_{glass}\right)}{Z_{o,1} - jZ(d_{glass})\tan\left(k_o n_g\cos(\theta_{glass})d_{glass}\right)}, \tag{3.52}$$

$$Z(d_{glass}) = Z_{o,plastic}\frac{Z(d_{plastic}) - jZ_{o,p}\tan\left(k_o n_p\cos(\theta_p)d_{plastic}\right)}{Z_{o,plastic} - jZ(d_{plastic})\tan\left(k_o n_p\cos(\theta_p)d_{plastic}\right)}. \tag{3.53}$$

In equations (3.49) through (3.50)

$$\theta_h = \sin^{-1}\left(\frac{\sin(\theta)}{n_h}\right), \tag{3.54}$$

and for the TE case,

$$Z_{o,h} = \frac{\omega\mu_o}{k_o \cos(\theta_h)}. \tag{3.55}$$

However, for the TM case

$$Z_{o,h} = \frac{k_o \cos(\theta_h)}{\omega\varepsilon_o {n_h}^2}. \tag{3.56}$$

The total transmitted power is approximated by

$$P_{out} = P_{in} * \Gamma^N. \tag{3.57}$$

In equation (3.57), N is the number of reflections of the cladding for the specific mode. The number of reflections is defined as

$$N = 2\frac{L}{\Lambda}, \tag{3.58}$$

where Λ is the spacing between two consecutive reflections as depicted in Figure (3.9). It is defined as

$$\Lambda = \frac{2a\,\beta_z}{\beta_r}. \tag{3.59}$$

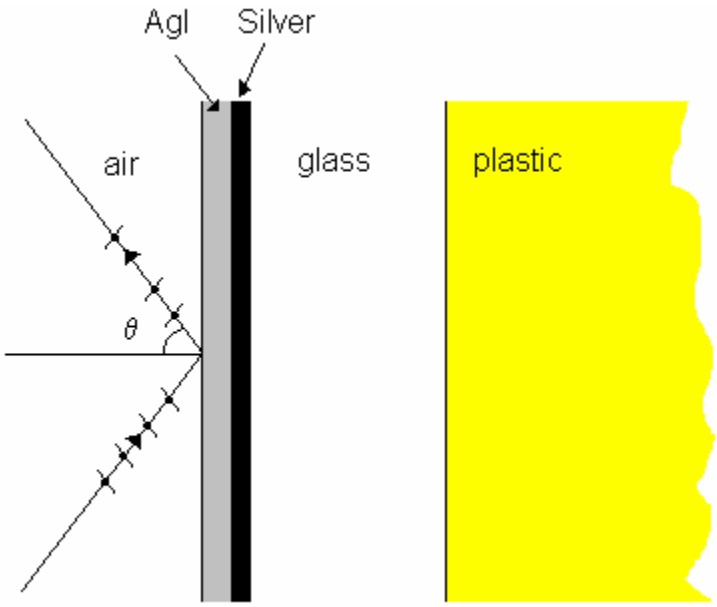

Figure 3. 12: Fresnel reflection from the multilayer fiber cladding

Using equation (3.57), the transmitted power through a 300 μm bore diameter fiber with the parameters mentioned in Figure (3.10) above is depicted in Figure (3.13) as a function

of the mode angle for both TE and TM polarizations. The figure shows that TE polarization suffers from less power loss than the TM case. Though, the difference in transmittance is very small, around 0.2 dB. Thus, a mode of electric field that keeps a TE polarization around the boundary will suffer the least amount of power loss.

In the previous analysis, we considered the transmission losses as for the TE and TM modes. However, when guiding the light inside the fiber, HE_{11} is the most dominant mode and hence the transmission loss is mainly related to this mode. The attenuation coefficient of the power, 2α, for this mode can be expressed as [27]

$$2\alpha = k_o \frac{8U_o^{\,2}}{(k_o a)^3} \mathrm{Re}\{z_{TE} + y_{TM}\}. \tag{3.60}$$

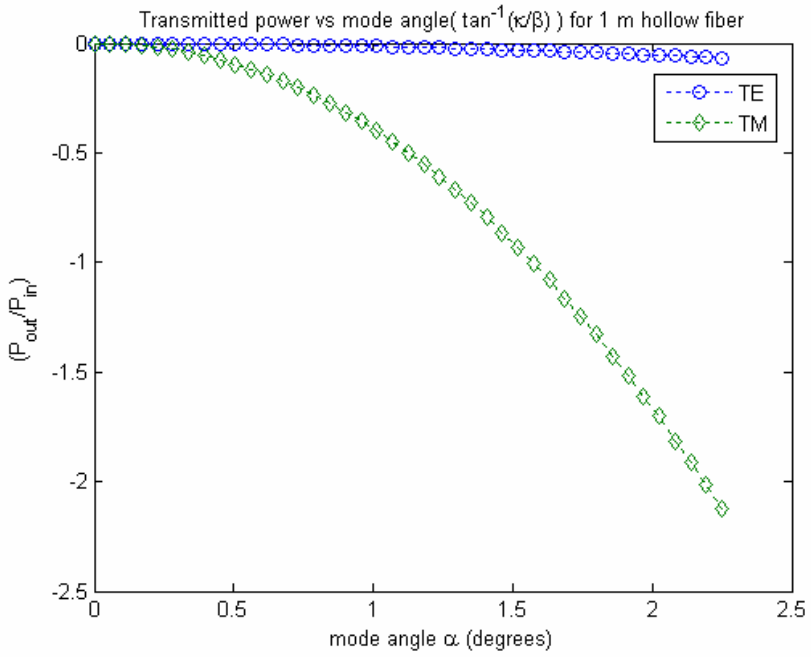

Figure 3. 13: Transmission of a 300 μm bore diameter hollow waveguide.

In equation (3.60), U_o is the first zero point (2.4024) of the Bessel function $J_o(U_o)$. The normalized TE impedance and TM admittance are defined as [28]

$$z_{TE} = z_l \frac{z_c + i \cdot z_l \cdot \tan(x)}{z_l + i \cdot z_c \cdot \tan(x)}, \tag{3.61}$$

and

$$y_{TE} = y_l \frac{y_c + i \cdot y_l \cdot \tan(x)}{y_l + i \cdot y_c \cdot \tan(x)}, \tag{3.62}$$

where, the normalized impedance and admittance of the dielectric layer (z_l and y_l) and metal are defined as

$$z_l = \left(n_{Ag}{}^2 - 1\right)^{-1/2} \quad \textbf{and} \quad y_l = n_{Ag}{}^2 \cdot \left(n_{Ag}{}^2 - 1\right)^{-1/2} \tag{3.63}$$

$$z_c = \left(n_{AgI}{}^2 - 1\right)^{-1/2} \quad \textbf{and} \quad y_c = n_{AgI}{}^2 \cdot \left(n_{AgI}{}^2 - 1\right)^{-1/2} \quad , \tag{3.64}$$

and

$$x = \left(n_{AgI}{}^2 - 1\right) k_o \cdot d_{AgI} \, . \tag{3.65}$$

Another loss mechanism in the hollow waveguide is the bending loss. Bending the fiber causes the excitation of higher-order modes with larger angles. Thus, the losses increase as depicted in Figure (3.13). In addition, bending the fiber causes coupling to TM modes

which suffer of high attenuation. While bent, the laser beam can travel in the fiber in two possible modes as depicted in figures (3.14,a and b). In the first one, the light reflects from both sides, while for the second case the light collides with one side only. The second case is referred to as whispering gallery mode [28]. Figure (3.14,c) shows the geometry of the bent fiber and the ray paths for both modes of propagation. Using this geometry, the complement mode angles, θ_1 and θ_2 can be calculated as follows [20]

$$\theta_{1,2} = \sin^{-1}\left(\frac{R}{R \pm a}\cos\alpha\right) \tag{3.66}$$

where R is the radius of curvature and *a* is the bore radius as can be seen in Figure (3.14,c).

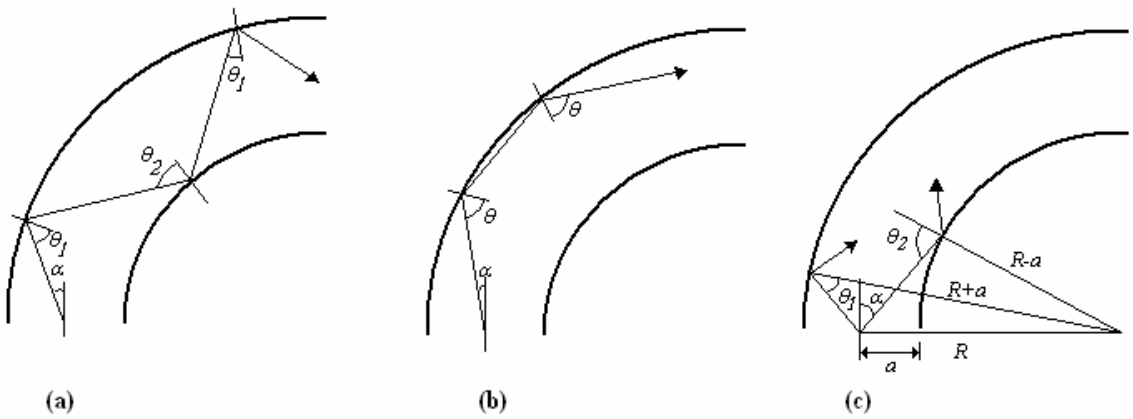

Figure 3. 14: The two modes of ray and angles corresponding to: (a) reflection from both walls of the fiber and (b) colliding with one side only. (c) The geometry used to calculate the angles for both modes.

The two modes of propagation are separated when θ_2=90^o. Thus, the first mode of propagation exists when

$$\alpha < \frac{R-a}{R}. \tag{3.67}$$

As can be seen in equation (3.67), the type of propagation depends on the mode angle and the radius of curvature. This is an important factor to be taken into consideration while calculating the bending loss for a particular mode in addition to the state of polarization of that mode. In this section, we will compare the bending loss calculations for the TE_{01} and TM_{01} modes respectively. The polarization distributions of these two modes are shown in Figure (3.10). Considering a plane of symmetry along this fiber, the electric field of the TE_{01} is normal to this plane. However, for the TM_{01} mode the electric field lies in the plane of symmetry. In other words, the TE_{01} mode maintains a TE polarization around the inner wall of the fiber. Conversely, the TM_{01} can be considered to maintain a TM state of polarization around the walls of the fiber. Using these considerations, the bending losses of both modes can be calculated by calculating the Fresnel reflections from the inner wall for the TE and TM cases. The angles of incident are calculated from the mode angle α and the radius of curvature as represented in equation (3.67).

3.3.3. Numerical Example: calculations of the bending loss for the TE_{01} and TM_{01} modes in a 300 μm core HGW at 980 nm

To determine the mode angle for each mode, we first need to compute the transverse and longitudinal propagation constants, β_r and β_z, through equation (3.39), (3.40) and (3.43). For the TE_{01} mode

$$\begin{aligned} \beta_r &= \frac{3.3838}{300\times10^{-6}} = 1.1298\times10^{4}\, m^{-1} \\ \beta_r &= \sqrt{\left(\frac{2\pi}{980\times10^{-9}}\right)^2 - \left(\frac{3.3838}{300\times10^{-6}}\right)^2} = 6.4114\times10^{6}\, m^{-1} \end{aligned} . \tag{3.68}$$

Thus, the mode angle is

$$\alpha_{TE} = \tan^{-1}\left(\frac{1.1298\times10^{4}}{6.4114\times10^{6}}\right) = 0.002 \text{ rad.} \tag{3.69}$$

Similarly, for the TM_{01} mode

$$\begin{aligned} \beta_r &= \frac{2.2405}{300\times10^{-6}} = 7.468\times10^{3}\, m^{-1} \\ \beta_r &= \sqrt{\left(\frac{2\pi}{980\times10^{-9}}\right)^2 - \left(\frac{2.2405}{300\times10^{-6}}\right)^2} = 6.4114\times10^{6}\, m^{-1} \end{aligned} . \tag{3.70}$$

Thus, the mode angle is

$$\alpha_{TM} = \tan^{-1}\left(\frac{7.468\times10^{3}}{6.4114\times10^{6}}\right) = 0.0012 \text{ rad.} \tag{3.71}$$

In a bent fiber, light can propagate in two different modes as can be seen in figures (3.14, a and b). Equation (3.67) presents a condition over the mode angle for the first mode of propagation to exist. This equation can be rewritten in the following form

$$R > \frac{a}{1-\alpha}. \tag{3.72}$$

As can be seen by equations (3.70) and (3.72), the mode angles are very small compared to unity. Thus, for the whispering gallery mode to exist the radius of curvature has to be as small as the bore radius of the fiber, which is an extreme case. So, the light propagates in the first mode as depicted in Figure (14.a). As both mode angles, α_{TE} and α_{TM}, are very small, the cosine of these angles can be set to unity. Therefore, equation (3.66) can be simplified to

$$\theta_{1,2} = \sin^{-1}\left(\frac{R}{R\pm a}\right). \tag{3.73}$$

Using equation (3.73) and equations (3.49) through (3.59), the normalized transmitted power versus the bending curvature is depicted in Figure (3.15) for both the TE_{01} and TM_{01} modes. As predicted, the TM_{01} suffers of a very high bending loss compared to the TE_{01} mode.

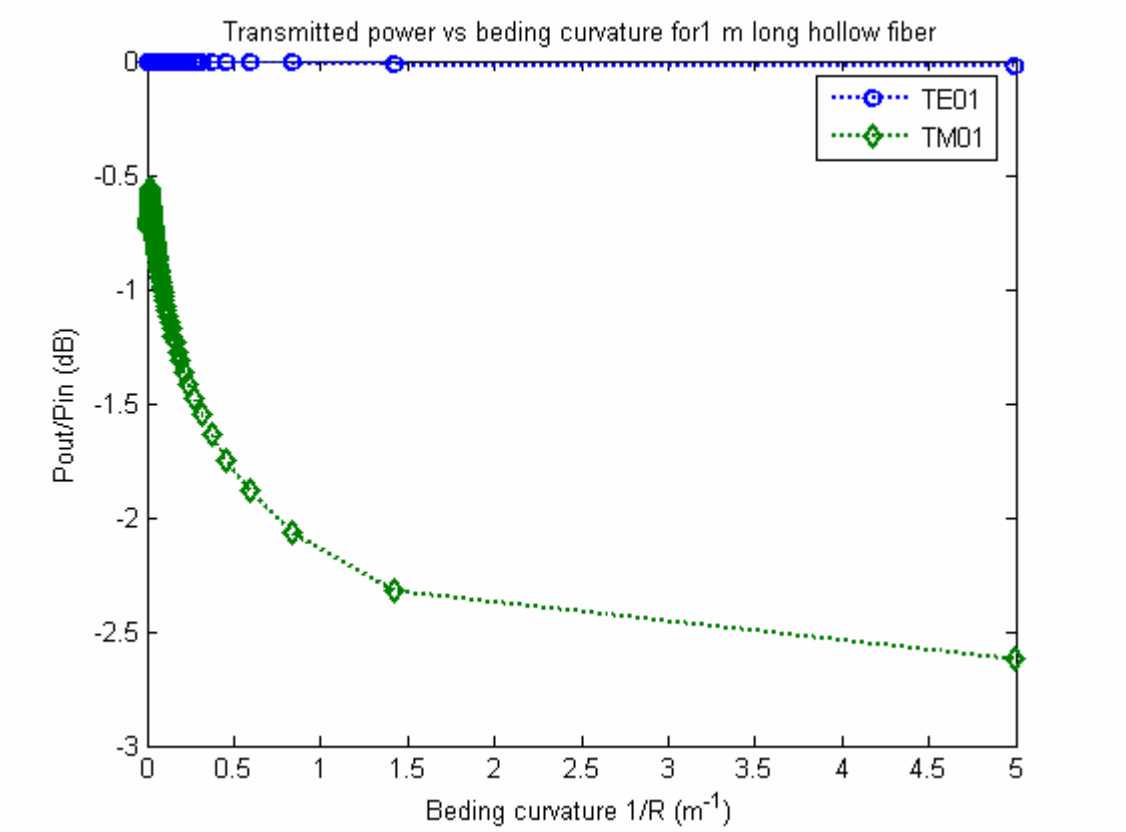

Figure 3. 15: Transmittance of the TE_{01} and TM_{01} modes versus the curvature of the fiber (1/R) for a bore

CHAPTER FOUR: DESIGN OF OPTICAL COUPLING METHODS

The previous section demonstrated different modeling techniques for multimode fiber, multicore fiber and hollow cylindrical waveguide. Using these techniques, we investigated the properties of the guided modes in these specialty fibers. Among those modes, certain higher order modes exhibit interesting complex field distributions which can be used to overcome the limitations of these light delivery systems as explained in chapters one and three. In order to benefit from such field properties we need to selectively couple to those modes. This section deals with the design of novel coupling schemes that maximize the power coupled to a certain mode or set of modes in these fibers for different applications.

4.1. Single mode fiber to multimode fiber direct coupling

Multimode interference and re-imaging conditions [29] provide the basis for the operation of the wavelength tunable lens. In the past, multimode interference theory has been utilized in the design and fabrication of devices such as modulators [30] and Mach-Zender switches [31]. For an input field centered symmetrically on the optical axis of a multimode fiber, multimode interference results in periodic longitudinal locations within the fiber where the source field is duplicated. Characterizing the re-imaging effect in a multimode fiber, it is possible to design and fabricate a device that provides a mechanism

to overcome the natural tendency for the light to diverge when exiting the fiber.

Traditionally, when fiber based devices are designed and fabricated, it is assumed that collimating optics have been incorporated to combat the natural divergence of the exiting beam [32]. In fact, some approaches actually involve fabricating lenses on the ends of the fiber [33]. The device we present essentially performs a lensing operation on the input field incident to the multimode fiber, condensing the light to wavelength dependent longitudinal locations outside the fiber. By analogy to the traditional lens, we will call these locations outside the multimode fiber (MMF) where the field condenses focal planes using our virtual lens model. These locations and associated spot sizes are a function of the core diameter of the multimode fiber, the material properties of the fiber, and the wavelength of the source. We present a method to theoretically predict the shift of the focal plane as a function of wavelength in comparison to experimentally observed behavior and results obtained through FD-BPM simulations. These FD-BPM simulations are also used to verify the validity of the model we present for the determination of the beam spot size observed at the wavelength dependent locations where the output beam is condensed.

4.1.1. Multi mode interference

The basis for this work lies in the concept of re-imaging based on the multimode interference effect associated with multimode waveguides as was done for the case of a

planar waveguide [29]. The re-imaging distance is where the input source is replicated in both amplitude and phase. In contrast to the planar waveguide approach, a re-imaging condition is established for a circular multimode waveguide. Moreover, fractional planes are defined where light appears to be concentrated (see Figures (4.1,a), (4.1,b)). The specific planes where field concentration and re-imaging occur are determined through use of analytical approximations that are derived on the premise that the input light source is provided by a single mode fiber fusion spliced to a section of MMF.

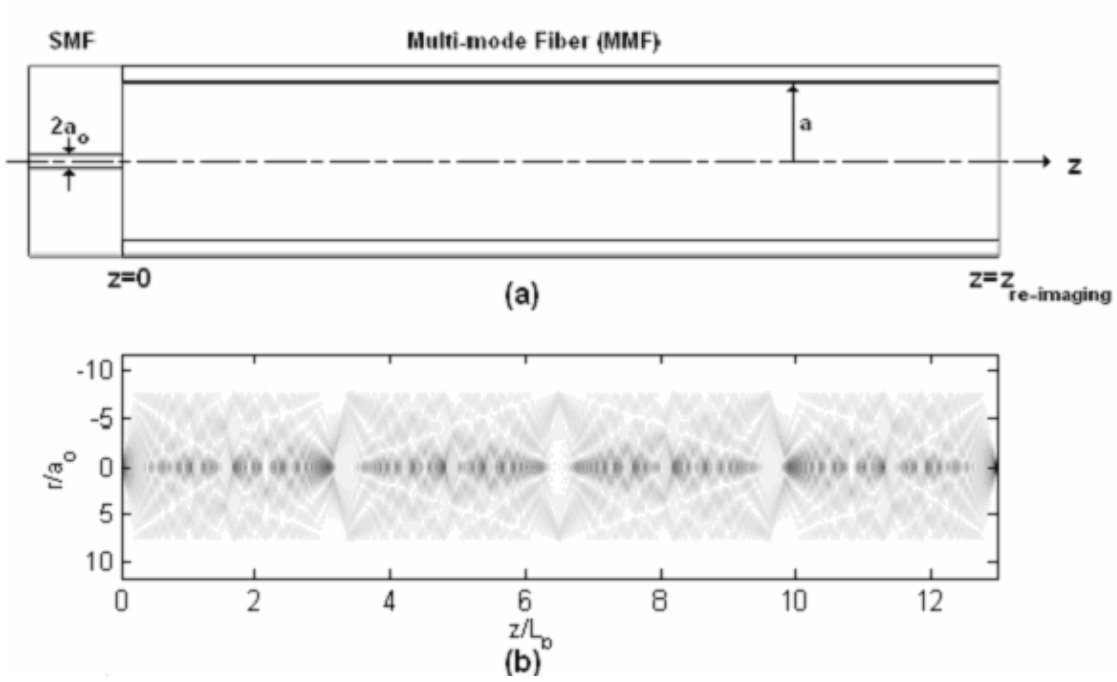

Figure 4. 1: Geometry of the device, SMF fusion spliced to a MMF. (b) Amplitude distribution of the light inside the MMF for the fibers parameters mentioned in table (1).

4.1.2. SMF to MMF Coupling

In order to determine the longitudinal re-imaging locations inside a MMF, with an input field provided from a single mode fiber (SMF) fusion spliced directly to the MMF, it is necessary to first determine which modes are excited in the MMF based on the SMF source. This may be derived by the coupling efficiency associated with the propagating modes within the MMF. Using the linearly polarized mode approximation, the input field provided from the SMF, $\overline{E}_s(r)$ can be approximated by a Gaussian beam as follows

$$\overline{E}_s(r) = e^{-(r/w_g)^2} e^{-i\beta_o z}\hat{x}, \tag{4.1}$$

where β_o is the longitudinal propagation constant for the SMF guided mode, LP_{01}. The half width half max (HWHM) spot size, w_g, of the Gaussian beam can be determined empirically [36], based on the radius of the SMF, a, and the V-number, $V = \left(2\pi a/\lambda\right)\sqrt{n_{core}^2 - n_{clad}^2}$, where n_{core} and n_{clad} are the core and cladding refractive indices respectively, as

$$w_g = \frac{a}{\sqrt{\ln 2}}\left(0.65 + 1.619V^{-1.5} + 2.879V^{-6}\right). \tag{4.2}$$

This input field excites a specific number of guided modes inside the MMF. These

modes, together with the radiating modes, form an orthogonal set [39]. Neglecting the radiating modes effect, the field distribution at any location across the MMF can be written as a series expansion of the guided modes as depicted in equation (4.3)

$$\overline{E}(r,\theta,z) = \sum_{m=-M}^{M} \sum_{v=1}^{N} c_{v,m} \overline{\psi}_{v,m}(r,\theta,z). \tag{4.3}$$

In equation (4.3) the suffixes v and m are the indices for the guided radial and azimuthal components respectively. N and $2M+1$ are the total number of radial and azimuthal guided modes respectively. The vector $\overline{\psi}_{v,m}(r,\theta,z)$ represents the complex field amplitude of the guided mode. Applying the separation of variables and solving Maxwell equations inside the MMF for linearly polarized modes, $\overline{\psi}_{v,m}(r,\theta,z)$ can be written as follows [35]

$$\overline{\psi}_{v,m}(r,\theta,z) = \begin{cases} c_{v,m} J_m(u_{v,m} \dfrac{r}{a}) \cos(m\theta) e^{-i\beta_{v,m} z} \hat{x} & r \le a \\ d_{v,m} K_m(w_{v,m} \dfrac{r}{a}) \cos(m\theta) e^{-i\beta_{v,m} z} \hat{x} & r > a \end{cases}, \tag{4.4}$$

where $u_{v,m}$, and $w_{v,m}$ are the normalized transverse propagation constant inside the core, and in the cladding respectively. The symbol $\beta_{v,m}$ corresponds to the longitudinal propagation constant for this mode and a is the radius of the MMF. The symbols J_m and

K_m are the m[th] order Bessel and modified Bessel functions respectively. The normalized transverse wave number, u_v and w_v, are defined as

$$u_{v,m} = a\sqrt{k_o{}^2 n_{core}{}^2 - \beta_{v,m}{}^2} \; and \; w_{v,m} = a\sqrt{\beta_{v,m}{}^2 - k_o{}^2 n_{clad}{}^2}\,, \tag{4.5}$$

where, n_{core} and n_{clad} are the core and cladding refractive indices respectively, and k_o is the wave number in free space, $\frac{2\pi}{\lambda}$. The coefficients $c_{v,m}$ and $d_{v,m}$ are constants. A direct relation is obtained between these constants by applying the continuity of the tangential field components at the core cladding interface as follows

$$d_{v,m} = \frac{J_m(u_{v,m})}{K_m(w_{v,m})} c_{v,m}\,. \tag{4.6}$$

Thus equation (4.4) can be incorporated into equation (4.3) to represent the radial and azimuthal modes within the MMF. At z = 0, the left hand side of equation (4.3) should equal the input field, $E_s(r)$, as shown in the geometry of Figure (4.1,a). In other words, at this position, the input field is projected onto an orthogonal set of the transverse field components of the guided and leaky modes inside the MMF with different weights. These weights are referred to as the mode excitation coefficients of these modes. Here, we will neglect the influence of the leaky modes inside the MMF, and hence in equation (4.4) the constant $c_{v,m}$ is the field excitation coefficient of the $LP_{v,m}$ mode. Since of the input field

defined by equation (4.1) does not contain any azimuthal components, the field distribution inside the MMF should be radially symmetric. Thus, the excitation coefficient vanishes for values of m greater than 0. This constraint simplifies the representation for the field within the MMF into a sum of radial modes as follows

$$\overline{E}_s(r,0) = \begin{cases} \sum_{v=1}^{N} c_{v,0} J_0(u_{v,0}\frac{r}{a})\hat{x} & r \le a \\ \sum_{v=1}^{N} d_{v,0} K_0(w_{v,0}\frac{r}{a})\hat{x} & r > a \end{cases}. \tag{4.7}$$

For simplicity we will omit the suffix for the azimuthal modes and write the excitation coefficients, the normalized traverse propagation constant and the longitudinal propagation constant as c_v, d_v, u_v, and β_v respectively. To calculate the field excitation coefficients, we will use the power coupling coefficient, η_v. The power coupling coefficient determines the amount of the input power that couples to each specific mode in the MMF. In terms of an overlap integral in cylindrical coordinates η_v can be determined using the following equation

$$\eta_v = \frac{\left|\int_0^{\infty} E_s(r)\psi_v(r)rdr\right|^2}{\int_0^{\infty}|E_s(r)|^2 rdr \int_0^{\infty}|\psi_v(r)|^2 rdr}. \tag{4.8}$$

\The function $\psi_\nu(r)$ represents the field distribution of the ν^{th} guided radial mode. Using the fact that the input field is much smaller than the actual core diameter of the MMF itself, we can neglect the extension of the mode field in the cladding region in the numerator of equation (4.6). Using this assumption, the field excitation coefficient, c_ν, can be related to the power coupling efficiency, η_ν, through $c_\nu = \sqrt{\eta_\nu}$ since the integration in the numerator in equation (4.8) is the cross correlation between the input and the core fields. In this case the overlap integral can be written as

$$\eta_v = \frac{\left| \int_0^\infty \exp\left[-\left(\frac{r^2}{w_g{}^2} \right) \right] J_0\left(\frac{u_v r}{a} \right) r dr d\theta \right|^2}{\int_0^\infty \exp\left[-\left(\frac{2r^2}{w_g{}^2} \right) \right] r dr \left[\int_0^a J_0\left(u_\nu \frac{r}{a} \right)^2 r dr + \left(\frac{J_0(u_v)}{K_0(w_v)} \right)^2 \int_a^\infty K_0\left(w_\nu \frac{r}{a} \right)^2 r dr \right]}. \quad (4.9)$$

Using Hankel Transform properties, an analytical solution can be deduced as a function of the guided modes and the terms dependant on the physical parameters of the fibers used

$$\eta_v = \frac{2\left(\frac{w_g}{a} \right)^2 \exp\left[-\left(\frac{w_g{}^2}{a} \right)\left(\frac{u_v{}^2}{2} \right) \right]}{J_0^2(u_v) + J_1^2(u_v) + \left(\frac{J_0(u_v)}{K_0(w_v)} \right)^2 \left(K_1^2(w_v) - K_0^2(w_v) \right)}. \quad (4.10)$$

From the asymptotic formulation for the roots of the 0^{th} order Bessel function [39], the normalized transverse wave numbers can be written as

$$u_v = (2v - \tfrac{1}{2})\frac{\pi}{2} \quad , \tag{4.11}$$

$$w_v = \sqrt{V^2 - \left((2v - \tfrac{1}{2})\frac{\pi}{2}\right)^2} \, , \tag{4.12}$$

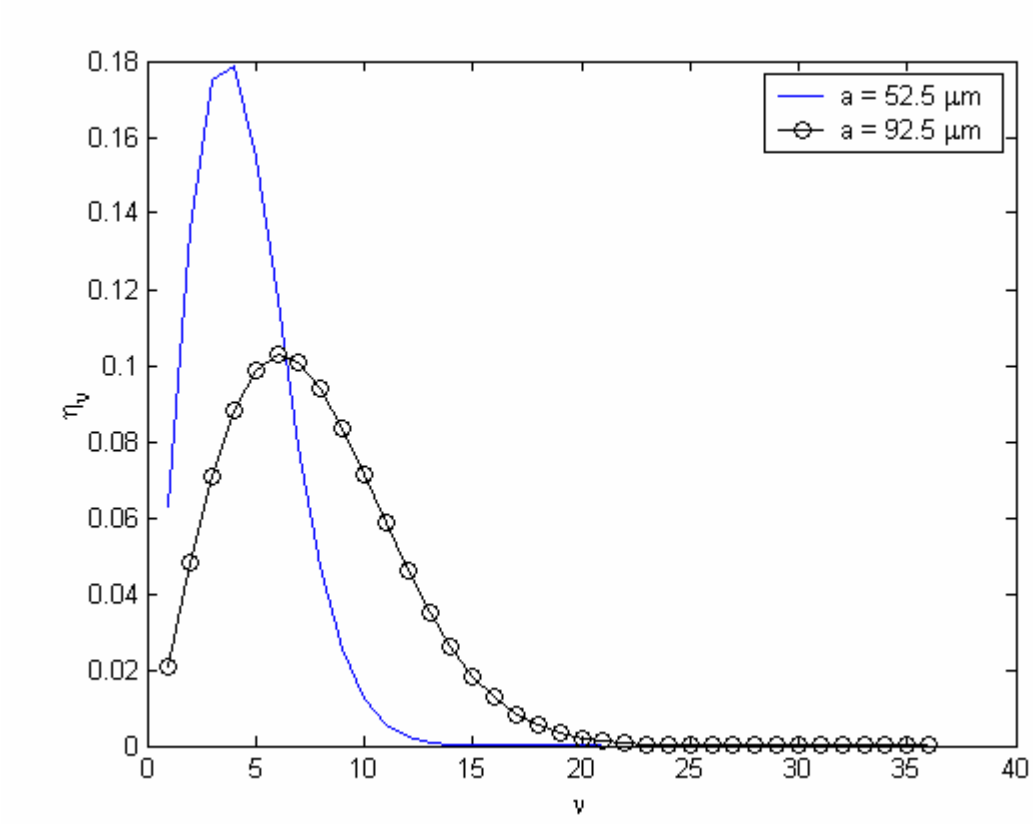

Figure 4. 2: Coupling efficiency as function of mode number for MMF core radii of

52.5μm and 92.5μm respectively

In equation (4.12), V is the V number of the multimode fiber. Thus, equation (4.8) can be modified into the following form

$$\eta_v = \frac{2\left(\frac{\omega}{a}\right)^2 \exp\left[-\frac{1}{2}\left(\frac{\omega^2}{a}\right)\left((2v-\frac{1}{2})\frac{\pi}{2}\right)^2\right]}{J_0^2\left((2v-\frac{1}{2})\frac{\pi}{2}\right)+J_1^2\left((2v-\frac{1}{2})\frac{\pi}{2}\right)+\left(\frac{K_1^2(\sqrt{V^2-\left((2v-\frac{1}{2})\frac{\pi}{2}\right)^2})}{K_0^2(\sqrt{V^2-\left((2v-\frac{1}{2})\frac{\pi}{2}\right)^2})}-1\right)J_0^2\left((2v-\frac{1}{2})\frac{\pi}{2}\right)}. \quad (4.13)$$

Using the equation above, the power coupling coefficient is calculated for all the allowed radial modes inside two MMF have the same material properties as in table (4.1) but two different radii: 52.5 μm and 92.5 μm as depicted in Figure (4.2). The most pronounced feature in the graph is the presence of a peak coupling efficiency associated with a specific mode number. This feature is the key for predicting the re-imaging and the fractional planes where light is concentrated as will be presented in the next section.

Table 3. 1

Optical Fiber Characteristics

FIBER TYPE	CORE RADIUS	CLADDING RADIUS	CORE REF. INDEX
SMF-28	4.5μm	62.5μm	1.4505
Step Index MMF	52.5μm	62.5μm	1.479

4.1.3. Re-imaging Conditions

In this section we present an analytical formulation of the location of the re-imaging and the fractional planes where light is concentrated using the fact that the power coupling efficiency is maximum for a specific mode number. In order to determine which radial guided mode has the highest coupling efficiency associated with it, it is necessary to look at the derivative of the coupling coefficient with respect to the mode number. Using the formulation for the coupling efficiency depicted in equation (4.13), the mode number associated with peak coupling efficiency is determined by taking the derivative with respect to the mode number and equating it to zero as follow

$$\frac{\partial \eta_v}{\partial v} = 0 \quad . \tag{4.14}$$

We introduce a parameter D_ν defined as

$$D_v = J_0^2\left((2v-\tfrac{1}{2})\frac{\pi}{2}\right)+J_1^2\left((2v-\tfrac{1}{2})\frac{\pi}{2}\right)+\left(\frac{K_1^2(\sqrt{V^2-\left((2v-\tfrac{1}{2})\frac{\pi}{2}\right)^2})}{K_0^2(\sqrt{V^2-\left((2v-\tfrac{1}{2})\frac{\pi}{2}\right)^2})}-1\right)J_0^2\left((2v-\tfrac{1}{2})\frac{\pi}{2}\right)$$

. (4.15)

This expression can be simplified as

$$D_v = J_1^2\left((2v-\tfrac{1}{2})\frac{\pi}{2}\right)+\frac{J_0^2\left((2v-\tfrac{1}{2})\frac{\pi}{2}\right)K_1^2(\sqrt{V^2-\left((2v-\tfrac{1}{2})\frac{\pi}{2}\right)^2})}{K_0^2(\sqrt{V^2-\left((2v-\tfrac{1}{2})\frac{\pi}{2}\right)^2})}. \quad (4.16)$$

The derivative of D_ν with respect to ν, D_ν', is defined as

$$D_v{}' = \frac{\partial D_v}{\partial v} = 2\pi J_1\left((2v-\tfrac{1}{2})\frac{\pi}{2}\right)J_1{}'\left((2v-\tfrac{1}{2})\frac{\pi}{2}\right) +$$
$$\frac{2\pi J_0\left((2v-\tfrac{1}{2})\frac{\pi}{2}\right)J_0{}'\left((2v-\tfrac{1}{2})\frac{\pi}{2}\right)K_1^2\left(\sqrt{V^2-\left((2v-\tfrac{1}{2})\frac{\pi}{2}\right)^2}\right)}{K_0^2\left(\sqrt{V^2-\left((2v-\tfrac{1}{2})\frac{\pi}{2}\right)^2}\right)\sqrt{V^2-\left((2v-\tfrac{1}{2})\frac{\pi}{2}\right)^2}}$$
$$-\frac{2\pi J_0^2\left((2v-\tfrac{1}{2})\frac{\pi}{2}\right)K_1\left(\sqrt{V^2-\left((2v-\tfrac{1}{2})\frac{\pi}{2}\right)^2}\right)K_1{}'\left(\sqrt{V^2-\left((2v-\tfrac{1}{2})\frac{\pi}{2}\right)^2}\right)}{K_0^2\left(\sqrt{V^2-\left((2v-\tfrac{1}{2})\frac{\pi}{2}\right)^2}\right)\sqrt{V^2-\left((2v-\tfrac{1}{2})\frac{\pi}{2}\right)^2}}$$
$$+\frac{2\pi J_0^2\left((2v-\tfrac{1}{2})\frac{\pi}{2}\right)K_1^2\left(\sqrt{V^2-\left((2v-\tfrac{1}{2})\frac{\pi}{2}\right)^2}\right)K_0{}'\left(\sqrt{V^2-\left((2v-\tfrac{1}{2})\frac{\pi}{2}\right)^2}\right)}{K_0^3\left(\sqrt{V^2-\left((2v-\tfrac{1}{2})\frac{\pi}{2}\right)^2}\right)\sqrt{V^2-\left((2v-\tfrac{1}{2})\frac{\pi}{2}\right)^2}} \tag{4.17}$$

The derivative of the coupling efficiency with respect to the mode number can thus be expressed in terms of D_v, the mode number, spot size of the input field, and the radius of the MMF core as follows

$$\frac{\partial \eta_v}{\partial v} = 0$$
$$= \frac{2\pi\left((2v-\tfrac{1}{2})\frac{\pi}{2}\right)\left(\frac{\omega}{a}\right)^2 \exp\left[-\frac{1}{2}\left(\frac{\omega^2}{a}\right)\left((2v-\tfrac{1}{2})\frac{\pi}{2}\right)^2\right]D_v - \left(\frac{\omega}{a}\right)^2 \exp\left[-\frac{1}{2}\left(\frac{\omega^2}{a}\right)\left((2v-\tfrac{1}{2})\frac{\pi}{2}\right)^2\right]D_v{}'}{D_v^2} \tag{4.18}$$

The solution of the above equation result in the value of $v=v_p$ that maximizes the

coupling coefficient. This mode is, in general, the most dominant radial mode in the MMF. In order for light within the MMF to be concentrated to on axis location, it is necessary for the phase difference between the peak mode, ν_p, and the previous mode to equal an integer multiple of 2π. Moreover, we predict that the re-imaging condition should be a special case of this criteria, or more specifically, a specific integer multiple of the distance characteristic of a location where field condensation occurs. In the coming paragraphs we will evaluate the validity of the previous statements.

Under the asymptotic formulation given by reference [4.12], the difference in the longitudinal propagation constants between two radial modes, ν_1 and ν_2, can be expressed as follows

$$\left(\beta_{\nu 1} - \beta_{\nu 2}\right) = \frac{u_{\nu 2}^2 - u_{\nu 1}^2}{2k_o a^2 n_{core}}, \tag{4.19}$$

where $u_{\nu 1}$ and $u_{\nu 2}$ are provided in equation (4.11) for the asymptotic formulation for the roots of the 0^{th} order Bessel function. Considering the two modes ν_p and ν_p-1, the phase difference between these two modes can thus be expressed as in the following equation.

$$\left(\beta_{\nu_p - 1} - \beta_{\nu_p}\right) z = \frac{\pi^2 (4\nu_p - 3)}{4k_o a^2 n_{core}} z . \tag{4.20}$$

At the following longitudinal location inside the MMF along the optical axis, z_m,

$$z_m = \frac{8ka^2 n_{core}}{\pi(4v_p - 3)} m = L_p m, \qquad m = 1,2,3,.....$$
$$L_p = \frac{8ka^2 n_{core}}{\pi(4v_p - 3)} \tag{4.21}$$

the phase difference becomes an integer multiple of 2π. L_p corresponds to the location where the phase difference between the two modes equals 2π. Recalling Figure (4.1,b), the upper part shows the Intensity distribution across the MMF calculated using equation (4.3) for the fiber properties mentioned in table (4.1). The lower part of the figure shows the average intensity distribution around the central region normalized to the input intensity. In this portion of this graph, we see pronounced maxima at m=0, 1, 3, 10, 12 and 13. Beside these locations, there are several maxima approximately corresponding to the values of m=2, 5, 8 and 11. This serves to justify the statement made previously that there are several locations, z_m, corresponding to local maxima along the axis of the multimode fiber where field condensation occurs. Although these locations might not be explicit re-imaging locations of the input field, they do correspond to positions where condensing of power along the optical axis occurs.

The explicit re-imaging location where the source input field is duplicated is derived from the representation of the field given in equation (4.3). Looking at the complex field vector contained in this formulation, the phase term can be manipulated by

factoring out the phase term characteristic of the radial mode that has a maximum coupling associated to it, $e^{-i\beta_{v_p} z}$. By doing so, the re-imaging distance can be determined by looking at the resulting phase difference term, $(\beta_v-\beta_{vp})z$. The re-imaging distance is defined as the distance, $z_{re\text{-}imaging}$, that corresponds to when this phase difference between these two guided radial modes equaling an integer multiple of 2π. Therefore, under the asymptotic assumption for the lateral propagation constants, the re-imaging distance can be calculated by formulating an expression for the phase difference between the ν^{th} and ν_p modes as done in equation (4.19).

$$\begin{aligned}\left(\beta_\nu - \beta_{\nu_p}\right)z &= \frac{\pi^2\left[2\left(\nu^2 - \nu_p^2\right)+\left(\nu_p - \nu\right)\right]}{4n_{core}ka^2}z \\ &= 2\pi p, \quad p : Integer\end{aligned} \tag{4.22}$$

Thus, the distance that the two modes must propagate to satisfy the re-imaging conditions can be expressed as

$$z_{re-imaging} = \frac{8n_{core}ka^2}{\pi}. \tag{4.23}$$

In comparing equations (4.21), (4.22), and (4.23), we can see that $z_{re\text{-}imaging}$ is indeed an integer multiple of L_p when expressed in the following manner

$$z_{re-imaging} = (4v_p - 3)L_p . \tag{4.24}$$

Having determined the specific planes inside the MMF where field condensation and re-imaging occurs, it is now necessary to present the use of this device to condense the light exiting the end facet of the MMF. In the next section, we will demonstrate a novel and simple technique that uses the phenomenon discussed above to create a fiber based wavelength tunable condensing lens.

4.1.4. Fiber based wavelength tunable condensing lens

To force light exiting the MMF to converge towards the optical axis, the actual length of the MMF, L_{MMF}, has to be slightly less than the length specified by equation (4.21) for a chosen integer value of m. By doing so, it is possible to determine the locations along the optical axis where field condensation will occur. Phase difference relations can be used to determine these locations by taking into account the propagation within the MMF and the propagation in free space to the locations outside the MMF where the field condensation is observed. The following equation is derived from this phase difference relation keeping in mind that the propagation constants are wavelength dependent

$$z_{out} = \frac{2\pi m - L_{MMF}\left(\beta_{vp-1} - \beta_{vp}\right)}{\beta_{out,vp-1} - \beta_{out,vp}}. \tag{4.25}$$

From continuity of the tangential component of the wave vector, the associated longitudinal propagation constant of a particular mode after exiting the MMF can be determined using the formula below in terms of the longitudinal propagation constant inside the MMF

$$\beta_{out,v} = \sqrt{k_o^2\left(1 - n_{core}^2\right) + \beta_v^2}\ . \tag{4.26}$$

In formulating equation (4.22), the phase term associated with the mode that has a maximum coupling was factored out of the field representation in equation (4.3) resulting in a particular phase difference term. In order to determine a 1st order formulation for equation (4.25), the same phase term factoring approach can be adopted, only for approximation purposes the phase term associated with the fundamental mode is factored out. In doing so, the same asymptotic approximations made previously can be applied to the $(\beta_1-\beta_v)$ term contained within the phase difference expression for the field as done in equation (4.22). β_v can be isolated from this relationship and substituted back into equation (4.22). Thus, the longitudinal propagation constant of a particular mode after exiting the MMF into free-space can be formulated as follows

$$\beta_{out,\nu} = \sqrt{k^2 - n_{core}^2 k_o^2 + \beta_1^2 - \frac{2\beta_1(2\nu+1)(\nu-1)2\pi}{z_{re-imaging}} + \left(\frac{(2\nu+1)(\nu-1)2\pi}{z_{re-imaging}}\right)^2} \quad . \tag{4.27}$$

Assuming that the fundamental longitudinal propagation constant can be approximated as ($k_o n_{core}$) and that the last squared term in equation (4.27) is much smaller than the other terms under the square root, this equation can be simplified into the following equation

$$\begin{aligned} \beta_{out,\nu} &= k_o \sqrt{1 - \frac{2n_{core}(2\nu+1)(\nu-1)2\pi}{z_{re-imaging}}} \\ &\cong k_o - \frac{n_{core}(2\nu+1)(\nu-1)2\pi}{z_{re-imaging}} \end{aligned} \quad . \tag{4.28}$$

This approximate formulation for the longitudinal propagation constants outside the MMF can be used to form the expression for the $\beta_{out,vp-1} - \beta_{out,vp}$ term included in equation (4.25). Along with the expression for $\beta_{vp-1} - \beta_{vp}$ in equation (4.20), equation (4.25) can be manipulated into the following equation for the locations along the optical axis where field condensation of the light exiting the MMF occurs

$$z_{out} = \frac{2\pi m - L_{MMF}\left(\frac{(4v_p - 3)2\pi}{z_{re-imaging}(\lambda)}\right)}{\frac{n_{core}(4v_p - 3)\pi}{z_{re-imaging}(\lambda)}} \quad . \tag{4.29}$$

Using the relation defined for L_p in equation (4.21), the above equation can be rewritten into a more compact form in terms of L_p, the actual length of the MMF used, and the core refractive index

$$z_{out} = \frac{mL_p - L_{MMF}}{n_{core}}. \tag{4.30}$$

In terms of the fiber parameters and the wavelength, equation (4.30) can be written as follows

$$z_{out} = m\frac{16a^2}{(4v_p - 3)\lambda} - \frac{L_{MMF}}{n_{core}}. \tag{4.31}$$

Due to the finite wavelength range that the source can be tuned, we operate over a specific range of wavelengths around a central wavelength, λ_o. Assuming that the value of v_p doesn't change within this range of wavelength, equation (4.31) is expanded around the central wavelength using a Taylor expansion as follows

$$z_{out} = \left(m\frac{32a^2}{(4v_p - 3)\lambda_o} - \frac{L_{MMF}}{n_{core}} \right) - m\frac{16a^2}{(4v_p - 3)\lambda_o^2}\lambda + O(\lambda^2). \tag{4.32}$$

It is important to look at how z_{out} changes as certain system parameters are varied. In particular, it is clear that this output distance exhibits inherent wavelength dependence. . Using the formulation above, the derivative of z_{out} relative to the wavelength demonstrates that it is approximately constant with respect to the varying wavelength as follows

$$\frac{\partial z_{out}}{\partial \lambda} = -m \frac{16a^2}{(4\nu_p - 3)\lambda_o^2}. \tag{4.33}$$

Another influencing system parameter is the radius of the MMF, a, because the peak mode index ν_p, and L_{MMF} depend strongly on the MMF radius. For a specific wavelength, λ_o, z_{out} changes considerably when the MMF radius is varied as demonstrated in the following equation

$$\frac{\partial z_{out}}{\partial a} = -m \frac{32a}{(4\nu_p - 3)\lambda_o} + m \frac{64a^2}{(4\nu_p - 3)^2 \lambda_o} \frac{\partial \nu_p}{\partial a} - \frac{1}{n_{core}} \frac{\partial L_{MMF}}{\partial a}. \tag{4.34}$$

As the radius of the MMF changes, ν_p changes according to equation (4.14). That changes the location of the working maximum, and thus the proper MMF length, L_{MMF}. Using the fiber material parameters in table (4.1), the change of L_{MMF} as a function of the core radius is depicted in Figure (4.3). L_{MMF} is assumed to be 0.95 of the length corresponding to the peak at $(\nu_p\text{-}1)L_p$.

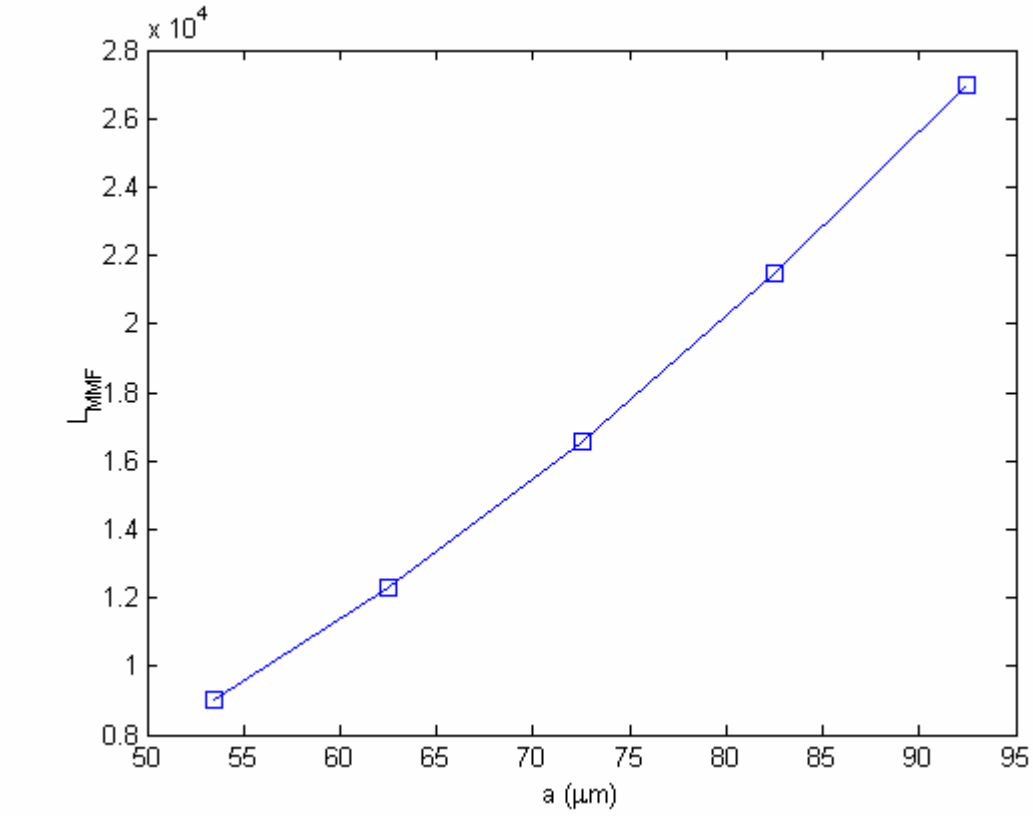

Figure 4. 3: Change of L_{MMF} versus the MMF radius a. L_{MMF} is considered to be 0.95 of the re-imaging distance inside the MMF.

Now that the locations outside the MMF where field condensation will occur have been identified, in order to estimate the spot size at the focal plane, we need to calculate the intensity distribution outside the MMF. The series expansion in equation (4.3) can be used with a modification in the phase term to compensate for the free space propagation. In addition, we can neglect the field expansion in the cladding region as most of the power is concentrated in the central region. Thus, the output field can be written as

$$E_{out}(r, L_{MMF} + z_{out}) = \sum_{v=1}^{N} \sqrt{\eta_v} J_0(u_v \frac{r}{a}) \, e^{-i(\beta_v L_{MMF} + \beta_{,ou,vi} z_{out})}, \quad (4.35)$$

where $\beta_{out,v}$ is the longitudinal propagation constant for the v^{th} order mode in air as defined in equation (4.28).

In this section, we have demonstrated a novel application of selective mode excitation without using any additional optical elements. By direct coupling of the light from a SMF to MMF, only radial modes are exited in the MMF. Properly selecting the length of the MMF, the device can be utilized as a wavelength tunable condensing lens. However, for other type of applications, we might need to add extra optical elements. For instance, selective excitation of certain higher order modes in few modes fiber requires at least one phase element to match the phase profile of the desired mode. In the next section, we will explain in details the design and analysis of single phase element for selective excitation of the LP_{11} and LP_{21} modes in few modes step index fiber.

4.2. Single Phase Elements

Figure (3.1) shows the first three higher order modes in few modes fiber. The phase profiles of these modes are orthogonal to each other. Consider two functions with radial symmetric amplitudes, and their phase profiles match two different modes. Although the amplitudes might not be orthogonal to each other, the cross correlation

between these two functions vanishes. However, this integral is maximized when the two phases match. Thus, to selectively couple to a certain linearly polarized mode, $LP_{v,m}$, the phase field at the input facet of the MMF has to match that mode. This can be achieved through placing a phase element with a phase profile equivalent to that of the desired mode in the path of the input light. In spite of the fact that one mode has been selectively excited inside the MMF its coupling efficiency might not necessary reach 100%. The coupling efficiency to any particular mode can be calculated through the overlap integral represented by equation (3.5) where, $E_s(r,\theta)$ is the field profile at the input facet of the fiber.

For a step index fiber of core radius a and a working wavelength λ the field distribution of the guided linearly polarized modes can be represented as in (4.4) and (4.6) [41]

$$\psi_{v,m}(r,\theta,z) = \begin{cases} c_{v,m} J_m(u_{v,m}\frac{r}{a})\cos(m\theta)\, e^{-i\beta_{v,m}z} & r \le a \\ c_{v,m}\frac{J_m(u_{v,m})}{K_m(w_{v,m})} K_m(w_{v,m}\frac{r}{a})\cos(m\theta)\, e^{-i\beta_{v,m}z} & r > a \end{cases}. \qquad (4.36)$$

In equation (4.36), the suffixes v and m are the indices for the guided radial and azimuthal components respectively, and $c_{v,m}$ is the excitation coefficient of the $LP_{v,m}$ mode as mentioned in the previous section. It is defined as the square root of the power coupling coefficient, $\eta_{v,m}$, represented by the following overlap integral

$$\eta_{v,m} = \frac{\left| \int_0^{2\pi} \int_0^{\infty} E_{in}(r,\theta) \cdot \psi_{v,m}(r,\theta,0)^* \, r dr d\theta \right|^2}{\int_0^{2\pi} \int_0^{\infty} \left| E_{in}(r,\theta) \right|^2 r dr d\theta \int_0^{2\pi} \int_0^{\infty} \left| \psi_{v,m}(r,\theta,0) \right| r dr d\theta}, \tag{4.37}$$

where, $E_{in}(r,\theta)$ is the field profile at the input facet of the fiber. Figure (3.1) depicts the amplitude and phase profiles of the first few linearly polarized modes. Upon closer inspection of the phase profiles of these modes, one notices that they are orthogonal to each other. Thus, in order to selectively excite one particular mode, it is sufficient to match the phase profile of that specific mode. This can be achieved through phase modulation of the input field by placing a proper phase element in its path as shown in Figure (4.4). In this setup, the first lens collimates the light out of the single mode fiber (SMF), and the second lens focuses the phase modulated light to the input facet of a larger core fiber that sustains more than one mode. We will refer to this fiber as a large core fiber hence forth.

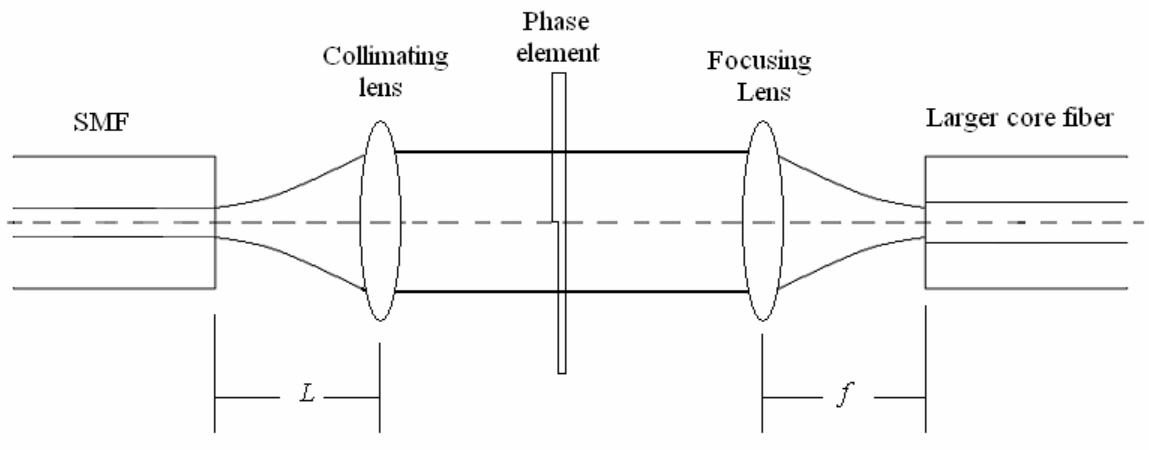

Figure 4. 4: The coupling scheme showing the phase element placed in the path of the input beam.

Proper selection of the focal length of the focusing lens has a great impact on achieving high coupling efficiency to the desired mode as we will present later in this section.

For the coupling scheme presented in Figure (4.4), the light out of the SMF is assumed to be Gaussian with a beam waist defined as [39]

$$w_S = a_S\left(0.65 + 1.619V_S^{-1.5} + 2.879V_S^{-6}\right). \tag{4.38}$$

In equation (4.38), a_S and V_S are the SMF radius and it's V-number respectively. The field immediately after the collimating lens has a beam waist of

$$w_g = w_S \sqrt{1 + \left(\frac{L\lambda}{\pi w_S^2} \right)^2} \quad . \tag{4.39}$$

Assuming perfect collimation, the beam waist at the phase element will be w_g as well.

In this section we present two coupling elements with phase profiles match that of the LP_{11} and LP_{21} respectively. The phase coupling whose a phase profile identical to that of the LP_{11} mode has a transmittance, *T(x,y)*, which can be represented by a sign function as follows

$$T_{11}(x, y) = sign(x) \,, \tag{4.36}$$

where

$$sign(x) = \begin{cases} 1 & x > 0 \\ 0 & x = 0 \\ -1 & x < 0 \end{cases} . \tag{4.37}$$

The field distribution at the input of the fiber can be calculated using Fresnel approximation as follows

$$E_{in}(x, y) = \frac{1}{i\lambda f} \int_{x'=-\infty}^{\infty} \int_{y'=-\infty}^{\infty} sign(x')\, Exp(-\frac{x'^2 + y'^2}{2w_g{}^2}) \times Exp\left(-i2\pi(\eta_x x' + \eta_y y')\right) dx'dy' \quad . \tag{4.38}$$

Equation (4.38) can be simplified as

$$E_{in}(x,y) = -\frac{2w_g^2}{i\lambda f} Exp(-2\pi w_g^2 \eta_y^2) \cdot \left(Exp(-2\pi w_g^2 \eta_x^2) \otimes \frac{1}{\eta_x} \right), \quad \textbf{where } \eta_x = \frac{x}{\lambda f} \textbf{ and } \eta_y = \frac{y}{\lambda f} \tag{4.39}$$

In equation (4.39), λ is the working wave length and $\otimes$ is the convolution operator. The convolution in equation (4.39) can be written as

$$\left(Exp(-2\pi w_g^2 \eta_x^2) \otimes \frac{1}{\eta_x} \right) = \int_{-\infty}^{\infty} \frac{e^{-\left(t^2 2\pi w_g^{2^2}\right)}}{\eta_x - t} dt \tag{4.40}$$

This integration can be split in two parts as follows

$$\begin{aligned} \left(Exp(-2\pi w_g^2 \eta_x^2) \otimes \frac{1}{\eta_x} \right) &= \left[\int_{0}^{\infty} \frac{e^{-\left(t^2 2\pi w_g^{2^2}\right)}}{\eta_x - t} dt + \int_{-\infty}^{0} \frac{e^{-\left(t^2 2\pi w_g^{2^2}\right)}}{\eta_x - t} dt \right] \\ &= \left[-\int_{0}^{\infty} \frac{e^{-\left(t^2 2\pi w_g^{2^2}\right)}}{(-\eta_x) + t} dt + \int_{0}^{\infty} \frac{e^{-\left(t^2 2\pi w_g^{2^2}\right)}}{\eta_x + t} dt \right]. \end{aligned} \tag{4.41}$$

Knowing that [42]

$$\int_0^{\infty} \frac{e^{-at^2}}{x+t}\,dt = e^{-ax^2}\left[\sqrt{\pi}\int_0^{\sqrt{a}\,x} e^{t^2}\,dt - \frac{1}{2}Ei(ax^2)\right], \tag{4.42}$$

where *Ei* is the exponential integral defined as

$$Ei(x) = \int_{-\infty}^{x} \frac{e^t}{t}\,dt\,, \tag{4.43}$$

equation (4.41) can be represented as

$$\begin{aligned}\left(Exp(-2\pi^2 w_g^2 \eta_x^2) \otimes \frac{1}{\eta_x}\right) = \left[-e^{-\left(2\pi^2 w_g^2 \eta_x^2\right)}\left[\sqrt{\pi}\int_0^{-\sqrt{2}\pi w_g \eta_x} e^{t^2}\,dt - \frac{1}{2}Ei(2\pi^2 w_g^2 \eta_x^2)\right] + \right. \\ \left. e^{-\left(2\pi^2 w_g^2 \eta_x^2\right)}\left[\sqrt{\pi}\int_0^{\sqrt{2}\pi w_g \eta_x} e^{t^2}\,dt - \frac{1}{2}Ei(2\pi^2 w_g^2 \eta_x^2)\right]\right]\end{aligned} \tag{4.44}$$

This is simplified to

$$\left(Exp(-2\pi^2 w_g^2 \eta_x^2) \otimes \frac{1}{\eta_x}\right) = \pi\, e^{-\left(2\pi^2 w_g^2 \eta_x^2\right)}\,\mathrm{erfi}\left(\sqrt{2}\pi w_g \eta_x\right), \tag{4.45}$$

where erfi(z) (referred to as imaginary error function) is defined as

$$\mathrm{erfi}(z) = \frac{2}{\sqrt{\pi}} \int_0^z e^{t^2}\, dt\,. \tag{4.46}$$

Thus, the field in equation (4.39) can be written as

$$E_{in}(\eta_x, \eta_y) = \frac{2\pi w_g^2}{i\lambda f} e^{-\left(2\pi^2 w_g^2 (\eta_x^2 + \eta_y^2)\right)} \cdot \mathrm{erfi}\left(\sqrt{2}\pi w_g \eta_x\right). \tag{4.47}$$

Substituting η_x and η_y in terms of x and y, equation (4.47) is written as

$$E_{in}(r, \theta) = \frac{2i\pi w_g^2}{\lambda f} e^{-\left(\frac{x^2+y^2}{2w_G^2}\right)} \cdot \mathrm{erfi}\left(\frac{x}{\sqrt{2}w_G}\right).$$
$$w_G = \frac{\lambda \cdot f}{2\pi w_g} \tag{4.48}$$

In equation (4.48), f represents the effective focal length of the second lens in Figure (4.4), and k is the wave number of the light, $\frac{2\pi}{\lambda}$. Notice that we used the Cartesian coordinates to represent both the phase transmittance of the coupling element and the field at the input of the large core fiber. However, it is more convenient to use polar coordinates in this cylindrical symmetric structure. Defining the following normalized polar coordinates

$$\rho = \sqrt{\frac{x^2 + y^2}{2w_G^2}}, \qquad \theta = \tan^{-1}\left(\frac{y}{x}\right) \tag{4.49}$$

equation (4.48) can be written as follows

$$E_{in}(\rho,\theta) = \frac{2i\pi w_g^2}{\lambda f} e^{-(\rho^2)} \cdot \mathrm{erfi}(\rho\cos\theta). \tag{4.50}$$

The amplitude and phase distributions of E_{in} are depicted in Figure (4.5). Notice that the phase profile matches that of the LP_{11} mode presented in Figure (3,e). However, the amplitude differs from that presented in Figure (3.b). This amplitude mismatch reduces the coupling efficiency to the LP_{11} mode.

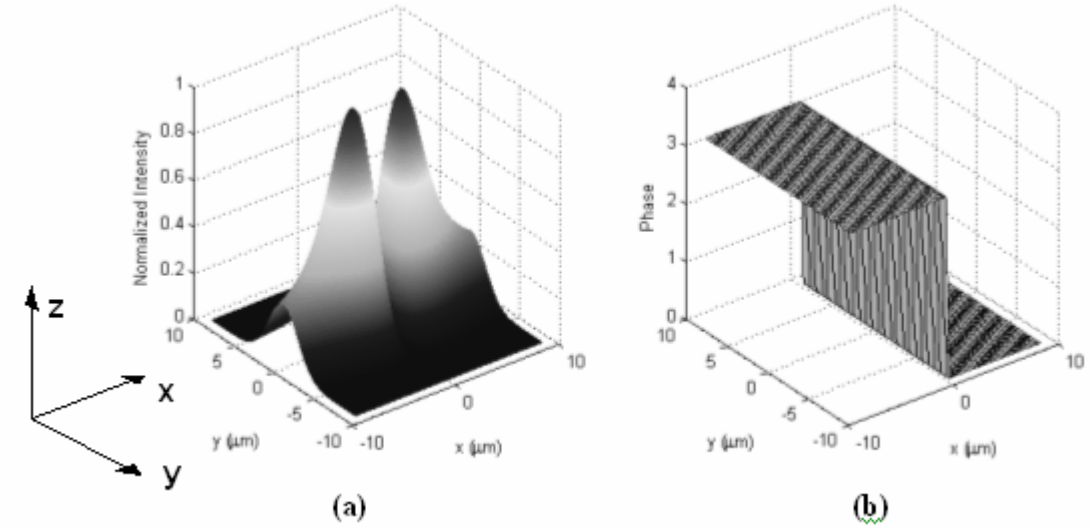

Figure 4. 5: The calculated (a) Amplitude and (b) phase profiles of the field at the input facet of the larger core fiber.

The coupling efficiency is calculated through the overlap integration in equation (4.37). Equation (4.37) can be written as

$$\eta_{11} = \frac{\left|N_f\right|^2}{D_1 \cdot D_2}, \tag{4.51}$$

where

$$N_f = \int_0^{2\pi} \int_0^{a/\sqrt{2}w_G} e^{-(\rho^2)} \cdot \mathrm{erfi}(\rho\cos\theta) \cdot J_m(b_{11}\rho)\rho d\rho d\theta + \int_0^{2\pi} \int_{a/\sqrt{2}w_G}^{\infty} e^{-(\rho^2)} \cdot \mathrm{erfi}(\rho\cos\theta) \cdot \left(\frac{J_m(u_{11})}{K_m(w_{11})}\right) K_m(c_{11}\rho)\rho d\rho d\theta, \tag{4.52}$$

$$D_1 = \int_0^{2\pi} \int_0^{\infty} \left| e^{-(\rho^2)} \cdot \mathrm{erfi}(\rho\cos\theta) \right|^2 \rho d\rho d\theta \cdot \tag{4.53}$$

and

$$D_2 = \int_0^{2\pi} \int_0^{a/\sqrt{2}w_G} \left|J_m(b_{11}\rho)\right|^2 \rho d\rho d\theta + \int_0^{2\pi} \int_{a/\sqrt{2}w_G}^{\infty} \left| \left(\frac{J_m(u_{11})}{K_m(w_{11})}\right) K_m(c_{11}\rho) \right|^2 \rho d\rho d\theta . \tag{4.54}$$

In equations (4.51) through (4.54), b_{11} and c_{11} are defined as

$$\begin{aligned} b_{11} &= \frac{u_{11}\sqrt{2}w_G}{a} \\ c_{11} &= \frac{w_{11}\sqrt{2}w_G}{a} \end{aligned}. \tag{4.55}$$

Equation (4.52) can be simplified by expanding the error function in a polynomial series around zero as

$$\operatorname{erfi}(z) = \frac{2}{\sqrt{\pi}} \sum_{n=0}^{\infty} \frac{(z)^{2n+1}}{n!(2n+1)}. \tag{4.56}$$

Using this expansion, Equation (4.52) can be written as

$$N_f = \frac{2}{\sqrt{\pi}} \sum_{n=0}^{\infty} \frac{1}{n!(2n+1)} \left(\int_0^{2\pi} (\cos\theta)^{2n+1} d\theta \right) \left(\int_0^{\infty} e^{-(\rho^2)} \cdot \psi_{11}(\rho) \rho^{2n+2} d\rho \right), \tag{4.57}$$

where, $\psi_{11}(\rho)$ is the LP_{11} mode radial dependant term defined as

$$\psi_{11}(\rho) = \begin{cases} J_1(b_{11}\rho) & \rho \le a/\sqrt{2}w_G \\ \left(\dfrac{J_1(u_{11})}{K_1(w_{11})} \right) K_1(c_{11}\rho) & \rho > a/\sqrt{2}w_G \end{cases}. \tag{4.58}$$

A closed form solution numerator, N_f, is obtained by, first, carrying out the integration over θ as shown in equation (4.57). It has the following closed form solution

$$\int_0^{2\pi} (\cos\theta)^{2n+1} d\theta = \frac{\Gamma(1/2)\Gamma\left(\frac{5}{2}+n\right)}{(3+2n)\Gamma(2+n)n!(2n+1)}. \tag{4.59}$$

In the second integration, a closed form solution is obtained by approximating $\psi_{11}(\rho)$ by a first order Hermite-Gaussian as follows [29]

$$\psi_{11}(\rho) \approx p_1 \rho e^{-(p_2\rho^2)}, \tag{4.60}$$

where p_1 *and* p_2 are constants. The values of these constants can be obtained by applying two constraints. First, the areas under both curves are equal,

$$\int_0^{\infty} \psi_{11}(\rho)\, d\rho = \int_0^{\infty} p_1 \rho e^{-(p_2\rho^2)} d\rho. \tag{4.61}$$

Applying this constraint, we obtain the following linear relation between the two constants

$$p_2 = \frac{p_1}{2\int_0^{\infty} \psi_{11}(\rho)d\rho}. \tag{4.63}$$

The integration in the denominator has the following solution [42]

$$\begin{aligned}\int_0^{\infty} \psi_{11}(\rho)d\rho &= c_{11}\int_0^{a/\sqrt{2}w_g} J_1(b_{11}\rho)d\rho + A\left(\frac{J_1(u_{11})}{K_1(w_{11})}\right)\int_{a/\sqrt{2}w_g}^{\infty} K_1(c_{11}\rho)d\rho \\ &= c_{11}\left(\frac{(1-J_0(u_{11}))}{b_{11}} + w_{11}\left(\frac{J_1(u_{11})}{K_1(w_{11})}\right)K_0(w_{11})\right)\end{aligned}, \tag{4.64}$$

Thus

$$p_1 = h\ p_2, \tag{4.65}$$

where

$$h = 2A\left(\frac{(1-J_0(u_{11}))}{b_{11}} + \left(\frac{J_1(u_{11})}{K_1(w_{11})}\right)\frac{K_0(w_{11})}{c_{11}}\right) \tag{4.66}$$

In the second constraint, the value of p_2 is obtained by minimizing the profile amplitude error, δR, defined as

$$\delta R = \psi_{11}(\rho) - h\ p_2 \rho\ e^{-p_2\rho^2}. \tag{4.67}$$

Several optimization techniques can be used to solve for the p_2 coefficient. In this work we used the least square error method. In this method p_2 is represented as a combination of two parts,

$$p_2 = \tilde{p}_2 + \Delta p_2 . \tag{4.68}$$

In equation (4.68), $\tilde{p}_2$ is assumed to result in zero error. Using this assumption and using the first order expansion of the Hermite-Gaussian function around $\tilde{p}_2$, equation (4.67) can be written as

$$\delta R = \left(h\rho\, e^{-p_2\rho^2} - h\, p_2 \rho^3\, e^{-p_2\rho^2} \right) \Delta p_2 . \tag{4.69}$$

By discretizingρ, equation (4.69) can be written in a vector form as follows

$$\overline{R} = \overline{M} \cdot \Delta p_2 . \tag{4.70}$$

In equation (4.70), vectors $\overline{R}$, and $\overline{M}$ represent the error, the term between brackets on the right hand side in equation (4.69). The value of Δp_2 is obtained as follows

$$\Delta p_2 = \frac{\left(\overline{M}^T \cdot \overline{R}\right)}{\left(\overline{M}^T \cdot \overline{M}\right)}. \tag{4.71}$$

The initial value of p_2 is then updated

$$p_2^{new} = p_2^{old} - \Delta p_2 . \tag{4.72}$$

These steps are then repeated till p_2 converges. Using this representation, the integration over ρ can be written as

$$\int_0^\infty e^{-\left(\rho^2\right)} \cdot \psi_{11}(\rho) \rho^{2n+2} d\rho = \int_0^\infty \rho^{2n+3}\, e^{-(p_2+1)\rho^2}\, d\rho \tag{4.73}$$

Using the following relation

$$\int_0^\infty t^\mu\, e^{-\sigma t^2}\, dt = -\frac{\sigma^{-(1-\mu)/2}}{2} \Gamma\left(\frac{1+\mu}{2}\right), \tag{4.74}$$

equation (4.73) has the following solution

$$\int_0^\infty e^{-\left(\rho^2\right)} \cdot \psi_{11}(\rho) \rho^{2n+2} d\rho = \frac{(p_2+1)^{-(n+1)}}{2} \Gamma\left(\frac{1+\mu}{2}\right) \tag{7.75}$$

Substituting equations (4.59) and (4.75) in (4.75), we obtain

$$N_f = p_1 \sum_{n=0}^{\infty} \frac{\sqrt{\pi}(n+1)(2n)!}{2^n n!}(p_2+1)^{-(1+n)} \tag{7.76}$$

In the denominator, the first integral, D_1, is very difficult to be solved analytically. However, neglecting the Fresnel losses from the phase element and the lens, we can apply Parseval's theory since E_{in} is proportional to the Fourier transform of the input Gaussian beam phase modulated by the coupling element. Thus,

$$D_1 = \frac{\pi w_g^2}{\lambda^2 f^2}. \tag{7.77}$$

The Second integral in the denominator part of equation (4.51) has the following solution

$$D_2 = \pi a^2 H(u_{11}, w_{11}), \tag{7.78}$$

where

$$H(u_{11}, w_{11}) = \left[J_1^2(u_{11}) - J_0(u_{11})J_2(u_{11})\right] + \left(\frac{J_1(u_{11})}{K_1(w_{11})}\right)\left[K_0(w_{11})K_2(w_{11}) - K_1^2(w_{11})\right]. \tag{7.79}$$

Substituting equation (4.76), (4.77) and (4.78) into (4.51) and we obtain the following expression for the coupling efficiency

$$\eta_{11} = \frac{\lambda^2 f^2 \left| p_1 \right|^2 \left| \sum_{n=0}^{\infty} \frac{\sqrt{\pi}(n+1)2n!}{2^n n!} (p_2+1)^{-(1+n)} \right|^2}{\pi^2 w_g^2 a^2 H(u_{11}, w_{11})}. \tag{7.80}$$

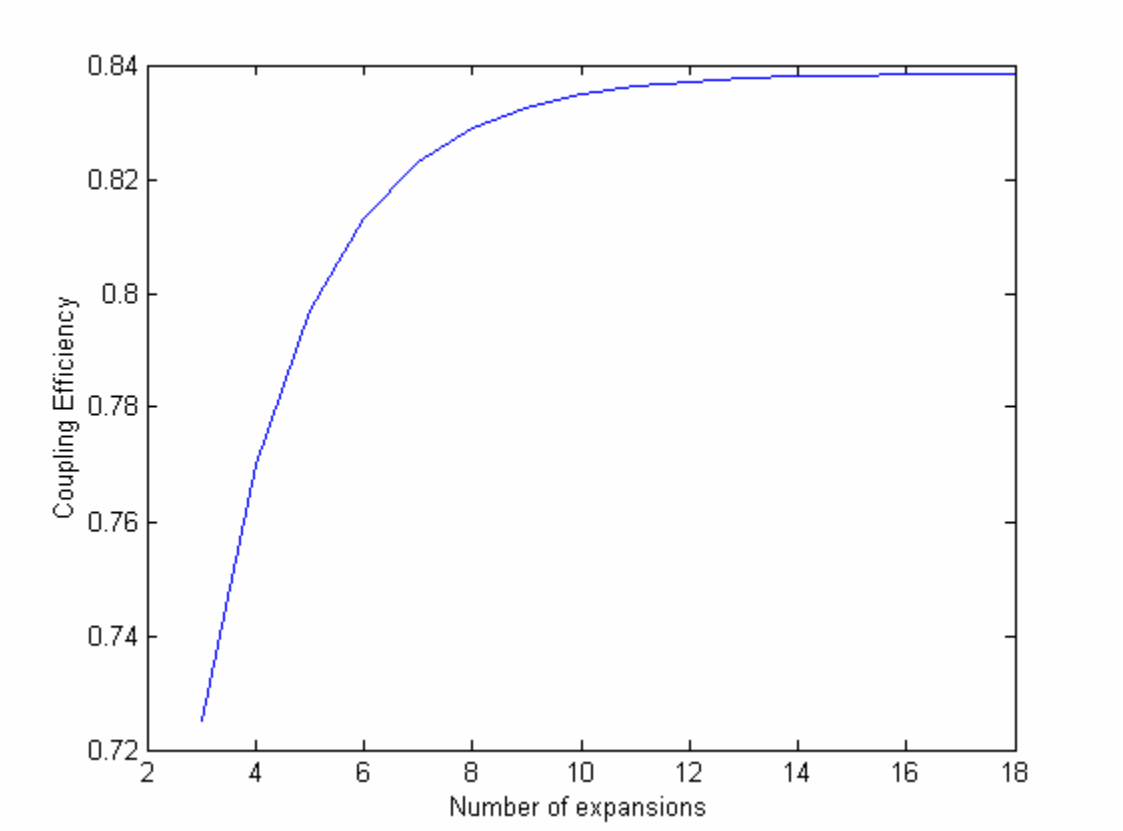

Figure 4. 6: The coupling efficiency to the LP_{11} mode as a function of the number of expansions.

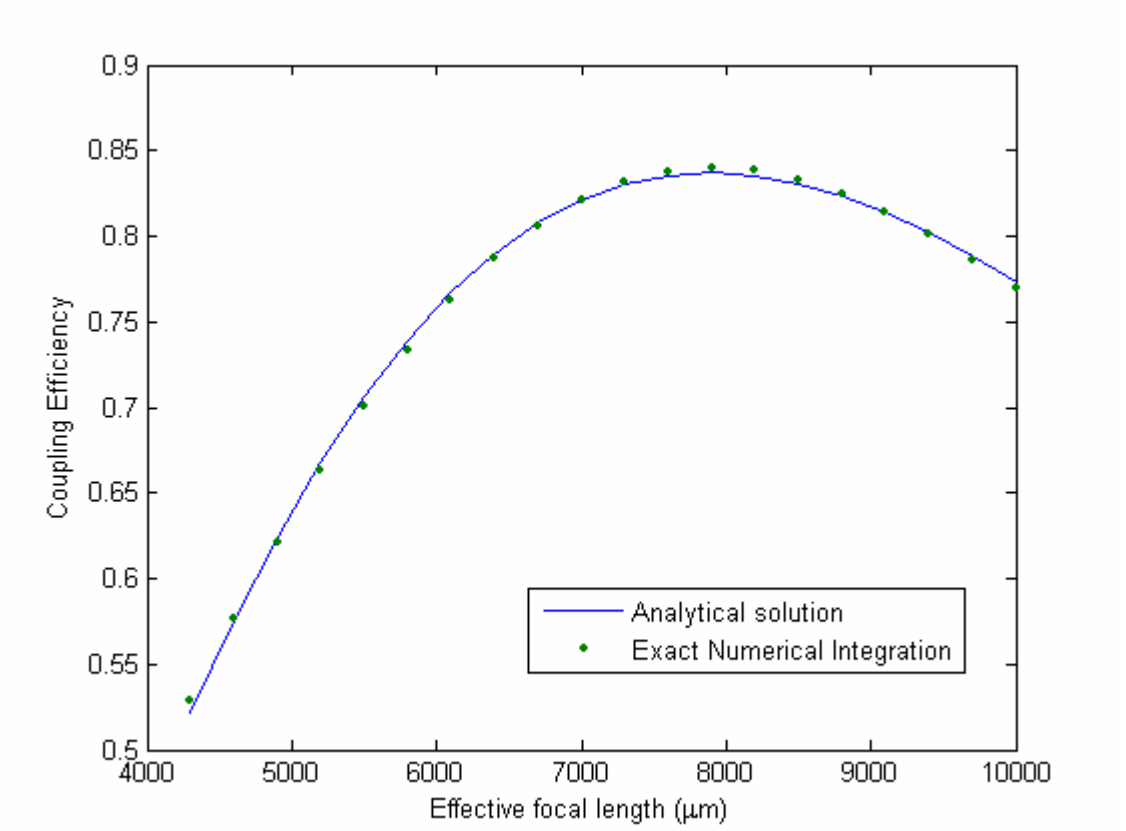

Figure 4. 7: Coupling Efficiency vs. the effective focal length of the few modes fiber objective using exact numerical integration in equation (4.14) and the analytical solution in equation (4.48).

This expression is represented in terms of an infinite series. However, a few expansion terms might only be needed to obtain a precise value of η_{11}. Figure (4.6) depicts the coupling efficiency as a function of the number of expansion terms. In these calculations we consider an effective focal length, f, of 8 mm for the focusing lens. The figure shows that by including more than 16 expansion terms into the efficiency calculation, the

calculated value of η_{11} converges to a stable value. Therefore, in the rest of this work we use 16 expansion terms to evaluate η_{11} when using the expression in (4.80). To predict the accuracy of this expression, we compare the exact numerical calculation of the overlap integral in (4.37) and equation (4.80) as a function of f. These results are depicted in Figure (4.7).

In the numerical calculations, E_{in} is computed through the Fresnel propagation of the input Gaussian beam phase modulated by the coupling element through the second lens. The figure shows a good agreement between both cases. However, the slight difference in the graphs is mainly due to the first order Hermite-Gaussian approximation as presented in equation (4.60). Additionally, the graphs show that the coupling efficiency is maximized around f = 8 mm. This seems contradictory with equation (4.80) due to the presence of f^2 in the numerator. The explanation for the maximization of η_{11} at a specific effective focal length value can be traced to the formulation of p_1 and p_2. However, constants p_1 and p_2 implicitly depend on f through b_{11}, c_{11}, and w_g as presented in equations (4.55), and (4.65). Figure (4.8) shows the values of p_1 and p_2 as a function of f. Notice that both p_1 and p_2 increases with f. Similarly, the transmittance of the phase element required to excite the LP_{21} is

$$T_{21}(x,y) = sign(x) \cdot sign(y), \tag{4.82}$$

and the resulting field distribution at the input facet of the fiber is

$$E_{in}(r,\theta) = \frac{2\pi^2 w_g^2}{i\lambda f}\,\mathrm{erfi}(\rho\sin\theta)\cdot\mathrm{erfi}(\rho\cos\theta)\,. \tag{4.83}$$

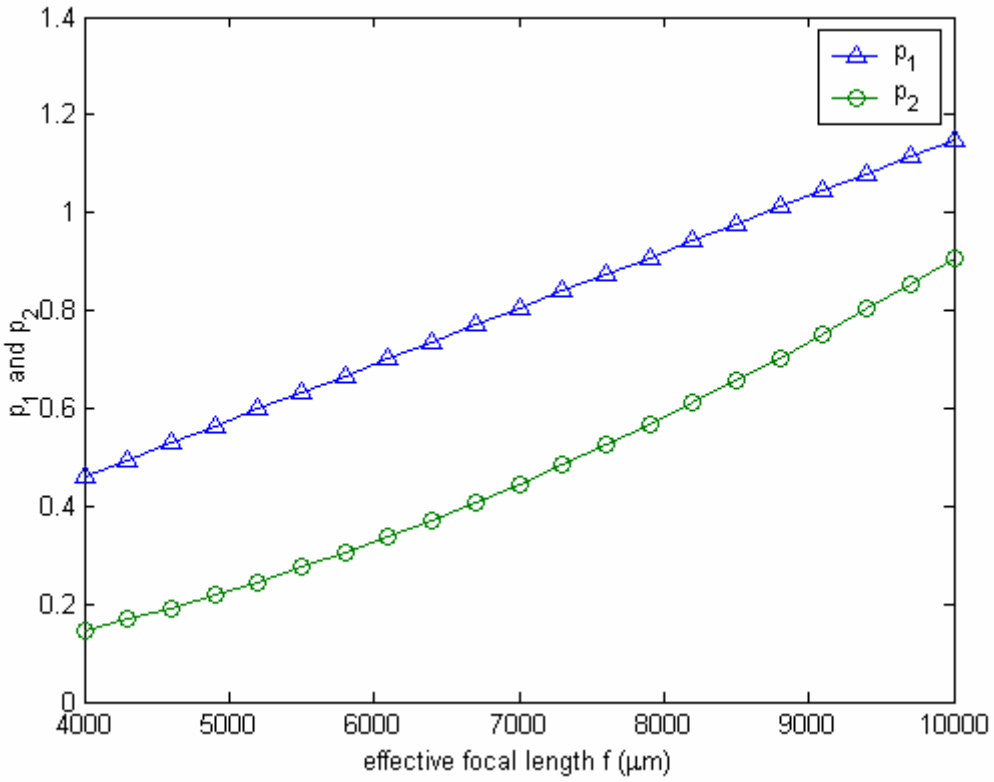

Figure 4. 8: Dependence on values of p_1 and p_2 on effective focal length showing increasing relationship for both parameters.

Again, the phase profile of this field matches that of the LP_{21} while the amplitude differs. For the used focal length of 9 mm, the calculated coupling efficiencies using equation (4.81) is 81.47% while it is 83.41% using the numerical integration. Using equation (4.14) the coupling efficiency for the LP_{21} mode is about 60%.

4.3. Dual elements

Dual elements are two phase elements aligned on the front and back sides of a substrate material such as fused silica wafer as depicted in Figure (4.9). The coupling scheme is depicted in Figure (4.10). In this scheme, the first element modulates the amplitude of the incident beam and the second one fixes the phase profile. However, designing the first phase is the main challenge. This section demonstrates two design techniques. The least square error method and Method of projection (MOP). In the first method, the phase surface of the first element is fitted to a two-dimensional polynomial expansion, while within the MOP method the phase of the first element is numerically calculated.

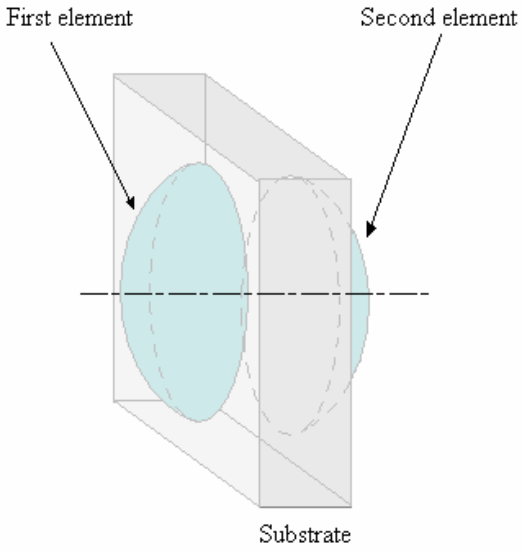

Figure 4. 9: Dual element structure.

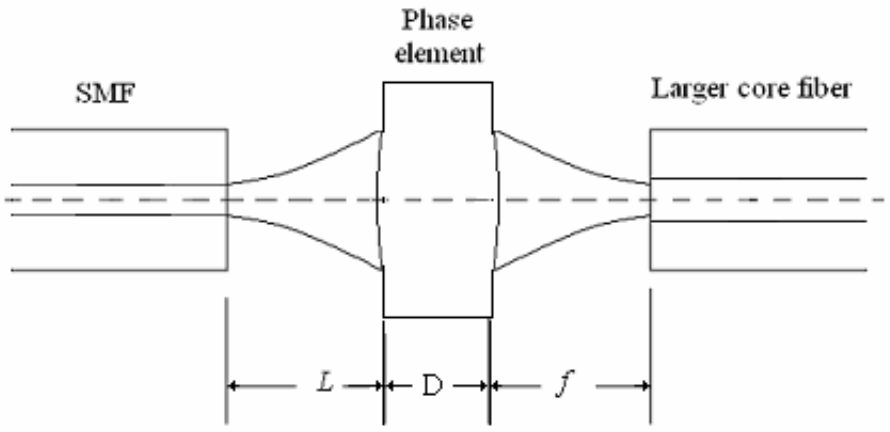

Figure 4. 10: Dual elements coupling scheme.

4.3.1. Least Square Error method

In this method, the phase surface of the first element is represented by a two dimensional polynomial expansion as depicted in equation (4.84).

$$\phi_1(x,y) = \sum_h \sum_k a_{h,k} x^h y^k \quad , h = 0,1,..,N \text{ and } k = 0,1,...,M \tag{4.84}$$

Considering an input Gaussian beam, $E_g(x,y)$, of specific beam width, w_g, the goal is to minimize the difference between the intensity distributions of the output field at a certain observation plane, $I(a_{h,k},x,y)$, and the target intensity, $I_o(x,y)$.

$$dI(x,y) = I_o(x,y) - I(a_{h,k},x,y) \tag{4.85}$$

The second element corrects for the phase of the field at the observation plane. Figure (4.11) depicts a schematic diagram of the method.

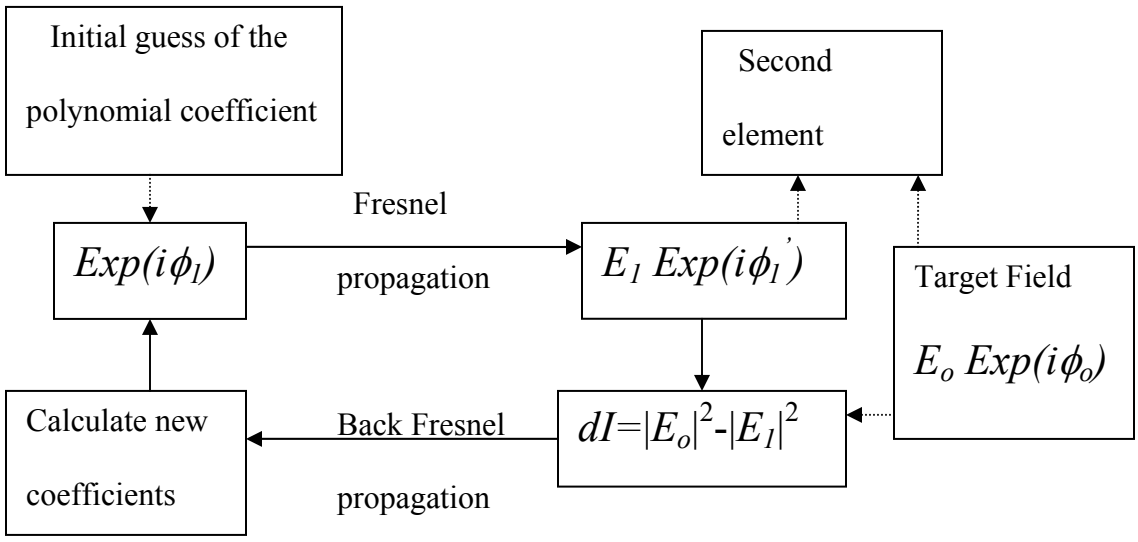

Figure 4. 11: Schematic diagram of the diffractive element design method.

The field distribution at the observation plane using the above scheme can be written as

$$E(a_{h,k},x,y) = \int_x \int_y E_g(x,y) Exp\left(\frac{ik(x^2+y^2)}{2\lambda z}\right) Exp\left(i\sum_h \sum_k a_{h,k} x^h y^k\right) dxdy\,, \tag{4.86}$$

where λ, k, and z are the working wavelength, the wave number and the propagation distance respectively. The intensity distribution at this plane is

$$I(a_{h,k}, x, y) = E(a_{h,k}, x, y) \cdot E(a_{h,k}, x, y)^{*}. \tag{4.87}$$

Using equation (4.86) and representing the coefficient $a_{h,k}$ as a summation of the desired value, $\tilde{a}_{h,k}$, and a displacement of $\Delta a_{h,k}$, equation (4.85) can be written as

$$dI(x, y) = \sum_{h} \sum_{k} \Delta a_{h,k} \frac{\partial I(a_{h,k}, x, y)}{a_{h,k}}. \tag{4.88}$$

Writing equation (4.88) in a matrix form, one obtains the following expression

$$\mathbf{dI} = \mathbf{M} \cdot \mathbf{\Delta} a \,. \tag{4.89}$$

In equation (4.89), matrices **dI**, **M,** and $\Delta \boldsymbol{a}$ are defined in appendix A. Multiplying both sides by the transpose of matrix **M**, equation (4.89) can be written as

$$(\mathbf{M}^{\mathbf{T}} \cdot \mathbf{dI}) = (\mathbf{M}^{\mathbf{T}} \cdot \mathbf{M}) \cdot \mathbf{\Delta} a \,. \tag{4.90}$$

Δa can be calculated by solving the set of linear equations represented in (4.90). Updating the value of a and substituting this new value in equation (4.89), one gets a new value of dI. Subsequently, this process repeats till the displacement coefficient reaches a very small value. However, the convergence of this scheme is critically dependant on the initial guess.

4.3.1.1. Least Square Error for Designing a Dual Element for Selective Excitation of The LP_{21} Mode

Using this technique the calculated coupling efficiency to LP_{21} reaches 94% of the total input power compared to 60% using phase matching only with a wavelength of 633 nm and Gaussian beam of 150 μm waist. Figure (4.12) depicts the two phase elements and the amplitude profile of the field just behind the second phase element and at the input facet of the large core fiber.

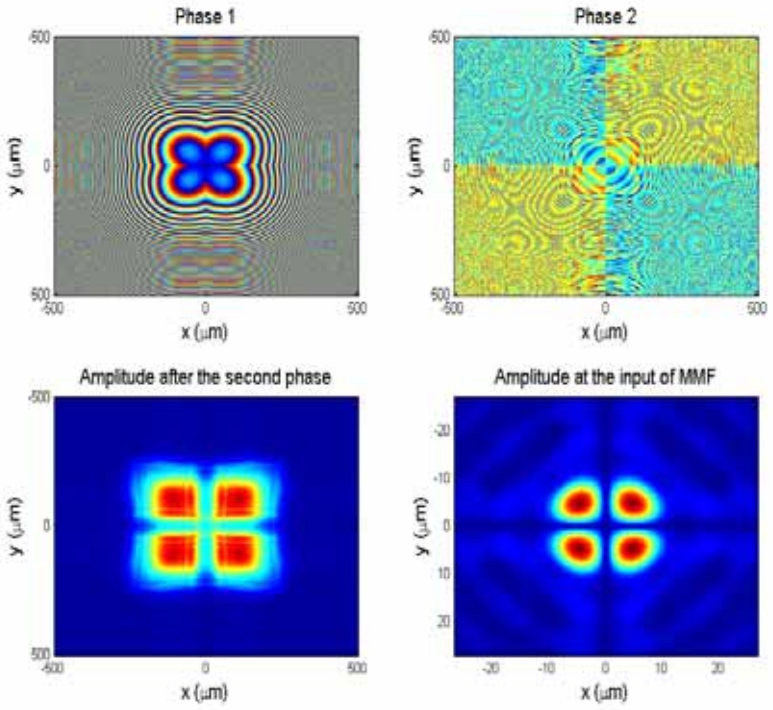

Figure 4. 12: (a) The first phase element, (b) the second phase element (c) phase (c) and intensity (d) distributions of the output field at the input facet of the fiber.

4.3.2. Method of Projection (MOP)

MOP is an iterative technique, where the first phase element is initially set to have a random phase. Applying a two dimensional Fresnel propagator, the complex field distribution is computed at the second phase element, then its intensity is set to the target field intensity. The second phase element is updated by the phase difference between the computed field at the surface of this phase element and the desired phase. Figure (4.13) depicts a schematic diagram of the MOP.

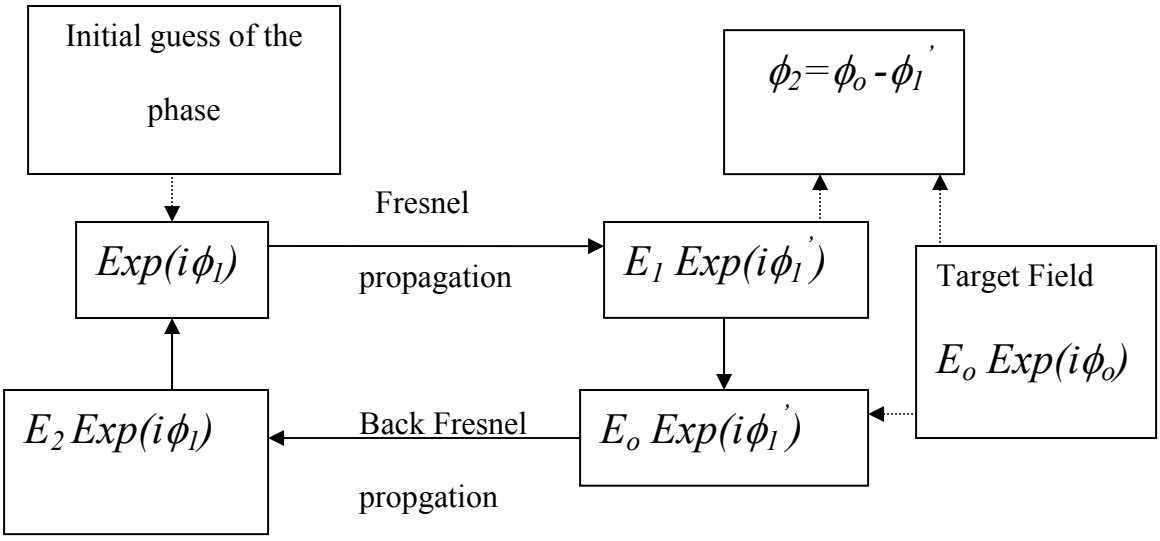

Figure 4. 13: Schematic diagram of MOP.

4.3.2.2. MOP for Designing a Dual Element for Selective Excitation of a High order super mode in seven core fiber

Figures (4.14, (c)) and (4.14, (d)) depict two phase elements designed to match both amplitude and phase of the last fundamental supermode in the seven core as depicted in Figure (3.7).

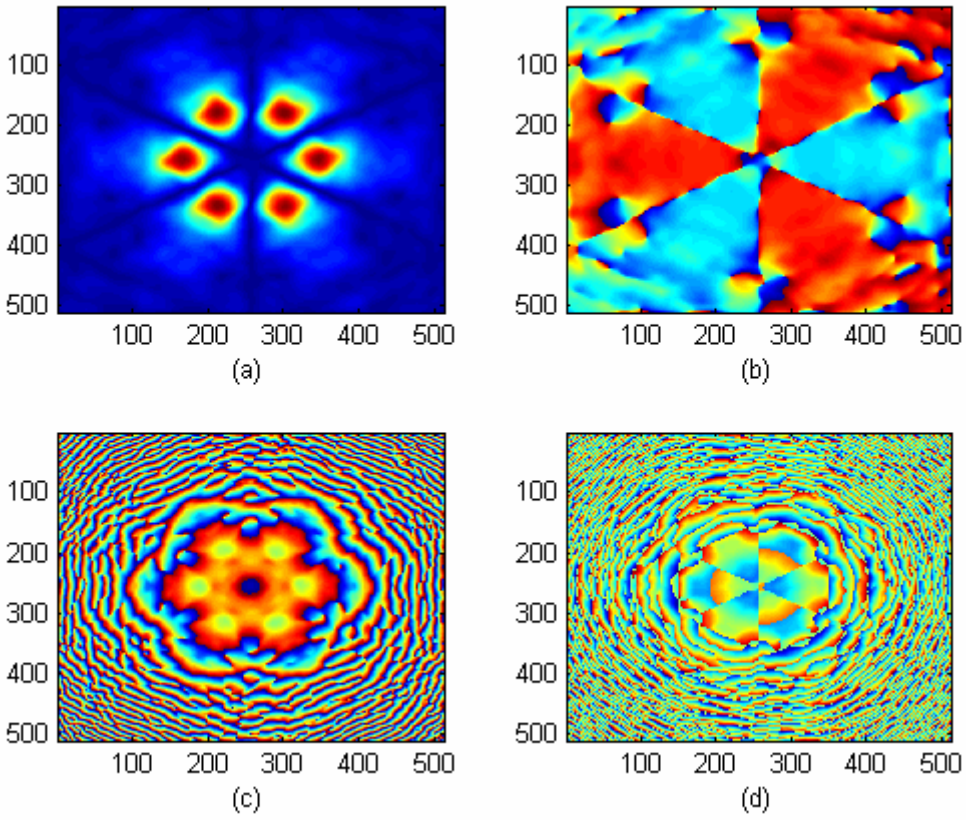

Figure 4. 14: (a) amplitude and (b) phase profiles of the field at the input facet of the seven core fiber when using the dual phase elements (c) and (d).

Using the coupling scheme depicted in Figure (4.10) and considering a 633 nm source, the calculated amplitude and phase profiles of the field at the input facet of the multicore fiber are depicted in figures (4.13, (a) and (b)). Using the overlap integral in (4.27), the estimated maximum coupling efficiency is about 98% when both L and f distances in Figure (4.10) are set to 1 mm.

4.4 Sub-wavelength periodical structure for coupling to hollow waveguide.

In chapter three, we presented first order calculations of the transmission and bending losses inside the cylindrical hollow waveguides based on Fresnel reflections. These calculations showed that the TE_{01} mode suffers the least amount of losses as depicted in figures (3.13) and (3.15). Coupling the input light to this mode, the performance of the light delivery system can be dramatically improved. To selectively excite this mode, matching the phase and amplitude profiles of the TE_{01} mode only will not be sufficient due to the degeneracy between this mode and the TM_{01} mode. Thus, it is desired to design an optical component that converts an incident linearly polarized light into a rotating one similar to that depicted in Figure (3.10, d). In order to design this optical component, we first need to review an important property of birefringent crystals.

For a birefringent crystal, the transmittance of this crystal for an incident linearly polarized light of angle ψ relative to the crystal axis (fast axis) with a phase retardation of π can be written as [44]

$$T(x,y)=\begin{pmatrix}-i\cos(2\psi(x,y))\\-i\sin(2\psi(x,y))\end{pmatrix}. \tag{4.91}$$

Thus, it is possible to obtain the desired output polarization distribution if the axis of the crystal varies in space. Realization of such component is almost impossible using traditional bierefringent crystals. However, artificial birefringent crystals can be fabricated using subwavelength gratings [45].

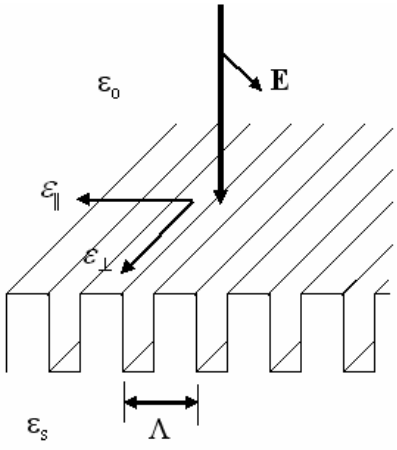

Figure 4. 15: Sub-wavelength grating structure that forms an artificial birefringent crystal.

Figure (4.15) depicts the subwavelength grating structure. In this figure, $\varepsilon_{\parallel}$, and $\varepsilon_{\perp}$ are the parallel and normal effective permittivities of the grating. ε_s and Λ are the substrate permittivity and the grating period. The birefringence of such structure can be calculated

using effective index method [46]. For the configurations shown in Figure (4.11), the calculated permittivities are

$$\varepsilon_{\perp} = \varepsilon_{\perp}^{0}\left(1+\frac{\pi^2}{3}\left(\frac{\Lambda}{\lambda}\right)^2 f^2(1-f)^2\,\frac{(\varepsilon_s-\varepsilon_o)}{\varepsilon_o\varepsilon_{\perp}^{o}}\right), \tag{4.92}$$

and

$$\varepsilon_{\parallel} = \varepsilon_{\parallel}^{0}\left(1+\frac{\pi^2}{3}\left(\frac{\Lambda}{\lambda}\right)^2 f^2(1-f)^2\,\frac{(\varepsilon_s-\varepsilon_o)\varepsilon_{\perp}^{o}}{\varepsilon_o}\left(\frac{\varepsilon_{\parallel}^{o}}{\varepsilon_o\varepsilon_s}\right)\right). \tag{4.93}$$

In equations (4.92) and (4.93)

$$\begin{aligned}\varepsilon_{\perp}^{0} &= f\varepsilon_s+(1-f)\varepsilon_o\\ \frac{1}{\varepsilon_{\parallel}^{0}} &= \frac{f}{\varepsilon_s}+\frac{1-f}{\varepsilon_o}\end{aligned}\quad, \tag{4.94}$$

where f is the in plane filling ratio. Using the effective refractive index calculations mentioned above, the required depth of the grating to have π retardation is

$$d = \frac{\lambda}{2(\sqrt{\varepsilon_{\perp}}-\sqrt{\varepsilon_{\parallel}})}. \tag{4.95}$$

4.4.1. Polarization converter element for coupling to TE_{01} mode.

For fused silica substrate, operation wavelength λ=0.98 μm, period of λ/2 and filling factor of 0.5, the calculated depth is about 6.84 μm. In a similar way, the calculated depth for the working wavelength of 1.55μm is 11.06 μm. Figure (4.16) depicts the proposed sub-wavelength structure.

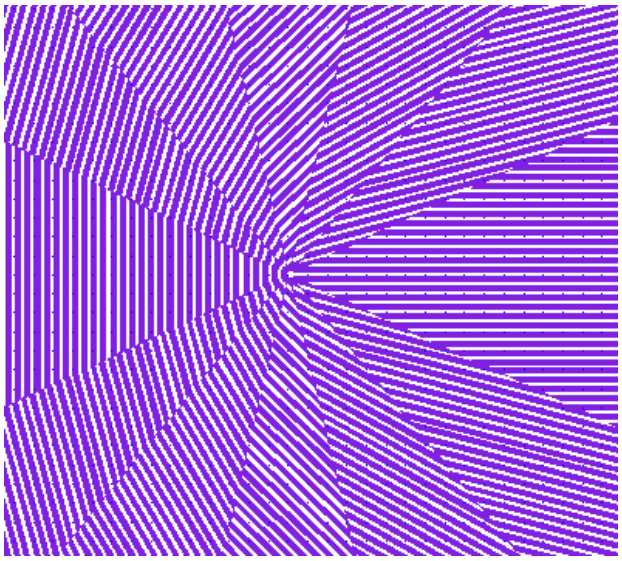

Figure 4. 16: The proposed design of polarization converter element to couple the light at the input of the hollow waveguide to the TE_{01} mode.

In this design, the working space is divided into 12 sectors. Each section represents a sub-wavelength grating with grating vector rotated by π/6 relative to the next sector. Thus each sector rotates the incident linearly polarization by 2ψ, where ψ is the

angle of polarization of the incident light relative to the grating vector. For an incident y polarized light the output polarization status will result in the field distribution and polarization status depicted in Figure (4.17) below. This field, to great extend, matches the desired TE_{01} mode. On the other hand, for an incident x polarized light the output field will be similar to that of TM_{01} mode.

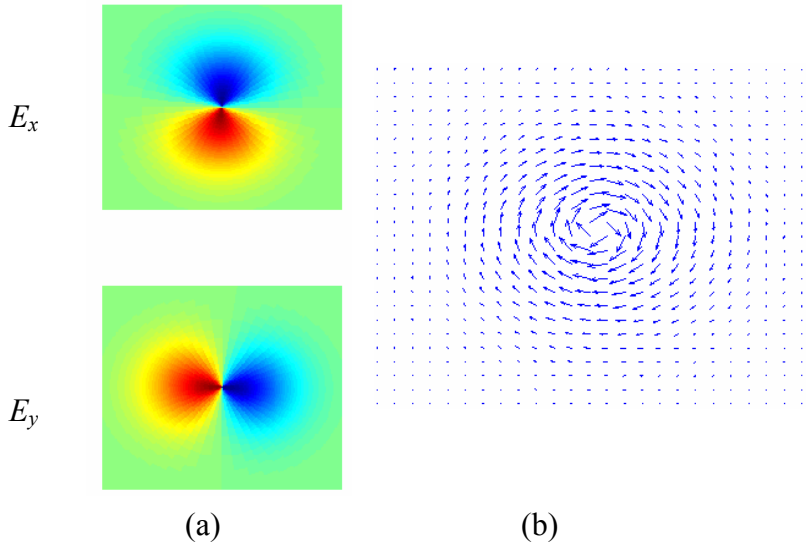

Figure 4. 17: Calculated (a) Field and (b) polarization distributions of the output of the polarization converter element.

This section presented the design of novel optical elements that couple the light to the desired guided modes in different specialty waveguides. However, fabricating some of these elements is challenging. The next section summarizes several fabrication techniques and procedures to realize these elements.

CHAPTER FIVE: FABRICATION TECHNIQUES

Lithography is a key process technology for fabricating micro-optical elements and is used to copy a master pattern into solid material such as silicon, glass or GaAs. This process has two major steps. First, a pattern is written into a resist material by exposing it to light (photolithography) or an electron beam (e-beam lithography) and developing in order to remove resist in selected areas. Second, the pattern is transfer etched into a substrate material using an etching technique. The substrate is etched where it is not protected by the resist material. Photolithography is most widely used.

In the next section, photolithography using a contact aligner and a stepper system is introduced. Both require a mask to control which portions of the resist are exposed, and hence the pattern. The photomask is typically an optically flat and transparent glass or quartz with a metal absorber pattern (e.g. 80 nm of chromium). [47] E-beam lithography (EBL) does not require a mask because the pattern is written by steering a narrow beam of electrons to write the pattern into the resist. In section three, fabrication of the polarization converter element using EBL is discussed. Section four introduces the use of the focused ion beam (FIB) system for integration of micro optical elements into real devices. The main advantage of FIB over lithography is that devices can be made in a single process step without a mask.

5.1. Photolithography

Figure (5.1) shows two major photolithography systems: contact aligners and steppers. In contact aligner systems, the photo-mask is usually in direct contact with the photoresist-coated surface during exposure as depicted in Fig. 5.1.(a). Ultraviolet light passes through a mask where it is selectively blocked by the metalized patterns. In this manner, the photoresist is exposed with the same pattern as the mask.

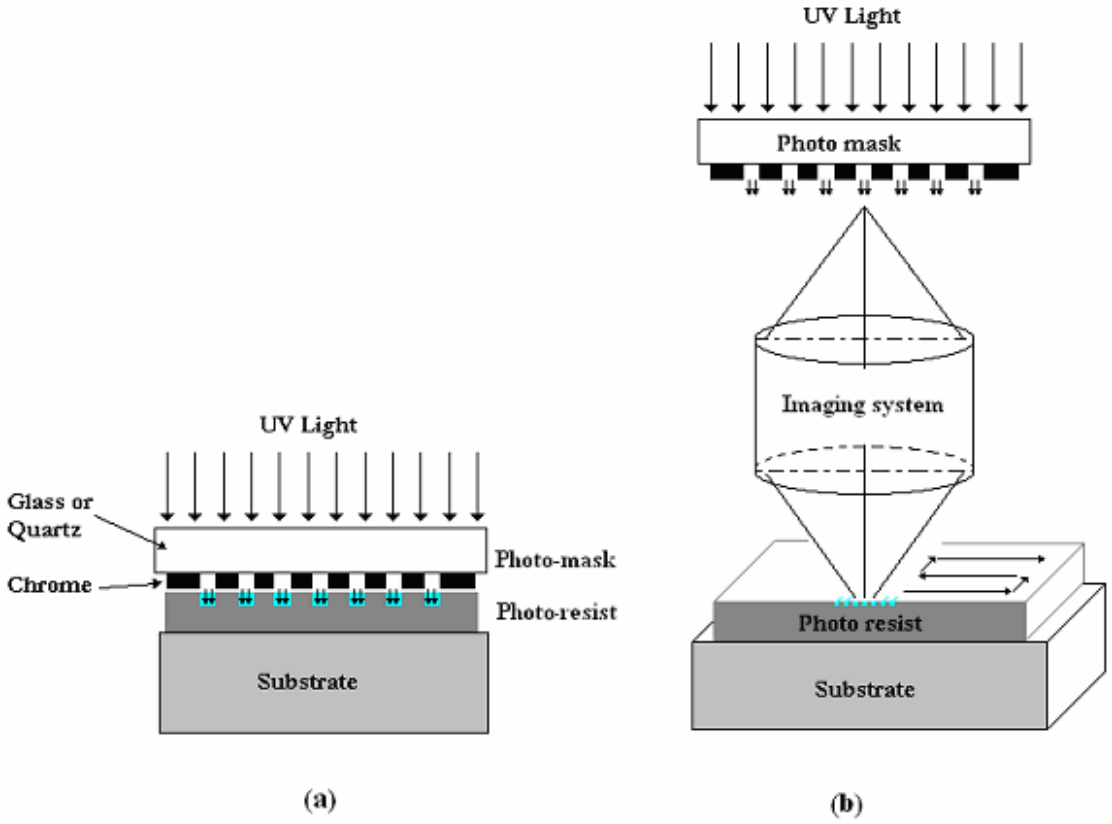

Figure 5. 1: The two major photolithography systems: (a) Contact aligners and (b)

steppers.

For the research described in this paper, the pattern on the photo-mask was generated using EBL because it could produce higher resolution patterns than photolithography alone. The transparent pattern on the mask was transferred to the photoresist coated on the wafer surface and then to the substrate using etching techniques. This procedure results in a 1:1 imaging of the entire mask onto the wafer.

Contact masks degrade fast through wear. Defects resulting from hard contact on both the photoresist and the wafer make this method unsuitable for very large scale integration manufacturing. However, this method is still commonly used in research and development as well as mask making [47]. A more robust method uses an optical stepper where the photo-mask does not contact the substrate, but is imaged onto the photoresist from some distance away.

Basically, the optical stepper is an imaging system where the photo-mask is in an object plane and the photo-resist layer on the wafer is in the image plane [48-49]. The scale of the pattern is often reduced by the imaging system. A 5:1 reduction is common. The photo-mask is illuminated by a UV source through condenser optics during exposure. This light incident on the photo-mask is well collimated and the effective source of UV light is imaged onto the pupil plane inside the stepper. Figure 5.1(b) shows a conceptual diagram of a typical optical stepper system. With a deep UV light source, resolution of 1 μm can be achieved, depth of focus of ±6 μm is possible, and an overlay accuracy of ±0.25 μm has been realized [1].

5.1.2. Example of Photolithography: Fabrication of Single phase elements

Figure (15) depicts Zygo profiles of the two phase elements presented in section 4.1. These elements were fabricated in Shiply PR1805 photoresist using a stepper system. The refractive index of the photoresist is 1.6406 at the working wavelength of 633 nm. To achieve a π phase shift, the step height was set to 494 nm.

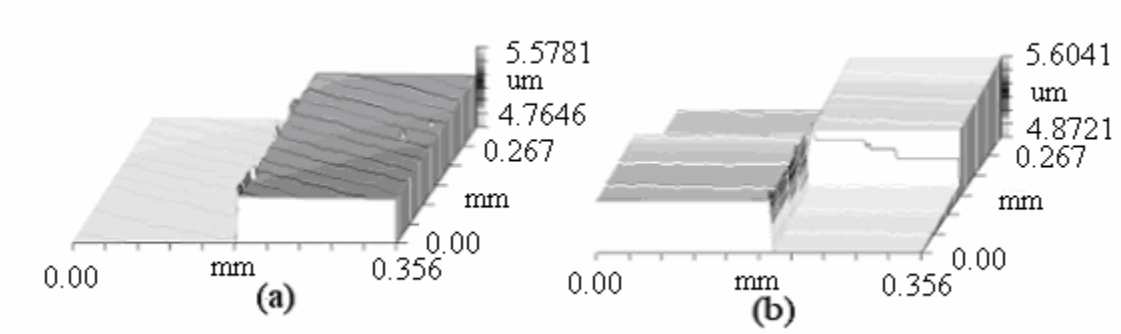

Figure 5. 2: (a) and (b) Zygo images of the first and second phase elements for coupling to LP_{11} and LP_{21} modes respectively, fabricated in PR1805 photoresist

5.2. Electron Beam Lithography

EBL is a high resolution pattering technique in which high-energy electrons (10 to 100 KeV) are focused into a narrow beam that exposes electron sensitive resist. Unlike photolithography, EBL does not limit feature resolution by diffraction because the

quantum mechanical wavelength of the high energy electron beam is exceedingly small [47]. On the other hand, resolution of the EBL system is affected by scattering of electrons from the resist and substrate. Back scattering of electrons exposes the resist over an area slightly greater than the spot size. This phenomena manifests itself in small variations in the geometry of exposed structures. The effect is more pronounced fy small structures

5.2.1. Introduction to E-Beam Lithography

EBL is a high-resolution and maskless pattering technique. Electrons emitted from a source are focused onto a substrate through an imaging column. The focused beam is scanned over the substrate using deflectors as depicted in Fig. 5.3. A computer controls the beam blanker, the deflector, and the moving stage according to received mask data. Total writing time depends on total exposed area and required dose to fully expose the e-beam resist. At the end of the writing process, a pattern is written into the e-beam resist. E-beam resists are produced for direct writing applications. Bombardment of polymers by electrons causes bond breaking. A subsequent chemical developing process is required. For positive resists, exposes areas are removed during developing. For negative resists, exposed resist remains after developing. In either case, the remaining resist serves as a mask during a subsequent etching process. Either wet or dry etching can be used to transfer etch into the substrate.

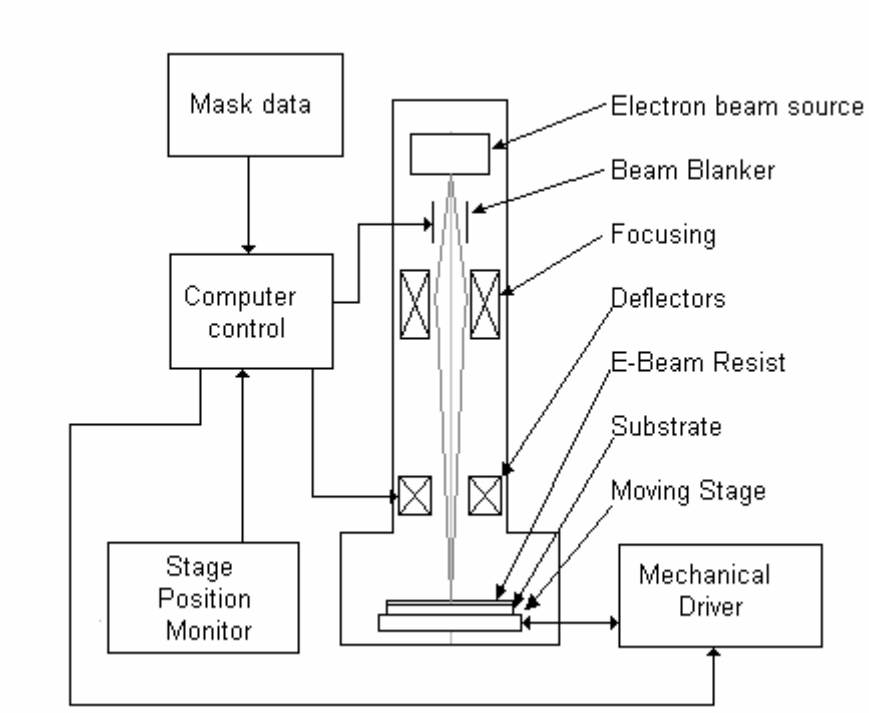

Figure 5. 3: Schematic diagram of e-beam system.

5.2.2. Fabrication of Polarization Converter Element

As presented in section 4.2, the polarization converter element is made of sub-wavelength gratings with a 0.775 μm period. Each grating is oriented such that the grating vector is rotated by π/6 relative the previous one. This structure has features as small as 375 nm with a depth of 11 μm in order to achieve π phase retardation when using fused silica as a substrate. In contrast, only 996 nm depth is required when using GaAs.

In the next sections, different fabrication procedures are used to realize this structure in both fused silica and GaAs. First, e-beam resist (ZERP 520) was used as a mask for etching into a GaAs substrate where an etching selectivity more than 2:1 was achieved. This selectivity is sufficient for GaAs, but not for fused silica that requires up to 22:1. For fused silica, a hard (metal) mask must be used.. The hard mask is fabricated using a lift off process and a bi-layer PMMA resist. For both techniques, the pattern must be properly transferred to the resist. This requires selecting an accurate dose while writing the pattern. Quality of the hard mask, and eventually the etched pattern, is determined by the surface condition in the developed regions and the amount of resist left after developing.

The next section discusses pattern transfer writing in ZEP520 resist using EBL.

5.2.2.1. Writing the pattern into the e-beam resist

The desired pattern was the first generated using our GDS master software. The pattern was fractured using a Linux based commercial software, CATS, and written to the resist using the Lieca EBPG 5000+ E-Beam at 50 KeV. Different e-beam resists have different polarity, sensitivity, resolution, and etch resistance. PMMA and ZEP520 are examples of positive e-beam resists. Although both resists have high resolution, ZEP520 has higher sensitivity and higher dry etch resistance. This reduces the e-beam writing time when using ZEP520 compared to PMMA. In addition, ZEP520 holds for a longer

time when etching chrome. Finally, ZEP520 resist can produce an under-cut profile similar to PMMA as depicted in Fig. 5.5. This profile is favorable for the lift-off process. In this work, ZEP520 was used as a mask for etching in GaAs and to generate a hard mask in chrome.

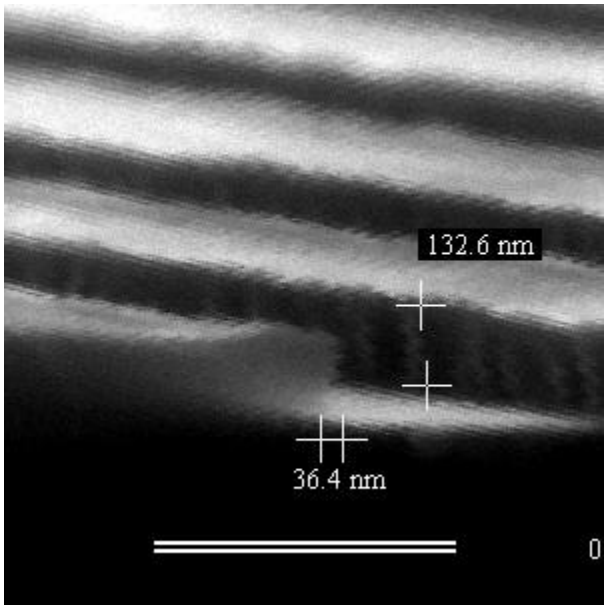

Figure 5. 4: ZEP520 resist profile.

Using ZEP520, proper writing dose is required to generate a pattern with the required dimensions. High doses will result in washed out patterns, while low doses will create under exposed patterns. In addition, the dose is a function of the feature size. To

determine the proper dose, variable period gratings were fabricated with a 50:50 duty cycle. The periods varied from 200 nm to 3.95 μm as shown in Fig. 5.5(a).

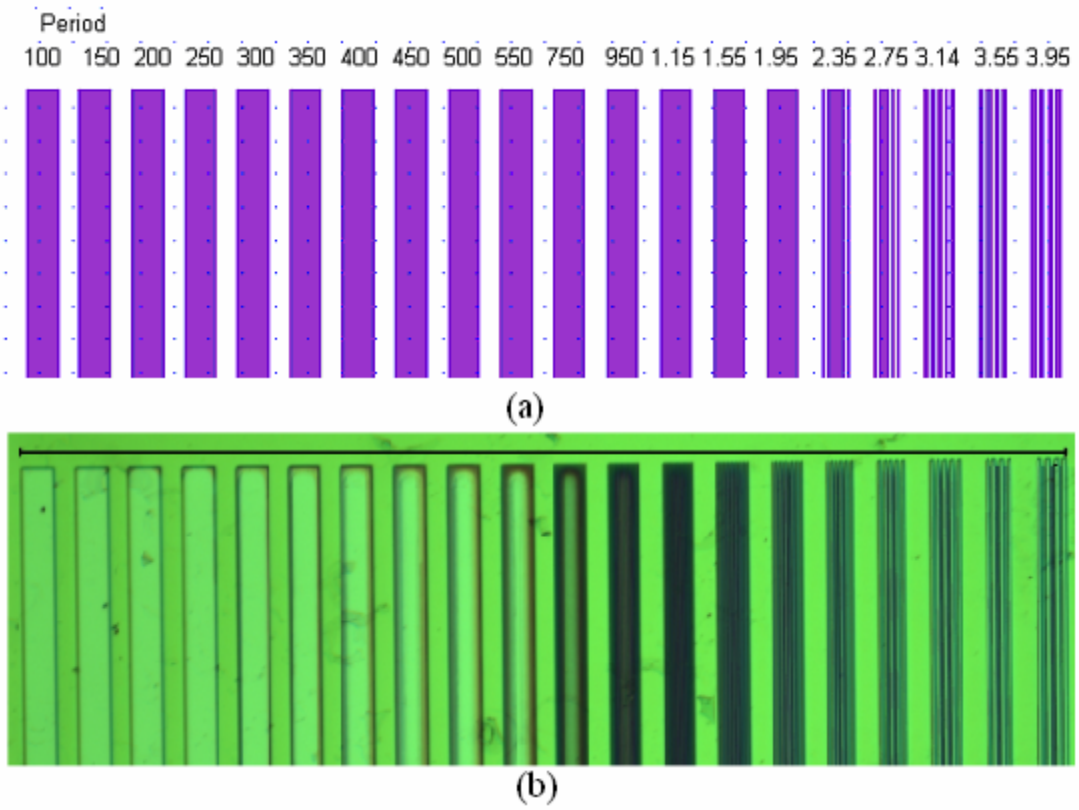

Figure 5. 5: (a) the GDS pattern of gratings of varying periods (b) the pattern written in the e-beam resist.

Using this pattern, a dose matrix was written in ZEP 520 e-beam resist with a dose varying from 50 μC/cm^2 to 300 μC/cm^2. The resist was spun at 1800 rpm on a four inch fused silica wafer coated with 300 nm of chrome. The spun resist layer was 500 nm thick. After writing the pattern, the wafer is developed for 90 seconds using ZEP-D

developer. The wafer was rinsed in isopropanol for 20 seconds immediately after developing. Figure 5.5(b) shows an optical microscope image of the pattern after developing. This pattern was written using a dose of 90 μC/cm^2. Observing the quality of the written patterns under the optical microscope, the dose map in Fig. 5.6 was generated

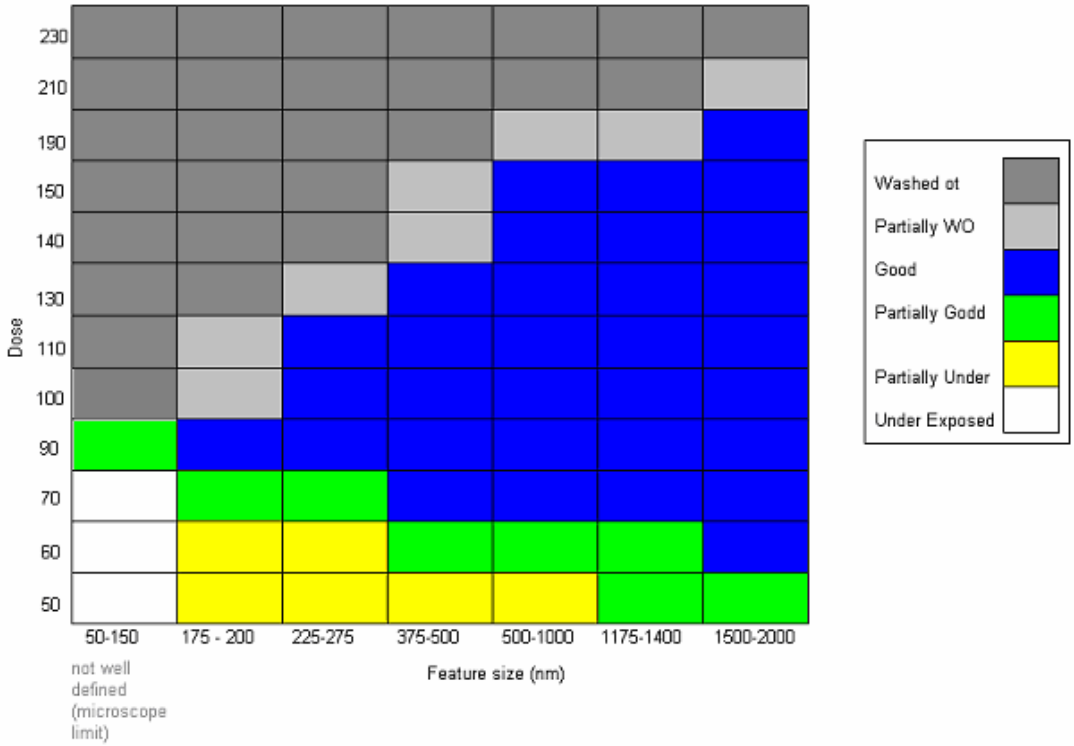

Figure 5. 6: Map of pattern quality in terms of dose values and feature size.

Figure 5.6 shows a 90 μC/cm^2 dose is optimum for features as small as 200 nm. Smaller features can be written with a dose between 70 μC/cm^2 and 90 μC/cm^2. For the

patterns written at 90 μC/cm^2, SEM images were taken after sputtering a 200 angstrom thick film of gold-palladium on the developed resist.

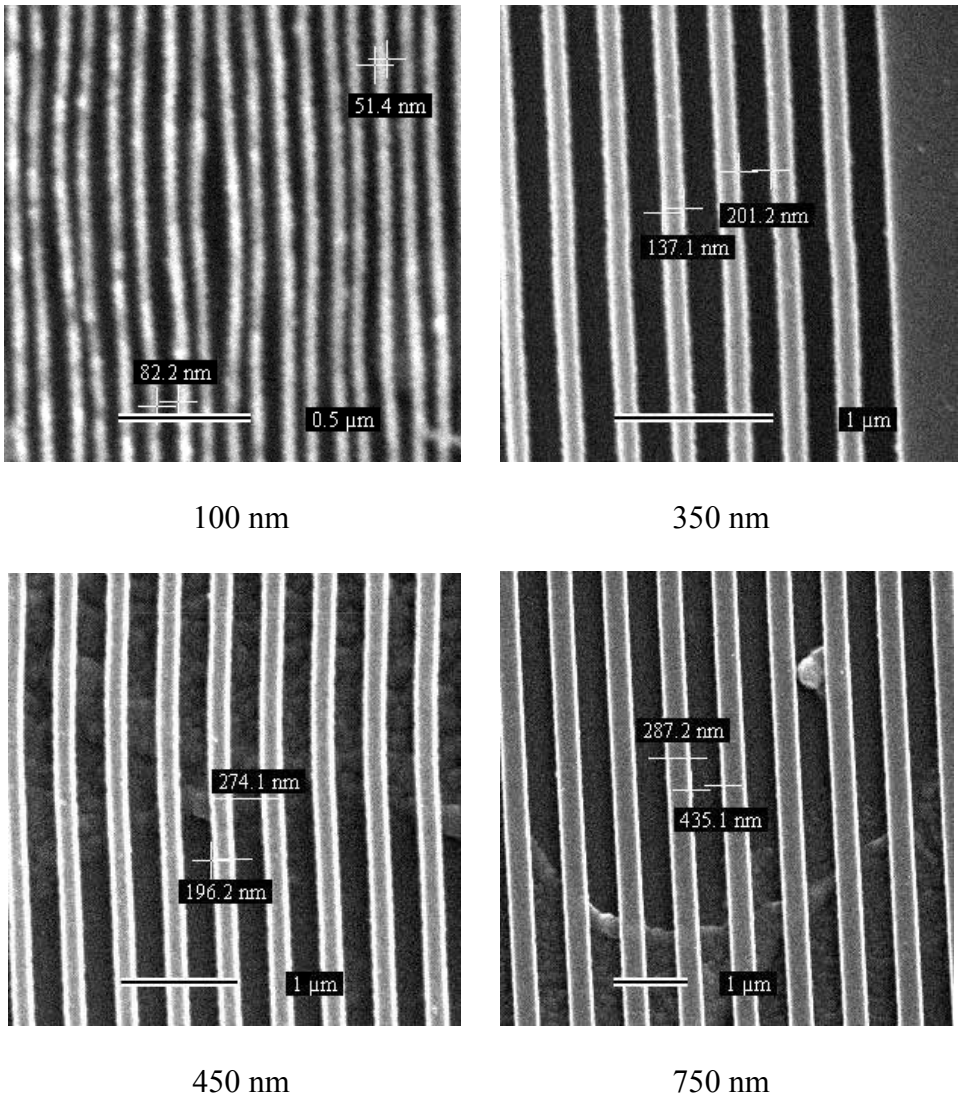

100 nm 350 nm

450 nm 750 nm

Figure 5. 7: SEM images of the varying period gratings using 90 μC/cm^2 after developing and coating with 200 angstrom layer of AuPd.

Figure 5.7 depicts four SEM images of different grating periods, 100nm, 350 nm, 450 nm and 750 nm. For the 100 nm period patterns, the irregularities of the lines are imaging artifacts due to charging of the substrate. In this figure, resist residue remains in the developed areas and may degrade the quality of the hard mask and hence the final etched pattern. The residue can be removed by oxygen plasma etching. In this process we used 40 sccm of oxygen with an ICP power of 400 W and RIE power of 40 W. The measured etch rate of ZEP520 was 10 nm/sec. Thus, five seconds of oxygen plasma etching removed 50 nm of resist.

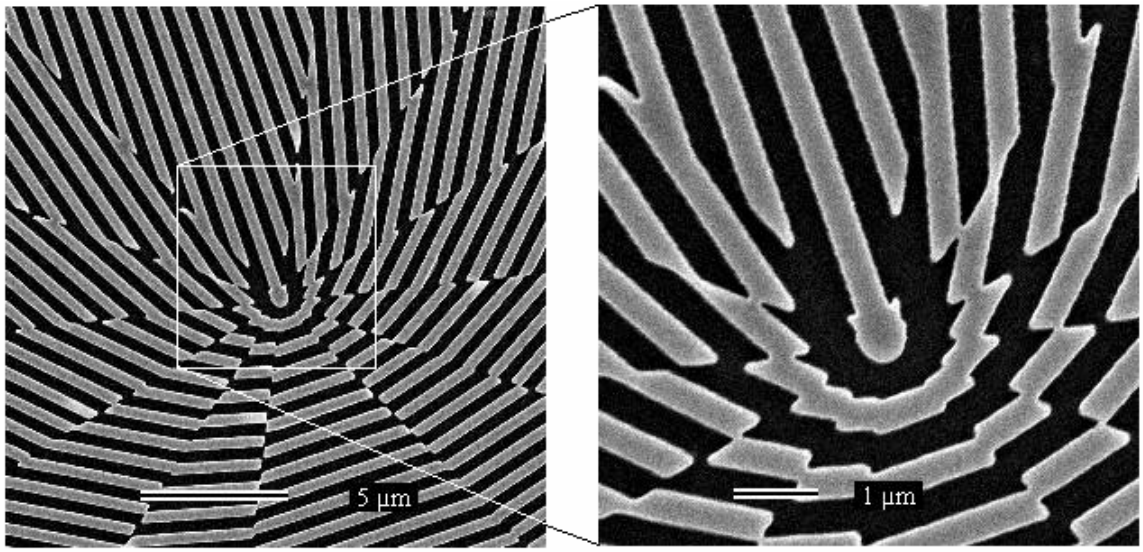

Figure 5. 8: The polarization converter pattern transferred to the ZEP520 e-beam resist.

As mentioned in chapter four, the polarization converter element consists of 12

sectors of subwavelength gratings; each rotated by $\pi/6$ relative to the next sector. The gratings were designed for an operation wavelength of 1.55 μm. Each grating has a period of $\lambda/2$ and filling factor of 0.5. Thus, the minimum feature of this structure is 375 nm. From the e-beam resist analysis depicted in Fig. 5.6, the proper dose to write this structure was 90 $\mu C/cm^2$. Using this dose, Fig. 5.8 shows an SEM image of the pattern generated in ZEP 520 after developing, plasma etching for 5 seconds, and coating with a thin layer of chrome to prevent the charging when using the SEM. This figure shows the pattern was properly transferred in the resist. The next step was to transfer etch this pattern into the substrate material.

5.2.2.5. Transfer Etching into Gallium Arsenide

First, ZEP 520 was spin-coated directly onto a GaAs wafer. Second, a pattern of gratings was written into the resist. The gratings had a 50% duty cycle with periods varying from 400 nm to 1600 nm in 200 nm increments. Third, the resist was developed using ZEP-RD for 90 seconds. Using the resist as a mask, the pattern was transfer etched in the GaAs substrate using a BCl_3/Ar plasma etch for two minutes. In this process, 20 sccm of BCl_3, 10 sccm of Ar, and 5 sccm of N_2 was used at a pressure of 10 mT. The RIE power was 60 W and the ICP power was 500 W. The profiles of the etched pattern were imaged using a SEM and are depicted in Fig. 5.9. Smaller period gratings had smaller depth than the larger period gratings (279 nm for 600 nm period grating compared to

799 nm at 1400 nm period grating as shown in Fig. 5.9(a) and 5.9(d) respectively.) This was due to a micro loading effect. Resist at the smaller period gratings etched faster than the larger period gratings. The eroded patterns in Fig. 5.9 were caused by resist being completely etched and no longer masking the GaAs. It is therefore necessary to increase etching selectivity and reduce the resist etch rate. The first was achieved through reducing RIE power, increasing ICP power, and increasing pressure. The resist etching rate was decreased by reducing the flow rate of the BCl_3 gas. Table 5.1 shows the different recipes used, the resulting etch rates, and etch selectivities.

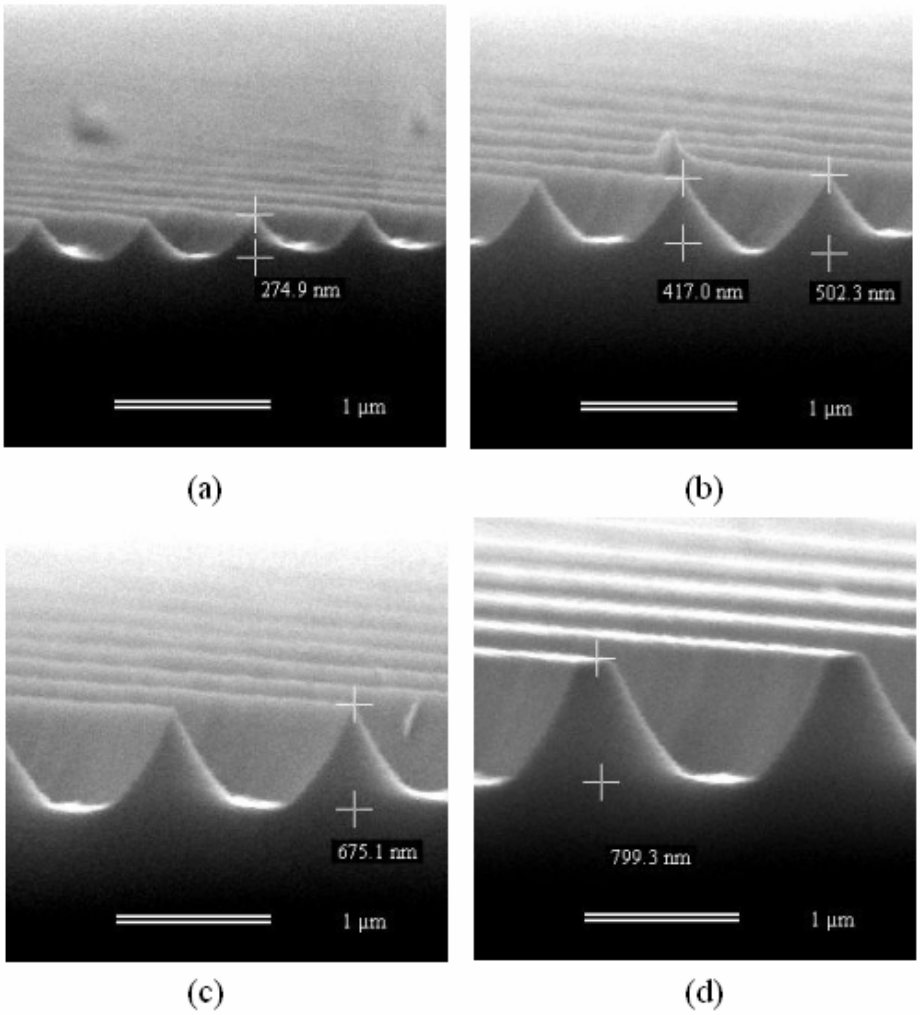

Figure 5. 9: Cross section SEM images of gratings with different periods etched into GaAs using 500 nm of ZEP520 as a mask and $BCl_3/Ar/N_2$ plasma for two minutes. Grating periods are (a) 600 nm, (b) 800 nm, (c) 1000 nm, and (d) 1400 nm.

Table 5. 1

GaAs dry etching process when using ZEP 520 as a mask.

Process	**BCL_3 (sccm)**	**Ar (sccm)**	**Pressure (mT)**	**RIE (W)**	**ICP (W)**	**Etch rate (nm/min)**	**Selectivity**
1	5	5	10	80	500	115	(1:1.15)
2	5	5	10	50	500	122	(1:1)
3	5	2	10	50	500	140	(1:1.4)
4	5	2	10	40	800	140	(1:1.67)
5	5	2	15	40	800	170	(1:2)

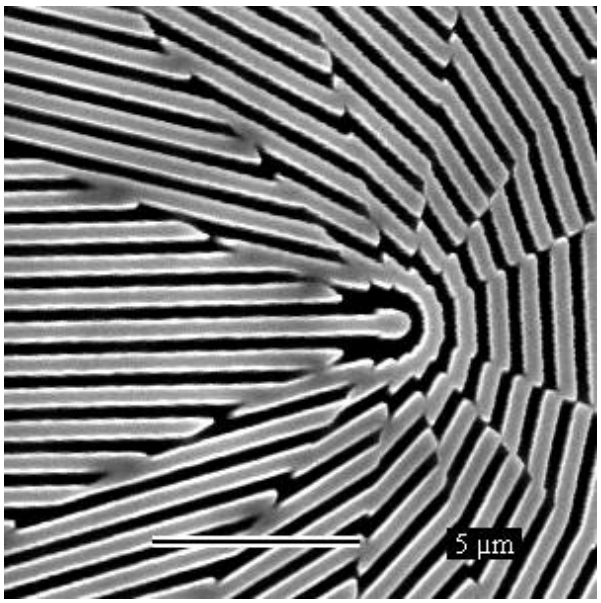

Figure 5. 10: SEM image of the pattern transfer etched in GaAs using ZEP 520 as a mask.

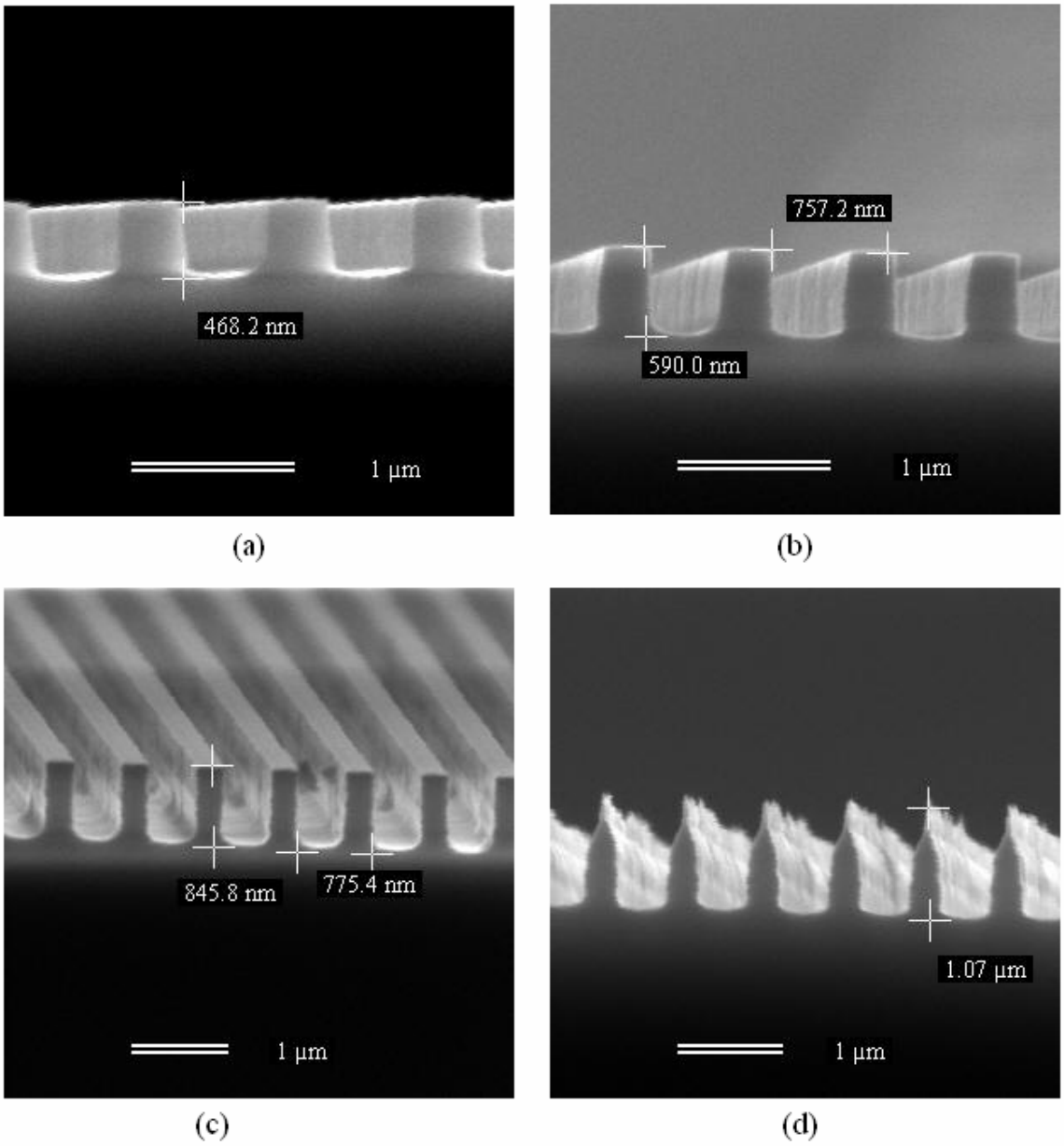

Figure 5. 11: SEM cross sectional image of the polarization converter pattern transfer etched in the GaAs substrate using (a) process 1 for 4 minutes, (b) process 3 for 5 minutes, (c) process 5 for 6 minutes, and (d) process 4 for 7 minutes.

Table 5.1 shows dry etching recipies using BCl_3/Ar plasma. It is clear from this Table, increasing the ICP from 500 W to 800 W improved the resist:GaAs etch selectivity from 1:1 to 1:2. Increasing the pressure from 10 mT to 15 mT, however, increases etch rate from 140 nm/min to 170 nm/min. Figure 5.10 shows a top view image of the polarization converter element transfer etched into a GaAs substrate taken by SEM. As can be seen, the pattern was properly transferred into the substrate. The profile of this element can be inspected by cleaving through it. Figure 5.11 shows profiles of some elements fabricated using different process from Table 5.1. The micro loading effect is apparent in Fig. 5.11(d), when using the process 5 for seven minutes.

5.3. Focused ion beam system for prototyping micro-optical elements

A FIB is often used in sample preparation for characterization measurements using a Transmission Electron Microscope (TEM) or Scanning Transmission Electron Microscope (STEM). Others have demonstrated the use of a FIB for micro/nano fabrication on flat surfaces of optical components such as gratings, photonic crystals, and micro lenses [50-54]. The main limitation of prototyping and fabrication with FIB is cost for mass production when compared to the available lithography tools such as EBL and photolithography. Moreover, FIB does not improve the resolution or surface quality over these techniques. Fabrication time and complexity become important issues as the device size increases. On the other hand, the FIB is a competent tool for rapid prototyping of

new devices, since it is a maskless fabrication technique and can be used on a single chip with small field sizes [50].

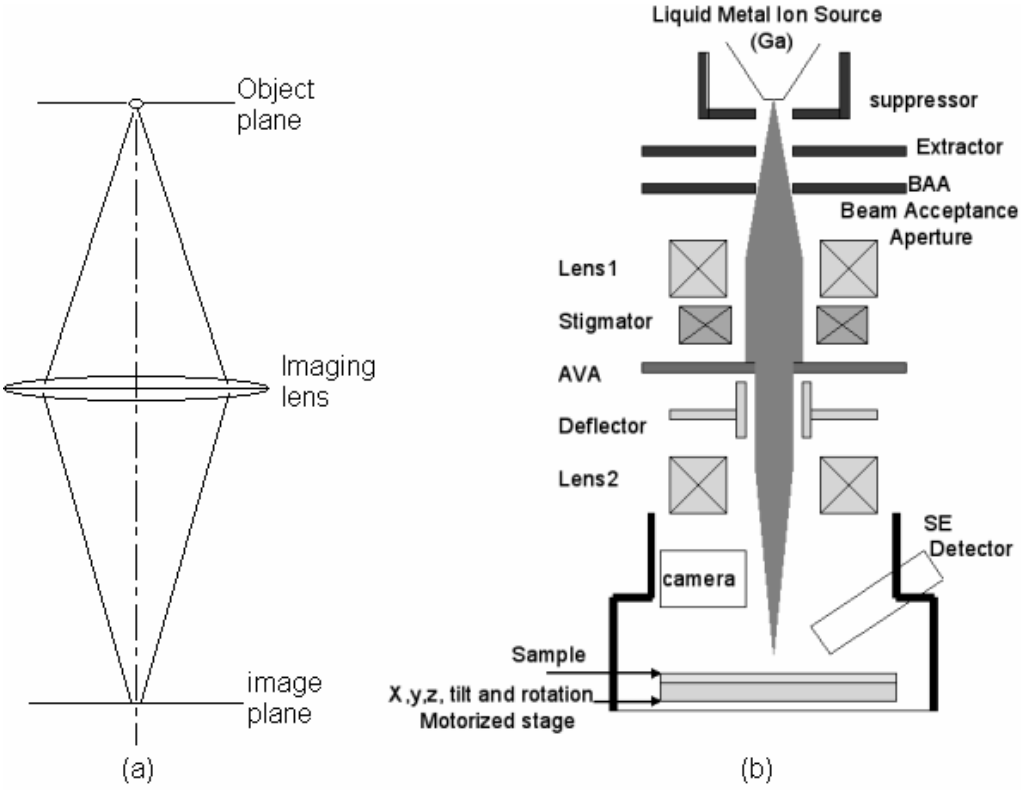

Figure 5. 12: (a) Representation of the FIB as an imaging system. (b) Schematic picture of a typical FIB system.

A FIB workstation takes charged particles from a source, focuses them into a beam through electrostatic lenses, and scans across small areas of the sample using deflection plates or scan coils. The charged particles (ions) are composed of a liquid

metal ion source (LMIS), Ga^+, where ions are produced through field evaporation by applying a high voltage on the emitter.

The emitter is a highly sharpened metallic needle. As liquid metal flows through the emitter, an electric field maintains the conical shape of the liquid. The conical shape provides a small end radius, typically in the range of 5 nm [55].

5.3.1. Focused Ion Beam as an imaging system

Focused ion beam is a point to point imaging system, where the shape and the size of the ion source at the object plane is transferred to the image plane as illustrated in Fig. 5.12(a). To transfer the image of the source to the substrate, an electrostatic lens is used. In comparison to an optical lens that consists of a transparent material of refractive index greater than unity, the electrostatic lens consists of an electrostatic field generated by a set of electrodes and insulators separating them. It is very difficult to calculate the refractive index of the electrostatic lens as the geometry of the electrostatic field depends on the potential distribution generated by the electrodes. Instead, equations of motion of ions passing through the lens can be written using the paraxial approximation as follows [56].

$$m\ddot{r} = \frac{qr\phi''}{2} \tag{5.1}$$

$$m\ddot{z} = -q\phi' + \frac{qr^2\phi''}{4}, \tag{5.2}$$

where q is ion charge, ϕ is potential, m is ion mass, ϕ' and ϕ'' are the first and second derivatives of the potential with respect to *r*. Equation (1) shows the second-order derivative of the radial position, *r*, is linearly proportional to *r*. This means ions located farther from the axis accelerate faster towards that axis. Thus the focal point is independent of *r*, which implies lens action. As in any imaging system, resolution is very important. In the next part we will briefly discuss spot size limitations of the FIB system.

5.3.2. Spot size limitation

The focused beam size of any FIB system depends on the presence of imaging aberrations and the Coulomb effects in the beam. Unfortunately, electrostatic lenses suffer from many aberrations known to optics plus more due to the anisotropic properties of the lens. As an LMIS is essentially a point source, the principal aberrations of interest are spherical and chromatic aberrations. It was assumed the current distribution was Gaussian at the source plane and that the source was well aligned on axis. Aberrations that depend on r can then be neglected. Given the source diameter d_g, the spot diameter at the image plane is

$$d = \sqrt{d_g^2 + d_c^2 + d_s^2}\ . \tag{5.3}$$

In this equation d_s and d_c are the spherical and chromatic aberration disks diameters. Equation (5.3) can be written in terms of the ion energy U, half width full modulation of the ion energy distribution ΔU, aperture angle α, and spherical and chromatic aberration coefficients C_{so} and C_{co}, as follows [56].

$$d = \sqrt{d_g^2 + \left(C_{co}\alpha \frac{\Delta U}{U} \right)^2 + \left(\tfrac{1}{2} C_{so}\alpha^3 \right)^2} \tag{5.4}$$

Equation (5.4) shows smaller spot size at the image plane can be achieved using smaller aperture angle, α. Reducing aperture angle, however, means reducing aperture size. This eventually reduces beam current at the sample/image plane. From the above arguments, a tradeoff is required to achieve the desired spot size and current value at the sample according to each specific application of the FIB system. Table 5.2 shows some typical values of d_{co} and d_{so} for a LMIS focusing column for different aperture angles with parameters $C_{so}=10^3$ cm, $C_{co}=10$ cm, $\Delta U = 5$ eV, $U = 10^4$ eV, and d_g=50nm [56].

The above text discussed the FIB as a system that images the source to the substrate. Limitations of spot size (or magnification of the source) was also discussed. It is also important to highlight some theory on the interaction between the ion beam and the solid

substrate. The following section discusses the basics of ion-solid interaction and its importance for micro-fabrication.

Table 5. 2

Typical values for the spherical and chromatic aberrations disks diameters for a LMIS focusing column with the parameters mentioned in the above paragraph.

α (mrad)	d_s (μm)	d_c (μm)
0.5	6.3×10^{-4}	2.5×10^{-2}
1.0	5.0×10^{-3}	5.0×10^{-2}
2.0	4.0×10^{-2}	0.1
3.0	1.4×10^{-1}	0.15
4.0	0.32	0.2
5.0	0.63	0.25

4.3.3. Interaction of ions with the substrate

Ion-solid interaction is substantially different than electron-solid interaction due to

intrinsically large difference in mass of the impinging particles. There are two basic classes of interaction between ions and solids. These are elastic and inelastic interactions. Elastic interactions cause defects through sputtering from displaced atoms in the lattice. Inelastic interactions produce other forms of energy such as secondary emitted electrons or x-rays.

With elastic interactions, impinging ions with a specific energy can sputter the material atoms, on a very small scale, and permanently change the surface chemistry of the substrate. By controlling the locations and depth of material to be removed, extremely small patterns can be directly milled in the substrate. The number of target atoms sputtered per primary ion is a very important quantity called the sputtering yield. This quantity strongly depends on the substrate material and ion source. The total sputtered volume of the material per unit time per unit incident beam current (in nA) is called milling rate. For a structure of certain volume, the total milling time can be estimated as

$$total\ time = \frac{Volume\ (\mu m^3)}{milling\ rate\ (\mu m^3 s^{-1} nA^{-1}) \times Beam\ current\ (nA)} \tag{5.5}$$

Table 5.3 shows typical values of milling (sputtering) rate and total time for three substrate types: Si, SiO_2, and GaAs considering Ga^+ LMIS with a potential of 30 KeV, beam current of 1000 pA, and a total milled volume of 1 μm^3 [57].

Table 5. 3

Typical values of the sputtering rate and total milling time for different substrates with the ion beam parameters mentioned above.

Substrate	Sputtering rate	Milling time (sec)
Si	0.22	4.5
SiO_2	0.23	4.3
GaAs	0.69	1.45

The inelastic process, specifically the production of secondary electrons, is very useful for constructing an image of the milled structure. This can be accomplished by collecting the secondary emitted electrons while scanning across the sample.

The inelastic process, specifically the production of secondary electrons, is very useful for constructing an image of the milled structure. This can be accomplished by collecting the secondary emitted electrons while scanning across the sample.

4.3.4. FIB as a tool for micro-fabrication

Figure 5.12(b) shows a schematic diagram of a typical FIB system. The three main components of the system are the source (object), the imaging optics, and the substrate

chamber (image plane). High voltage is applied to the emitter – a voltage difference between the suppressor and extractor to extract ions out of the source (typically 30 kV). The beam acceptance aperture (BAA) controls beam current in the column, and therefore the amplitude of system aberrations in Eq. (5.4). The first lens collimates the beam and the second lens serves as the imaging lens. The automatic variable aperture (AVA) can be set for the desired current to the sample. The sample holder is placed on a moving stage that can be automated.

With the appropriate background, FIB for micro-fabrication can now be discussed. First, feature size limits beam current because the imaged spot size is proportional to acceptance aperture size as in Equation (5.4). Reducing beam current will reduce system aberrations, but will require a longer milling time as quantified in Equation (5.5). Given beam current and total milling volume, total milling time can be estimated using Equation (5.5). Patterns can be defined in two formats: basic geometric elements or stream of points. For the first format, patterns are described as a combination of basic geometric elements. Each element is milled to a specific width such that the final pattern is achieved. To mill one element, the beam deflector controls the trajectory of the ion beam to fill the whole area of this pattern

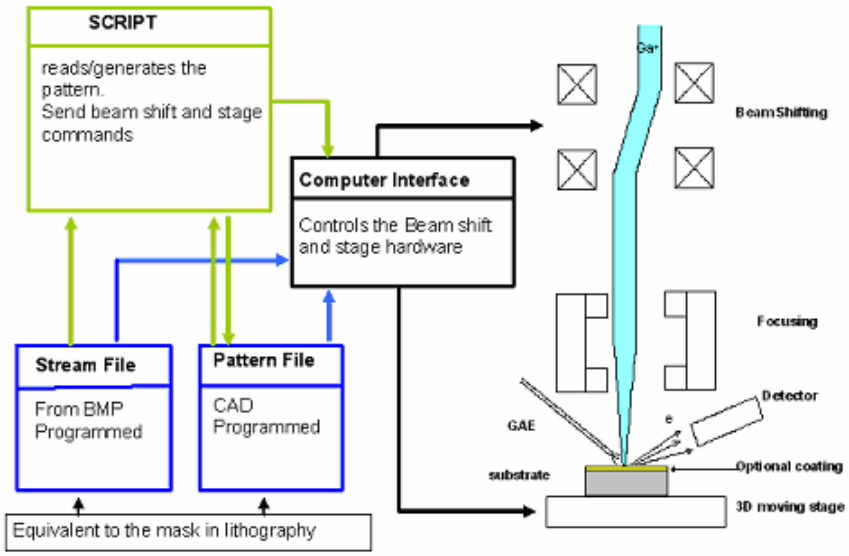

Figure 5. 13: FIB system as a tool for micro fabrication

In the second format, the pattern is defined as a stream of points that must each be milled for a specific time. In this format, the ion beam is raster scanned over the allocated spots in the pattern. Once the pattern is generated, the location of the pattern to be milled is manually selected and aligned. This method is convenient for applications that do not require high precision. To automate the milling process, a script can be written that contains a flow of commands to be executed until the final pattern is milled. Figure 5.13 shows a schematic diagram of the FIB as a tool for micro fabrication.

This section discussed the basics of micro-fabrication and imaging using a FIB system. The following section discusses a milling process that allows arbitrarily shaped refractive micro-optical elements to be sculpted.

4.3.4. Subtractive Milling Process

Subtractive milling relies on quantization of the optical element surface into discrete heights. Each height can be represented by basic geometrical shapes or a more complicated stream file. In this work, we present the fabrication of radially symmetric diffractive optical elements. For these structures, the basic geometrical shapes are rings and circles. The technique may be applied to structures that are not radially symmetric. The depth profile of a spherical lens or mirror of radius R is

$$h = R - \sqrt{R^2 - (W/2)^2}\ , \tag{5.6}$$

where W is the diameter of the micro-optic element. Figure 5.14(a) shows the quantization of a mirror surface into N levels of equal spacing $\delta h = h/N$. The radius of each level is calculated from equation (5.2).

$$\rho_i = \sqrt{R^2 - (R - (N-i)\delta_i)^2}\ , \qquad i=0,1,\ldots,N\text{-}1 \tag{7}$$

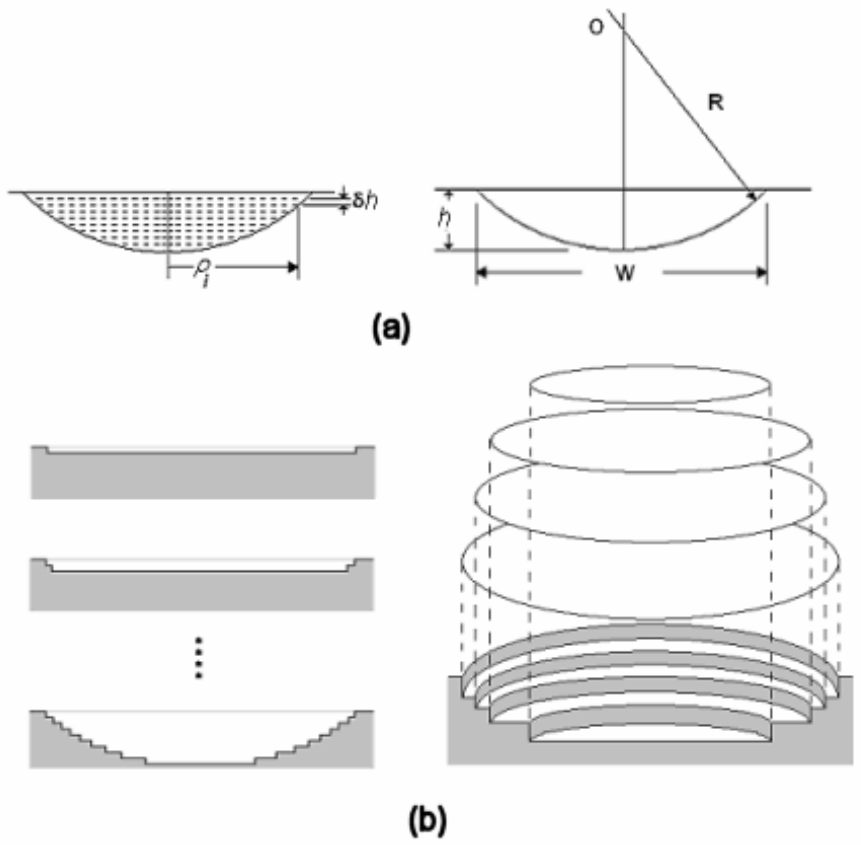

Figure 5. 14: (a) Quantization of the spherical mirror (b) subtractive milling technique; *N* concentric circles are milled sequentially starting by the largest one results in a multi-level spherical mirror

To fabricate a spherical mirror, a script was written to calculate the radii of *N* concentric circles according to Eq. (5.7). As shown in Fig. 5.14(b), each circle is milled to a depth of δh starting with the largest radius, $\rho_o = W/2$. In the case of a positive focal length

micro-lens, the script generates *N* concentric rings of inner radii calculated from Eq. (5.7) and outer radii that are greater than or equal to *W/2*. The inner radii must be less than *W/*2. The fabrication procedure starts by milling the ring of the smallest inner radius, $\rho_{N-1} = \sqrt{2R\delta h - \delta h^2}$ to a depth of δh, followed by the next smaller ring, and so on until the mirror is completely milled into the substrate as shown in Fig. 5.14(b).

5.3.5. Integrated Mirror Example

As an example of the subtractive milling technique, a micro-optic element was integrated onto the surface of a silicon v-groove mirror. One advantages of FIB milling is the ability to mill into tilted surfaces. The v-groove was fabricated by wet etching and was designed to passively align an optical fiber as shown in Fig. 5.15(a). A silicon wafer was coated with a layer of SiN and patterned using a g-line stepper with 5X reduction. The patterned areas were dry etched in an RIE plasmatherm for 12-14 minutes to remove the SiN. The sample was chemically etched in a KOH chemical bath at 90^{o}C for five hours. This resulted in 54.7^{o} tilted walls corresponding to the crystal lattice planes of the silicon wafer. Figure 5.15(b) shows the geometry of the optical element that was fabricated. As illustrated in the figure, the distance between the fiber and the mirror, r_1, defines the location of the image point. Due to the finite size of the mirror aperture, the maximum distance that the fiber can be placed in front of the mirror is restricted to a few hundred

microns. For a v-groove with wall angle θ, the location of the fiber center relative to the surface of the v-groove l_t can be calculated from the geometry shown in Fig. 5.15(a) as follows

$$l_t = D\ \tan(\theta) - \frac{r}{\cos(\theta)} \tag{5.8}$$

where D is the half width of the v-groove. For the v-groove to include the full cladding region of the fiber, l_t must be greater than r, the radius of the cladding.

$$D \geq r\frac{\cos(\theta)+1}{\sin(\theta)} \tag{5.9}$$

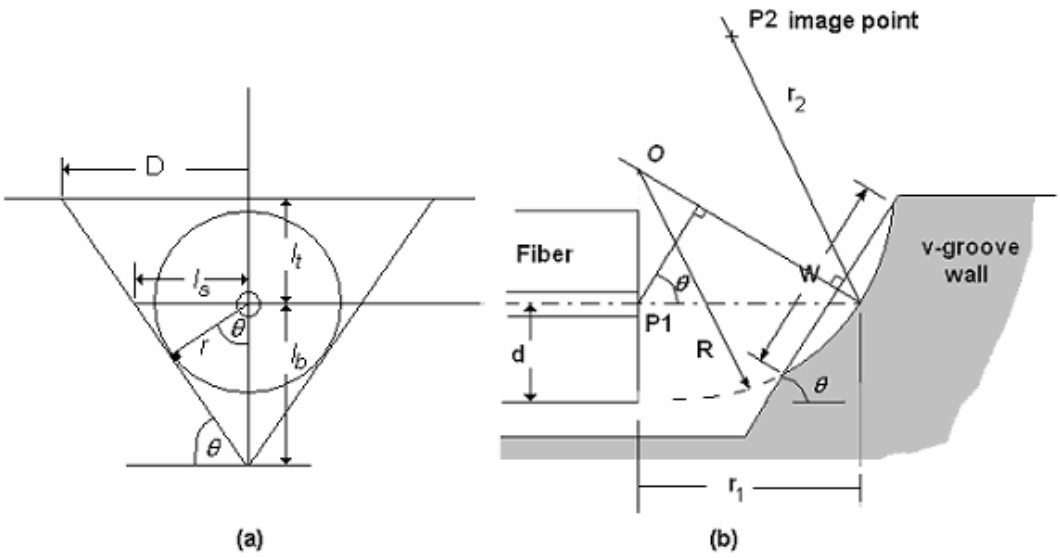

Figure 5. 15: (a) Geometry of the fiber inside the v-groove. (b) The location of the fiber relative to the integrated micro lens.

For a specific v-groove of width 2*D* and wall tilt angle θ, the lens must be fabricated so the center is located at a distance l_t under the v-groove surface. For this work, W=340 μm, *D*=170 μm, and *r*=62.5 μm. Using Eq. (5.4), the height of the center of the mirror should be 127.65 μm. The mirror diameter limited the maximum distance the fiber can be moved, r_1, while the beam was still within the mirror as shown in Fig. 5.15(b). The maximum distance, $r_{1(max)}$, was calculated using Gaussian beam propagation presented in Eq. (5.10).

$$r_1\big|_{\max} = z_o\left(\sqrt{\left(\frac{W}{2\ w_o}\right)^2 - 1}\right) - \frac{W}{2}\cos(\theta) \qquad z_o = \frac{\pi w_o^{\ 2}}{\lambda} \tag{5.10}$$

where w_o was the mode field radius of the single mode fiber. The location of the minimum beam waist, r_2, at the image location P_2 is defined as

$$r_2 = \frac{R}{2} + \frac{\left(\frac{R}{2}\right)^2\left(r_1 - \frac{R}{2}\right)}{\left(r_1 - \frac{R}{2}\right)^2 + z_o^{\ 2}} \tag{5.11}$$

where, *R* is the radius of curvature of the mirror as shown in Fig. 5.15(b).

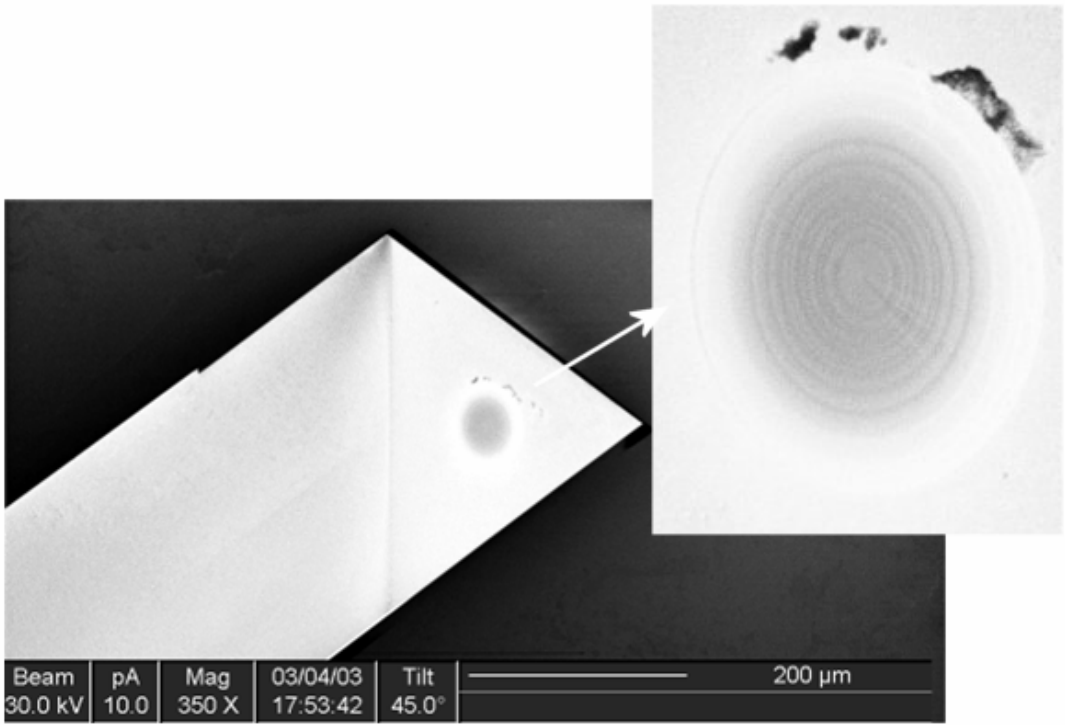

Figure 5. 16: SEM image of the micro spherical mirror fabricated on the wall of the v-groove.

CHAPTER SIX: EXPERIMENTAL VERIFICATION OF SELECTIVE COUPLING SCHEMES

In this chapter we demonstrate the experimental analysis and characterization of the different coupling schemes presented in chapter five. First, we present, in detail, the experimental results and characterization of a MMF condensing lens. A SMF is fusion spliced to a MMF of a specific length, and then we recorded the intensity distributions of the back reflected light for different wavelengths incident on a planar mirror using a tunable laser diode and a CCD camera. The subsequent analysis showed good matching to the theoretical predictions made. In the second section, we show the experimental analysis of the fabricated phase element for coupling to the LP_{11} mode. The results exhibited a great agreement with the theoretical analysis. The third section deals with the hollow-glass-waveguide (HGW) characterization and analysis. We characterized the transmission and bending losses in a meter long hollow glass waveguide and compared the measurements with the first order calculations presented in chapter five. Additionally, we measured the optical functionality of the fabricated polarization converter element as well as its influence on the bending loss in the hollow waveguide. In the last section we analyze the micro lens fabricated on the side wall of a fiber v-groove using the FIB system.

6.1. MMF as a Condensing Lens

The tunable fiber optic lens described here is unique with respect to the relative simplicity in fabrication and the ability to significantly change the focal length. It consists of a multimode fiber (Thor Labs AFS105/125) fusion spliced onto a single mode fiber (Corning SMF-28) attached to a tunable laser source via an 80/20 splitter, which allows for detection of any returning signal. Agilent 81635A InGaAs power sensor and 81640A tunable laser modules were used in conjunction with the 8164A Lightwave measurement system to make the measurements presented in this paper.

For the fiber parameters cited in table (3.1), the mode associated with maximum coupling is ν_p=4. This can be observed looking at Figure (4.2) which shows the relationship between the coupling efficiency and the mode number for MMF core radii of 52.5μm and 92.5μm respectively. Using these parameters at a wavelength of 1.55μm results in L_p = 3.2369mm. From equation (4.22), the re-imaging location is found to be $z_{re-imaging} = 13L_p = 42.08$ mm. Using these values, Figure (6.1) is constructed in order to represent the intensity distribution along the axis of the multimode fiber with the length in the z-direction normalized to L_p. As mentioned in the theory section, the most significant feature is the presence of very distinguished maxima at locations such as $3L_p$, and $10L_p$. The length of the MMF spliced onto the SMF can be chosen with respect to these distinguished maxima observed inside the MMF.

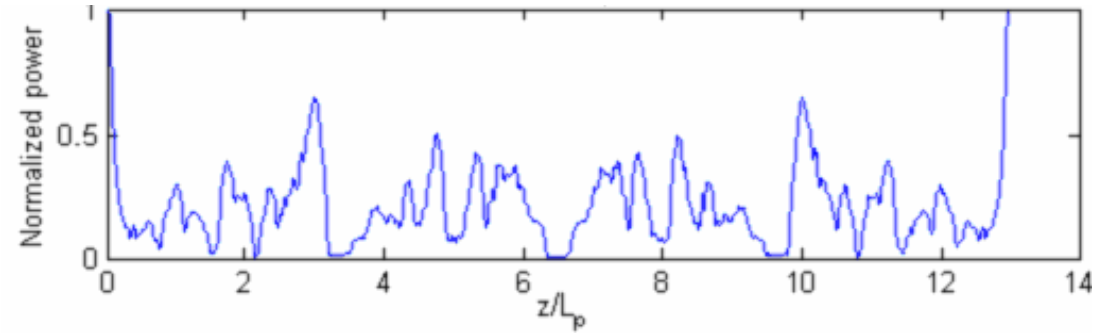

Figure 6. 1: Power, normalized to the input power, across an area equals to the SMF core along the MMF

By cleaving the multimode fiber at a length slightly less than the length specified at any one of these locations, the light exiting the fiber converges to an on-axis location in the air outside the fiber as depicted in Figure (6.2). In this case, the fiber end facet is located at a longitudinal location that corresponds to a length slightly less than that defined for the m=3 case in equation (4.19). If a mirror is placed at this same plane, the coupling of the light reflected back through the fiber would be a maximum compared to any other location in the near vicinity which indicates the location of the focal plane. Thus, the shift in the focal plane can be experimentally measured by detecting the power reflected from a mirror placed in front of the end facet of the MMF while sweeping the wavelength.

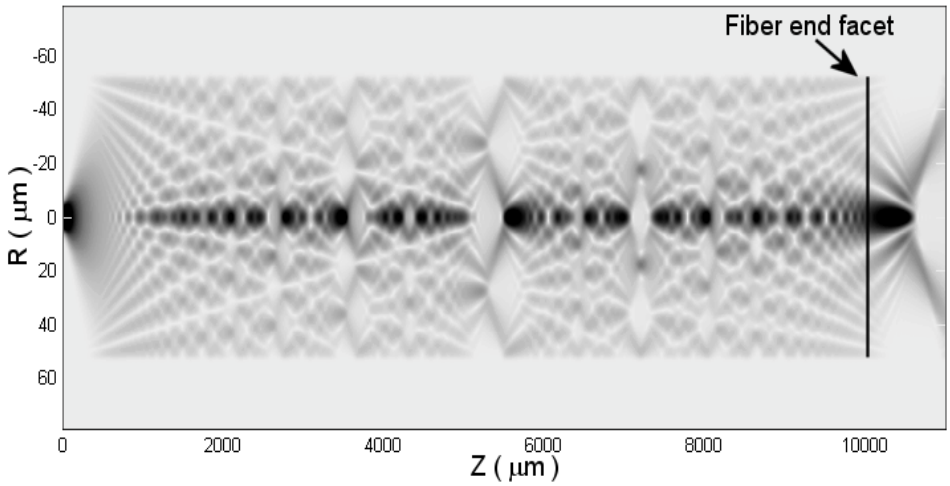

Figure 6. 2: Calculation of intensity inside multi-mode fiber ($\lambda = 1.55$ μm) using equations (5) and (25) for the field inside and outside the MMF. The MMF is polished slightly less than 10 mm (corresponds to $3L_p$). [SMF of 4.5 μm core radius and MMF core radius of 52.5 μm.]

To verify the validity of choosing the a length of MMF less than the m=3 case, a scalar cylindrically symmetric FD-BPM simulation was performed for a single mode fiber and step index multimode fibers using the parameters depicted in table (6.1). Figure (5) shows specifically the field convergence at longitudinal on axis locations after exiting the end facet of the MMF.

In order to accurately compare experimental and theoretical results, the length of the MMF fusion spliced onto the SMF must be accurately known. The process used to fabricate this device inherently provides this information and a procedure to repeatedly

cleave the same length of MMF onto the SMF each time a device is fabricated. Using the scale on the fiber cleaver, a MMF splice length of 21 mm was produced to be fusion spliced to the SMF. Once this was done, a cleave is made 11 mm from the end facet of the MMF, leaving a length less than 10 mm long MMF spliced to the SMF. This length is conveniently slightly less than the m=3 case using the formulation of equation (4.21). The actual length of the MMF can be more closely determined using a microscope equipped with a CCD camera. Once the fusion splice interface is found, the calibrated camera software to observe microscope images can be used to provide the distance from this interface to the end facet of the MMF. The bare fiber device was then appropriately connectorized into an FC ferrule with a stereo microscope used to verify that the MMF only barely protruded through the end facet of the FC ferrule. A 0.5 μm polishing disk and colloidal slurry were then used to hand polish the end facet of the MMF until the surface was of optical quality as depicted in Figure (6.3).

The single mode fiber and step index multimode fiber used have parameters defined in table (6.1). As done in [6.1], sweeping the wavelength of the source into the SMF we observed the reflected power that results for mirror placement at specific longitudinal displacements from the end facet of the MMF. Figure (6.4) depicts the experimental setup used for these measurements.

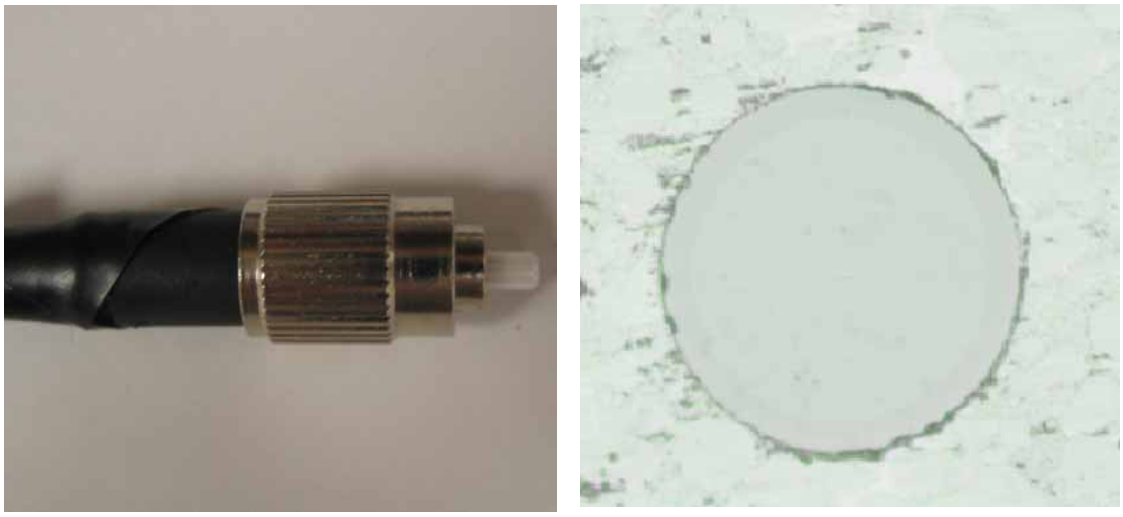

Figure 6. 3: Device connectorized in FC connector and 20x microscope image of end facet of MMF quality

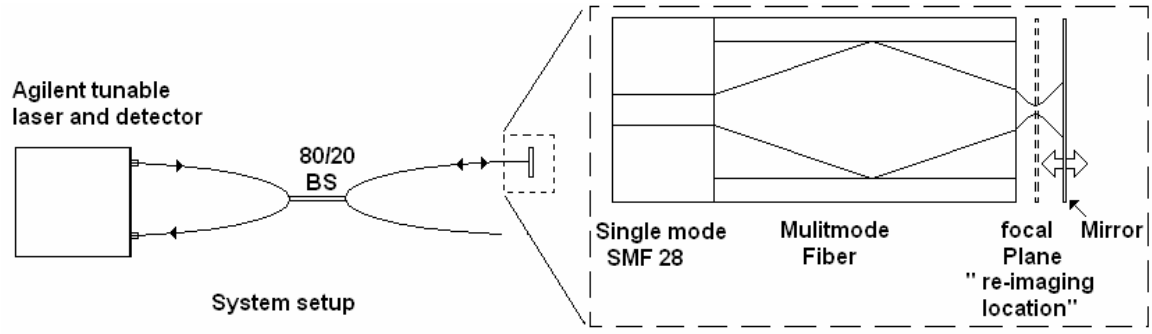

Figure 6. 4: the system setup showing the SMF fused splice to MMF.

The most notable feature for each waveform associated with a specific longitudinal displacement is the drop in output power (around 15 dBm) seen at a

particular wavelength over the 1.51-1.60 μm wavelength range. This drop corresponds to a plane located behind the focal plane at this wavelength as depicted in Figure (6.5). The shift over this wavelength range follows a linear relation that can be expressed as

$$z_{out,\exp} = -3909.7 \cdot \lambda\left[\mu m\right] + 6234.4\,\mu m \tag{6.1}$$

This drop in power can be explained by carefully observing the intensity distribution in Figure (4.1, b) specifically at the locations z = $3L_p$ and $10L_p$. Both locations correspond to local maxima along the MMF axis. For the first location, the light destructively interferes immediately after it condenses, while in the second location the destructive interference occurs before the light convergences.

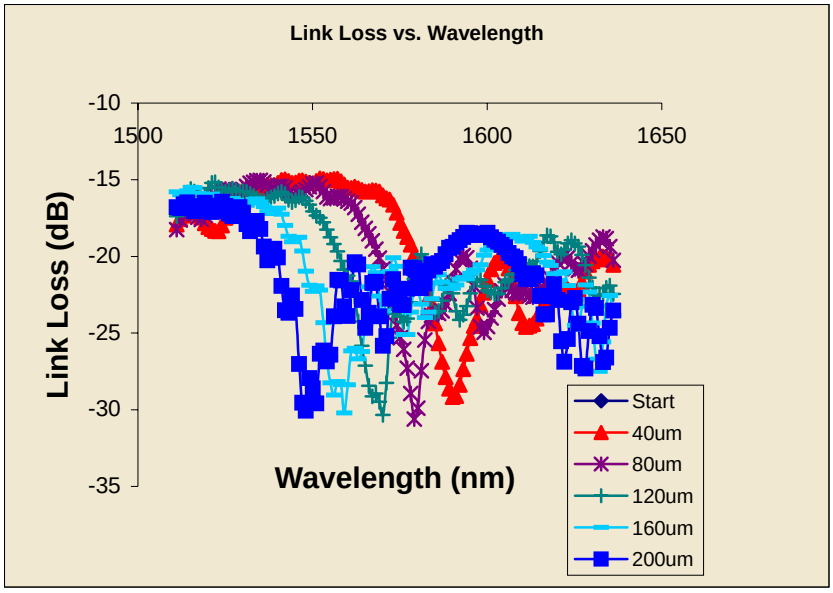

Figure 6. 5: The experimentally measured back-coupled power versus the wavelength.

As the MMF is cleaved to a length slightly shorter than $3L_p$ the drop in power is the most notable feature. Figure (6.2) shows the simulated field distribution in a region of 1 mm behind the MMF end facet using the modes expansion expressions in (4.3) and (4.33).

To compare these experimental results with the first order approximation the expression in equation (4.32) is used to calculate the location of the focal plane over this particular wavelength range.

$$z_{out} = -4208 \cdot \lambda\,[\mu m] + 6894\,\mu m \tag{6.2}$$

Equations (6.1) and (6.2) demonstrate a correlation between the experimental measurements and the predicted linear relation in equation (4.30). On the other hand, there is an error of 7% in the slope calculated using our first order approximation. This error is predictable due to the approximations carried while driving the expression presented by equation (4.30). In addition, a cylindrical symmetric FD-BPM is used to simulate the experimental setup.

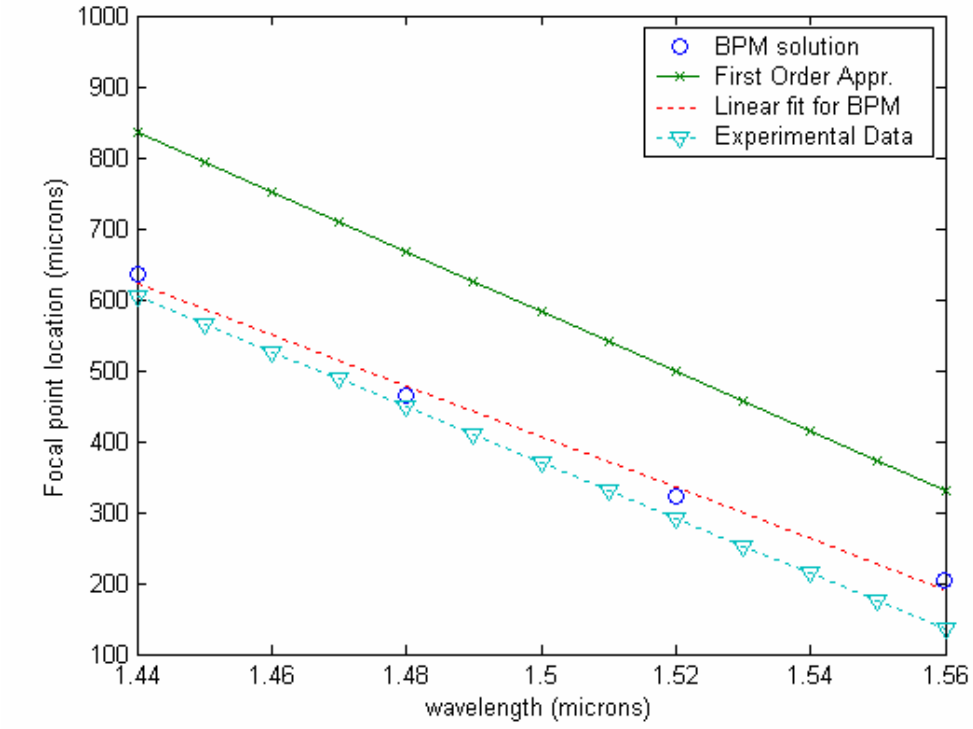

Figure 6. 6: FD-BPM, experimental measurements, and first order results for focal point location as a function of wavelength

The power that couples back to the SMF is calculated for four different wavelengths. Figure (6.6) depicts the results obtained using the FD-BPM in addition to the experimental and the first order approximation results. The figure shows almost a constant shift of 200μm between the first order approximation and both the experimental and the FD-BPM results. This shift is due to the presence of error of about 3% in calculating the longitudinal propagation constant using the asymptotic assumption in

comparison to the exact values. This results in inaccuracy of the value of L_p and thus the calculated z_{out}. In addition, by rounding of the value of ν_p to the nearest integer, an additional error in calculating L_p is introduced. Thus, the first order approximations are seen to be able to predict the location where the light condenses outside the MMF as a function of wavelength with an acceptable error of 7%. This error is not as significant when estimating the change of the spot size at these planes over the operating range of wavelength using 1st order approximations in comparison to complete FD-BPM simulations.

The mode series expansion expression presented in equation (4.35) is used to calculate the intensity distribution outside the MMF for four wavelengths: 1.44, 1.48, 1.52 and 1.56 μm as depicted in Figure (6.7).

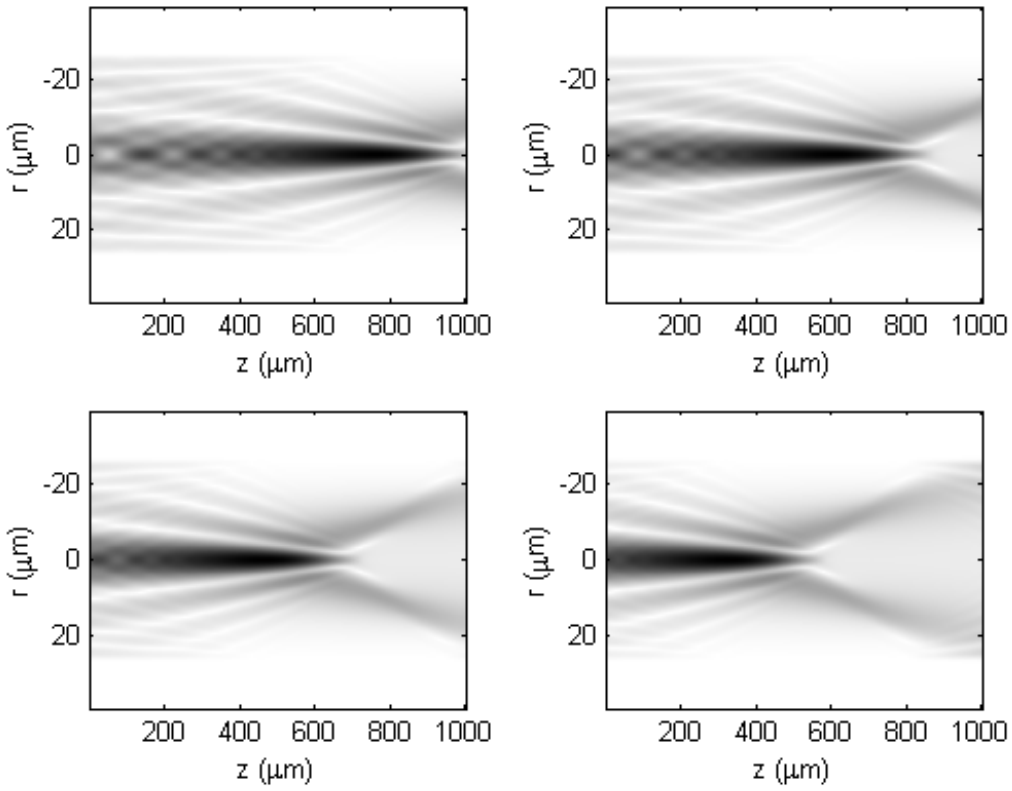

Figure 6. 7: Simulated field distribution out of the MMF facet for four different wavelengths demonstrating wavelength dependence of focal position.

The HWHM spot sizes at the focal planes are depicted in Figure (6.8) together with the experimentally measured data and the results from FD-BPM simulations. Looking at the curves in Figure (6.8), it is apparent that the spot size slightly decreases as the wavelength is increased. An interesting property of this device is the size of the beam at the focus location associated with a particular wavelength. To enhance the idea of the

actual size of a beam at a focus location, the experimentally measured beam is depicted in Figure (6.9), overlaid on the actual size of the MMF end facet.

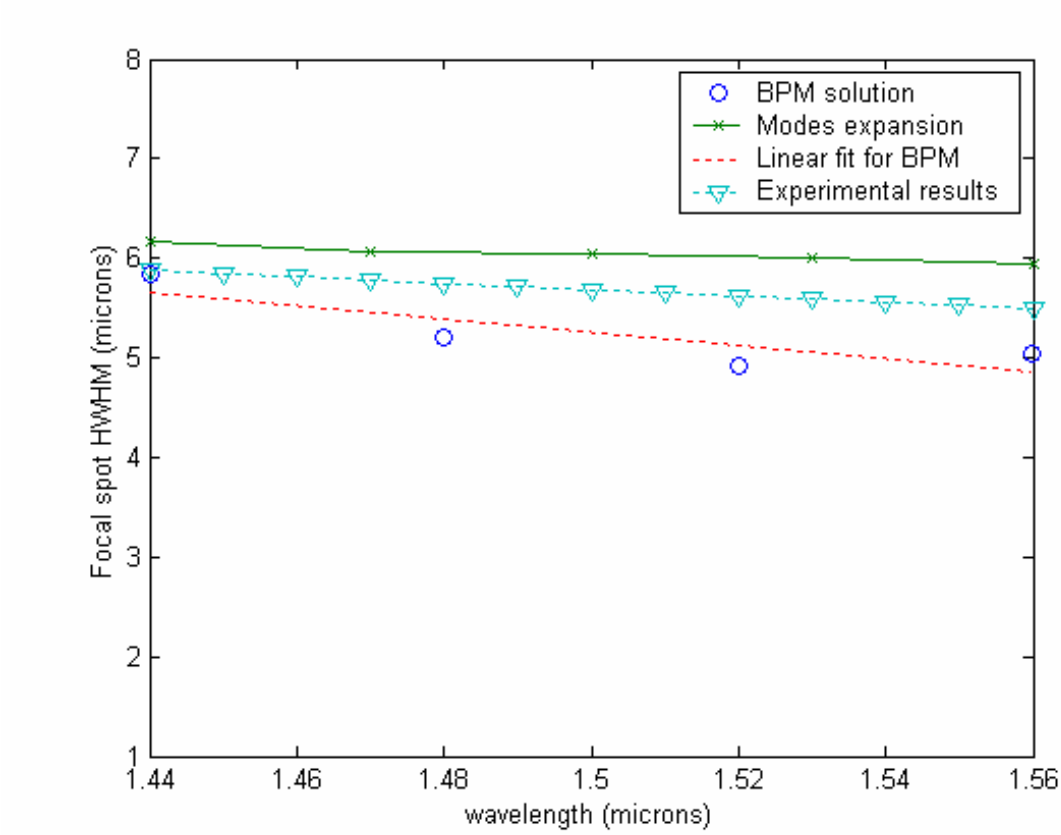

Figure 6. 8: Spot size (HWHM) at focal location as a function of wavelength for BPM, first order solutions, and experimental results.

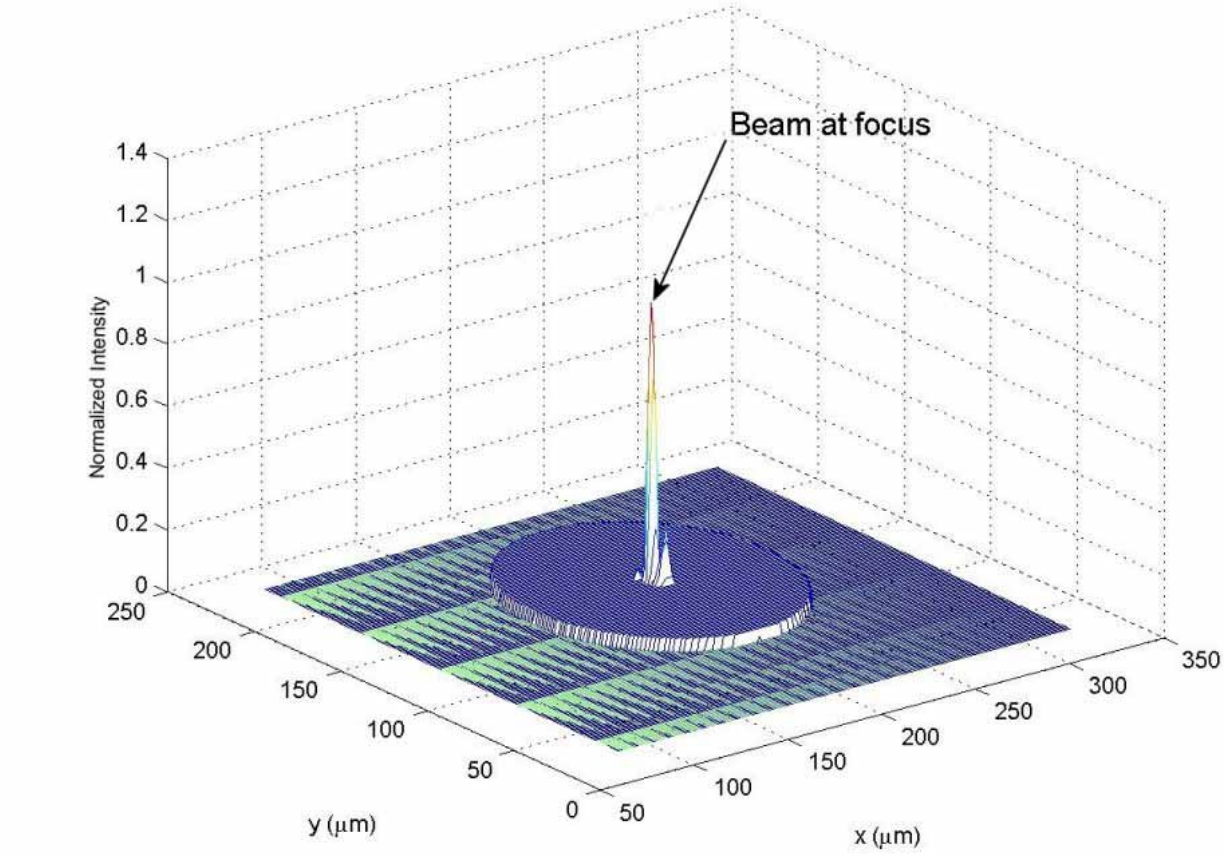

Figure 6. 9: Depiction of exiting beam at focus location overlaid on actual size of MMF end facet.

6.2. Excitation of LP_{11} and LP_{21} in Large Core Fiber Using Single Phase Element

In our experimental setup, a HeNe laser source is coupled to a single mode fiber and the output is then collimated using a 20x objective lens. The phase modulated light is then

coupled into a larger core fiber which sustains a few modes using a 20x objective lens with effective focal length of 9 mm. The fiber used is Corning SMF 28 which is single mode at 1550 nm, and supports four modes at a wavelength of 632.8 nm. Without any phase elements, we maximized the light coupled to the LP_{01} to guarantee minimum tilt and shift in the input beam. The phase elements shown in Figure (5.2, a and b) were fabricated in Shiply PR1805 photo resist using a stepper system. The refractive index of the photoresist is 1.6406 at the working wavelength. To achieve a π phase shift the step height was set to 494 nm. For the element depicted in Figure (5.2, a), the resulting far field intensity distribution at the output of the fiber is depicted in Figure (6.9, a). The figure shows that the light is selectively coupled to the LP_{11} mode. Measuring the output power, 81.4% of the power at the input facet of the large core fiber is coupled to the LP_{11} mode. This value is very close to the calculated coupling efficiency of 83.7% using equation (4.80). Nevertheless, only 60% coupling efficiency was achieved when using the second phase element to selectively excite the LP_{21} mode. The far field distribution after the large core fiber is presented in Figure (6.10, b). However, in both cases the cross talk is minimized when properly aligning the input light and the phase element to be on axis with the few modes fiber.

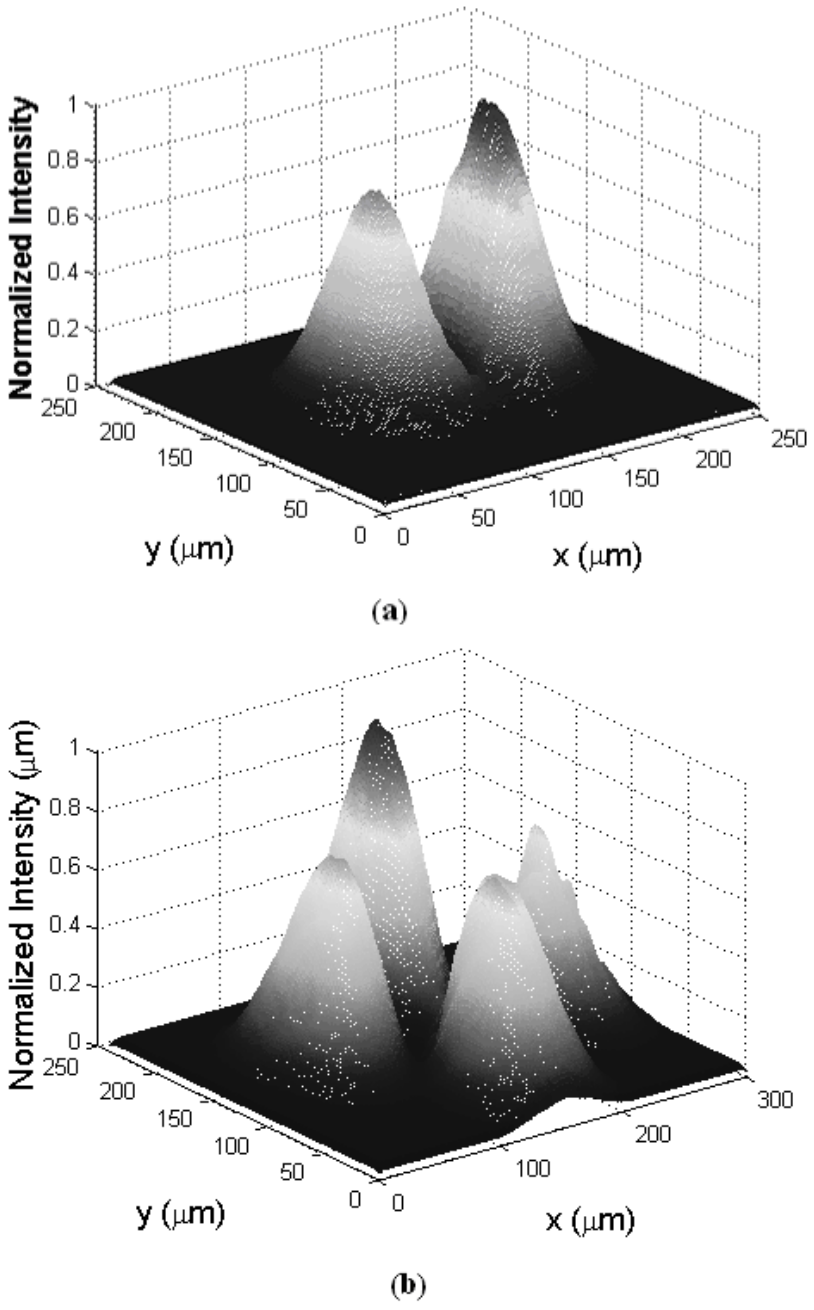

Figure 6. 10: Observed far field intensity distributions of the light at the out of the fiber using the (a) first phase element and (b) the second phase element.

6.3. Numerical analysis of the selective excitation of the highest order supermode in seven core fiber

In this section, we calculate the effect of the tilt and shift of the input beam on the coupling efficiency to the highest order supermode. Figure (6.11) depicts the change of the coupling efficiency when tilting and shifting the input beam. One notices that the efficiency is more sensitive to tilting than shifting. Thus, a very precise alignment is required to achieve high coupling efficiency.

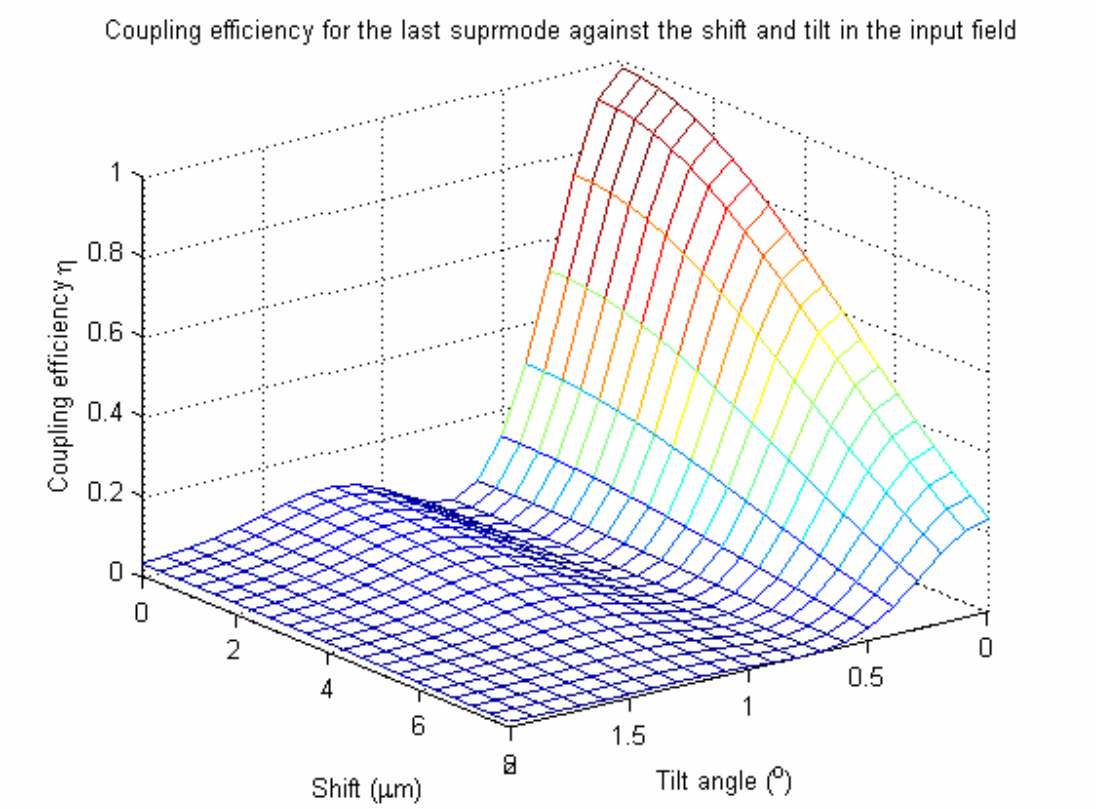

Figure 6. 11: Coupling efficiency to the last supermode in seven core fiber against the tilt

and shift in the input beam.

6.3. Selective Coupling to TE_{01} mode in HGW

In chapters four and five, we have illustrated the design and fabrication of polarization converter element to selective couple to the TE_{01} mode in order to minimize the bending loss in hollow waveguide. Here, we first characterize the transmittance and bending losses in glass hollow waveguide, and then study the optical behavior of the fabricated polarization converter element and its effect on the transmission and bending losses in the fiber.

6.3.1. Measurement of the Transmission and Bending Loss in HGW

Figure (6.12) depicts an SEM image of the HGW we used in our experiment. In any HGW, the thickness and refractive index of the dielectric and metal layers essentially affect the bending and transmission losses of this waveguide. As can be seen in Figure (6.12), the dielectric layer (AgI) has is 1.21 μm thick, while the thickness of the metal (Silver) layer is about 625 nm. At a wavelength of 1.55 μm, the refractive indexes of the AgI and silver layers are 2.138 and 11.9+i61.9 respectively. To measure the transmittance and bending losses we used a 91.5 cm long piece of this HGW as depicted in Figure (6.13).

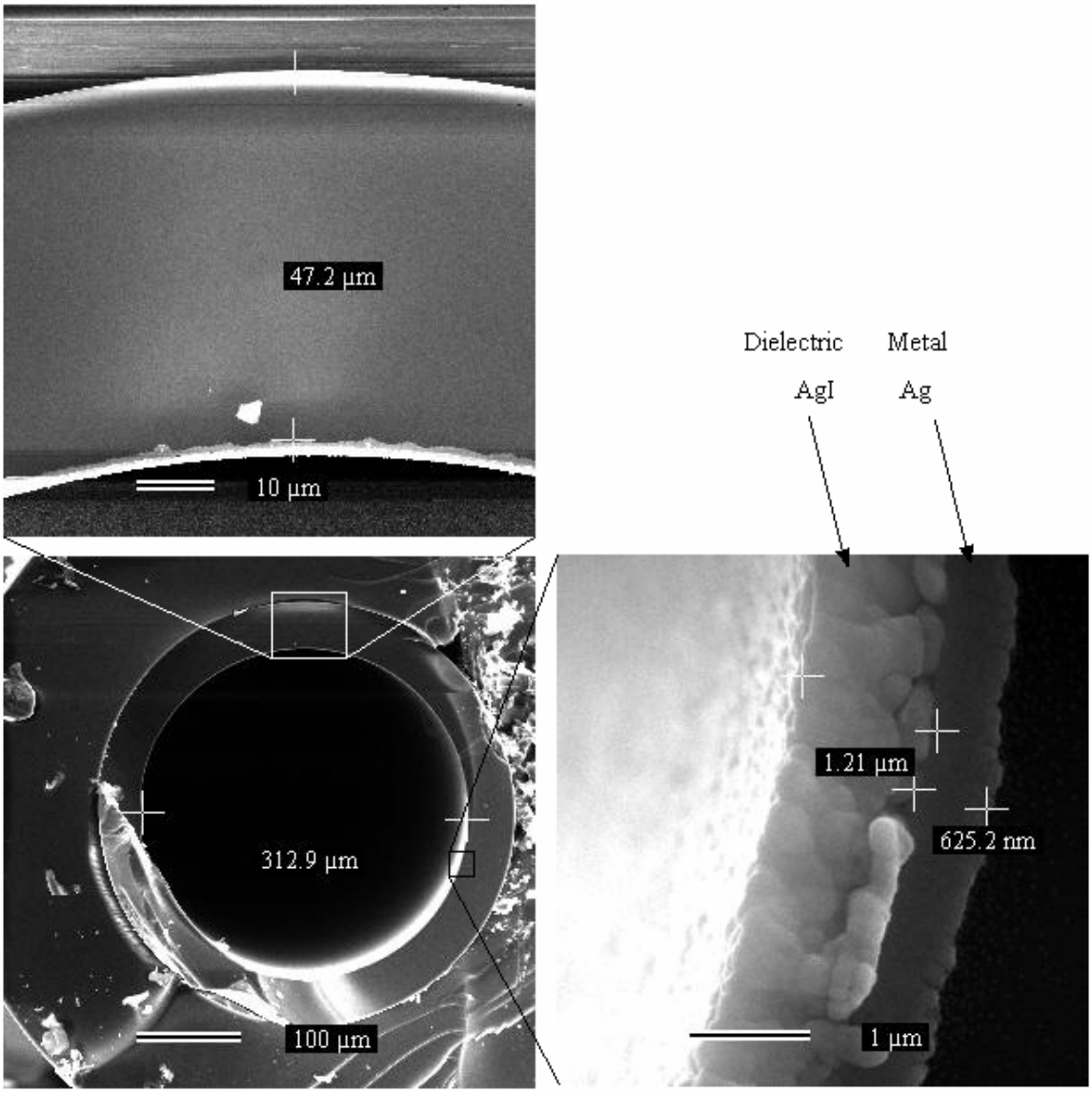

Figure 6. 12: SEM images of the HGW showing the dielectric (AgI) and the metal (Ag) layers.

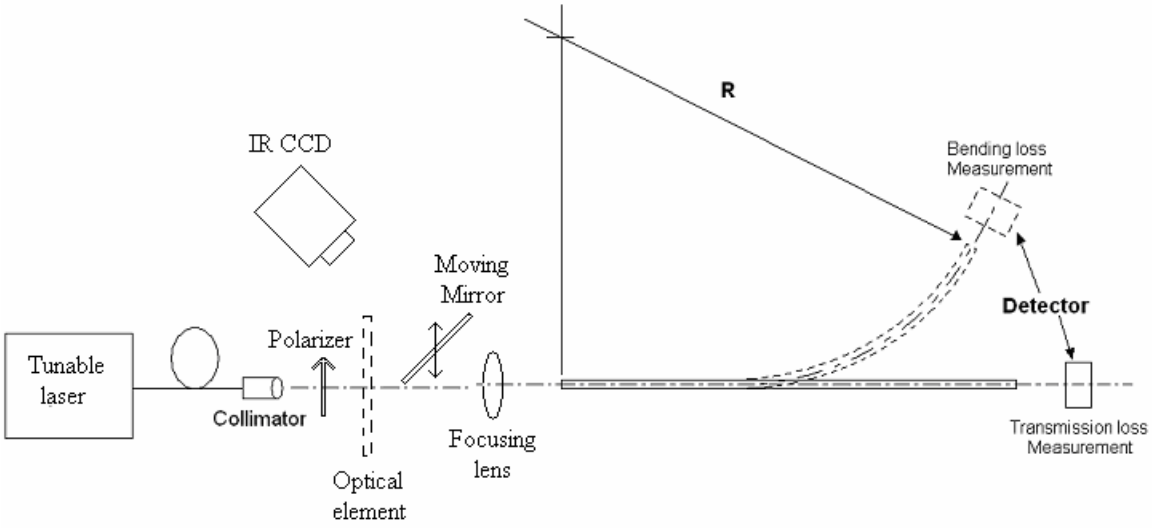

Figure 6. 13: Experimental setup for measuring transmission and bending losses in HGW.

In this setup, we used a tunable laser diode source with a wavelength range between 1.540 and 1.565 μm. The source is pigtailed to a SMF at 1.55 μm with a collimating lens at the output of this fiber. A linear polarizer is placed in front of the collimator in order to fix the polarization of the input light to be perpendicular to the plane of incidence. The moving mirror slides across the optical path and reflects the light towards an IR CCD camera where a far field image is formed. These mirror and camera are important for rough alignment as well as for capturing images of the far field intensity when using the optical element. When the mirror is not crossing the optical path, a focusing lens (10 cm focal length) is used to maximize the coupling to the HGW. First, we aligned the light out of the collimator to the center of the HGW when it is straight (no bending) through

three dimensional stage in addition to tilt and rotation stages. Alignment is achieved by maximizing power read by the detector. The amount of power measured directly out of the collimator is about 2.6 mW. However, the measured transmitted power in the fiber, when it is straight, is 1.24 mW. Hence, the transmittance of this HGW is 0.4769 and the power attenuation coefficient is about 0.407 m^{-1}.

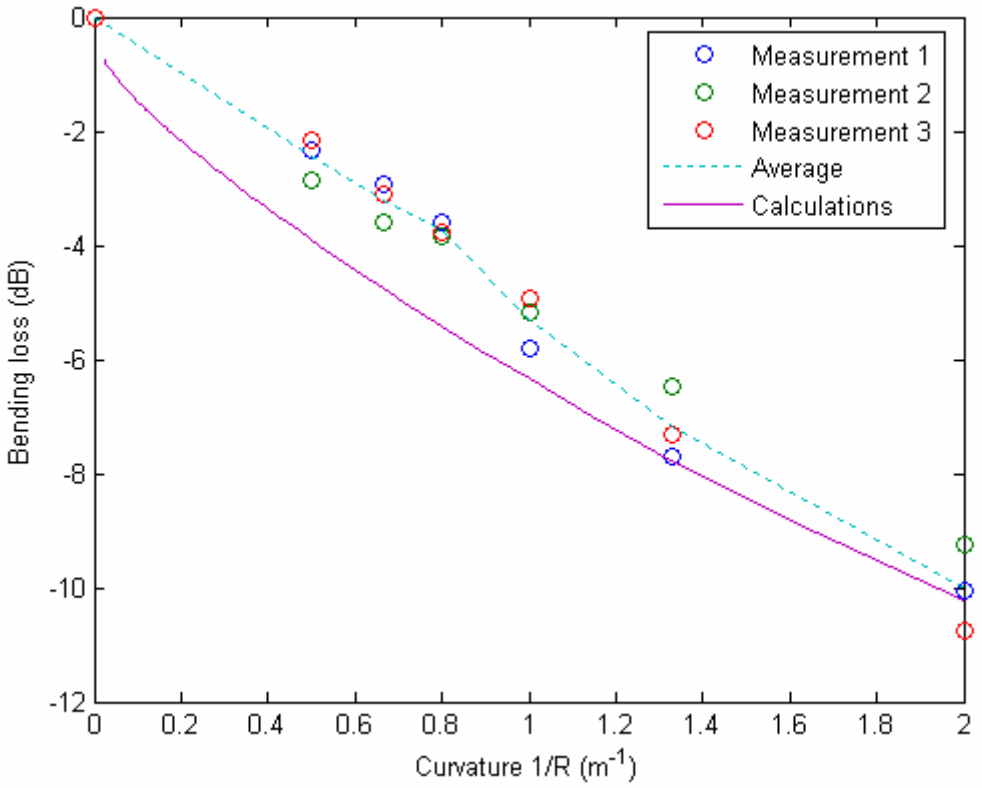

Figure 6. 14: The measured bending loss in HGW (circles represent three different measurement and the dashed line is the average) and the calculated bending loss using equation (3.57).

Using equation (3.60) and the HGW parameters defined in Figure (3.8), the calculated power attenuation coefficient is 0.398 m^{-1} which is close to the measured one. Bending the fiber with different radius of curvatures, we recorded the readings of the detector behind the fiber as shown in the setup depicted by Figure (6.13). Figure (6.14) shows the measured bending loss in the HGW at 1.55 μm as well as the calculated bending loss using equation (3.57).

6.3.2. Characterization of the Fabricated Polarization Conversion Element

In chapters four and five, we demonstrated the design and fabrication of a subwavelength structure phase element that converts the linearly polarized input light into a rotating one for selectively excitation of the TE_{01} mode inside HGW. In this section, we are going to test the optical performance of the element fabricated in GaAs substrate. Additionally, we will show that by placing this element in the path of the input light, the transmittance of the HGW improves considerably.

As presented in chapter five, the polarization converter element is fabricated in a GaAs substrate which has a high refractive index (n_{GaAs} = 3.3737 at λ=1.55 μm.) Hence, the maximum transmittance through the substrate itself is calculated through Fresnel reflection as follows

$$T = (1 - R)^2 , \tag{6.3}$$

where

$$R = \left| \frac{1 - n_{GaAs}}{1 + n_{GaAs}} \right|^2 . \qquad (6.4)$$
$$= 0.2943$$

Thus, the maximum transmittance is 0.4977. However, the multiple reflections from the two sides of the wafer (Fabry Perot) cause the change of the transmittance with the wavelength as depicted in Figure (6.15). As can be seen in the figure, the maximum transmittance is about 0.465 which is very close to the calculated one.

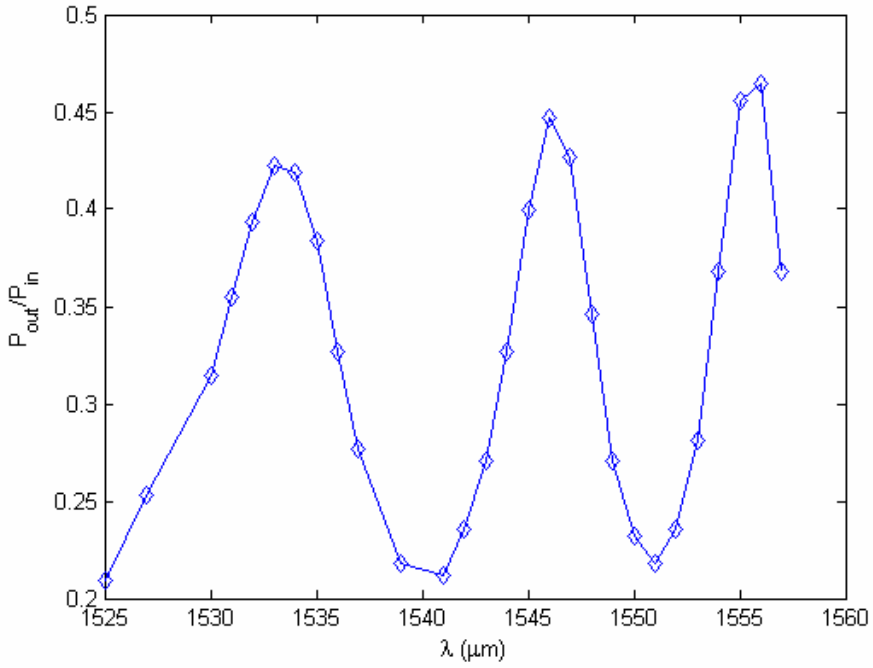

Figure 6. 15: Transmittance through the GaAs wafer as a function of wavelength.

To characterize the performance of this element, we placed it in the setup depicted in Figure (6.16) below.

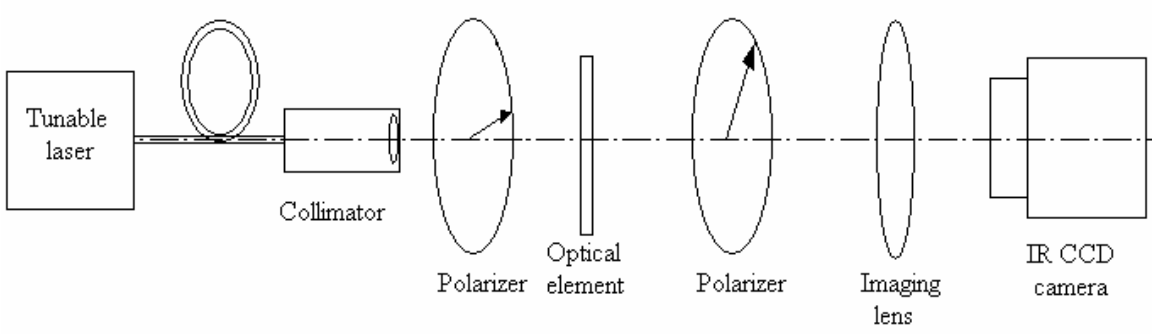

Figure 6. 16: Experimental setup for testing the performance of the polarization converter element.

In this setup, the Source is pigtailed to a SMF at 1.55 μm with a collimating lens at the end of this fiber. The first polarizer fixes the polarization of the light to be parallel to the table. However, the second polarizer is used to analyze the polarization distribution of the light out of the optical element. This can be done by rotating the polarizer and recording the intensity distributions for different rotation angles using the imaging lens and the IR CCD camera.

Using this setup, we first recorded the far field pattern without the second polarizer as depicted in Figure (6.17). As can be seen, the intensity distribution is a donut shape which matches the predicted one for the TE_{01}mode.

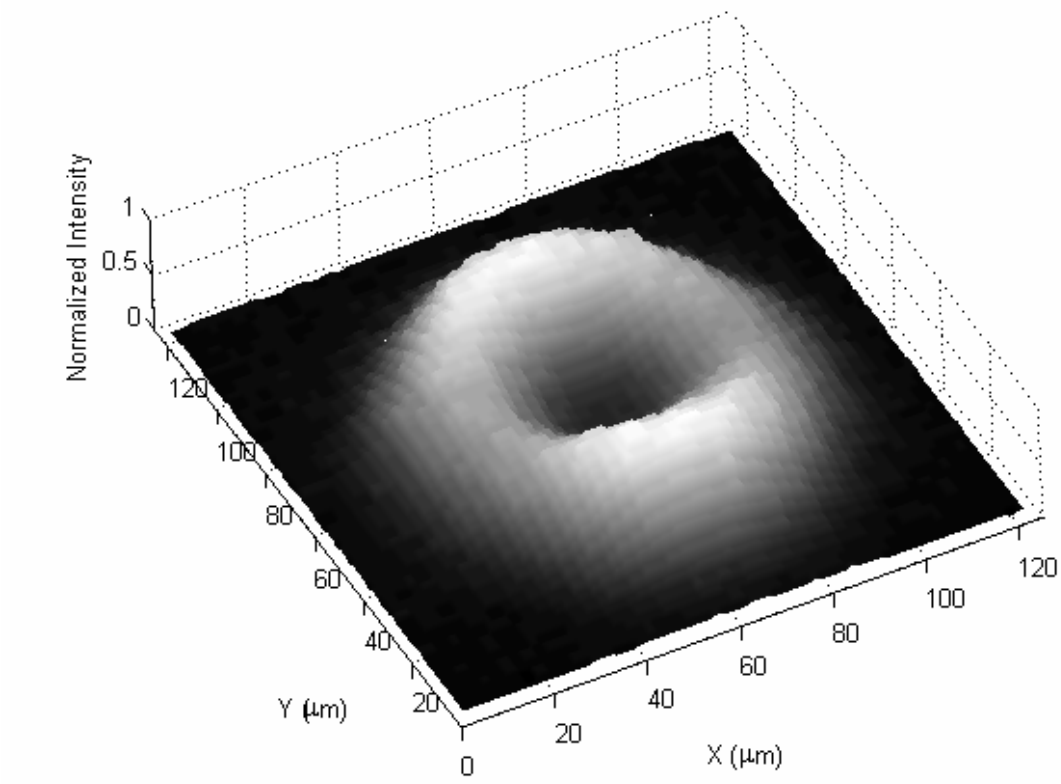

Figure 6. 17: The far field intensity distribution of the light out of the polarization converter element.

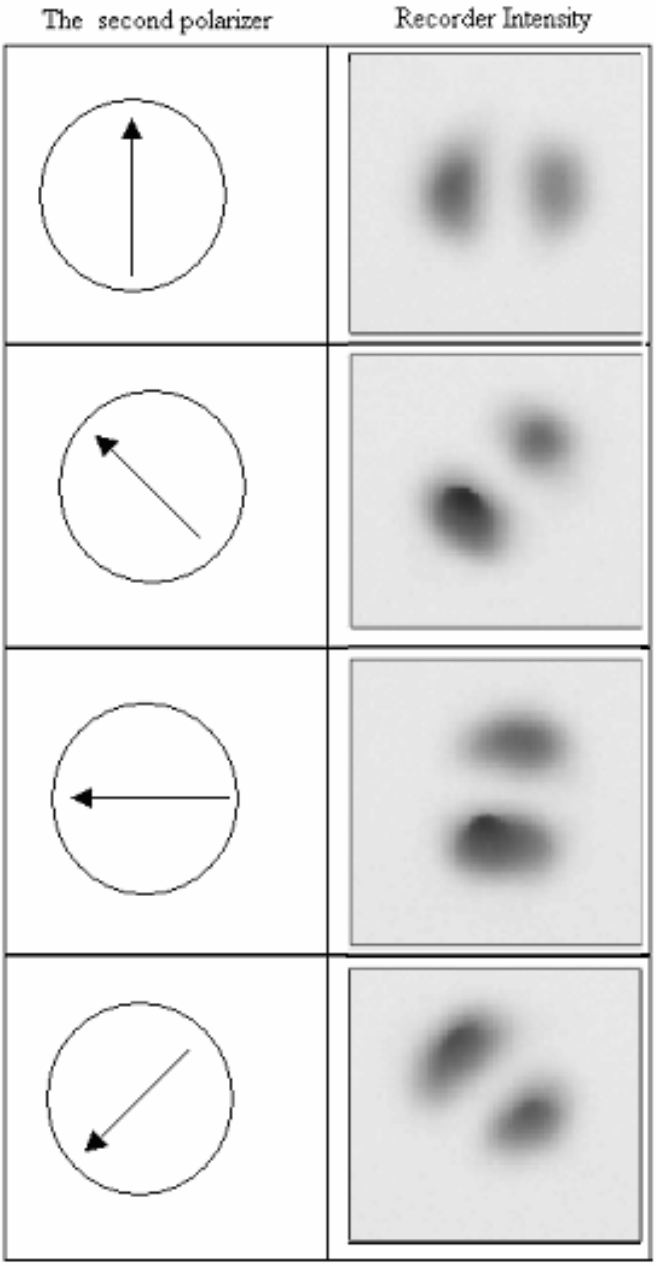

Figure 6. 18: Far field intensity distributions for different polarization angles for the light out of the polarization converter element.

As can be seen in Figure (6.18), when rotating the second polarizer the recorded intensity pattern is, basically, a section of the field out of the polarization converter element. This section rotates correspondingly with the polarized. That indicates that the polarization distribution of the output field is similar to that in Figure (4.13, b).

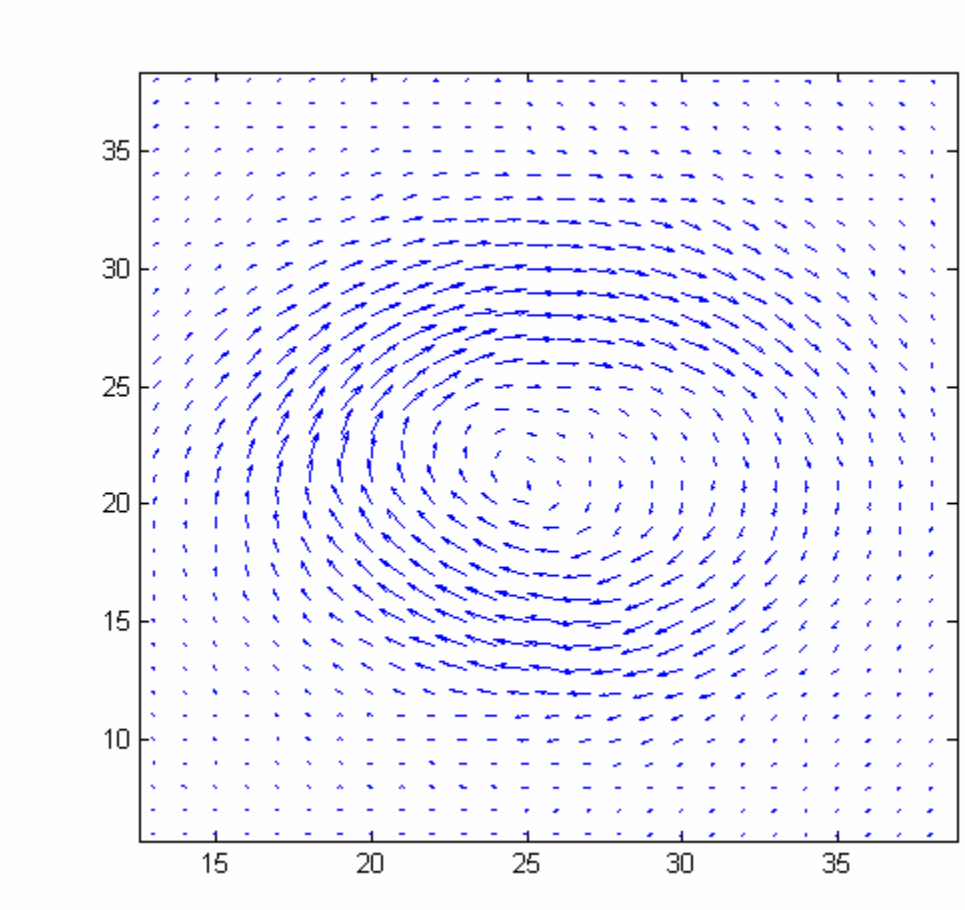

Figure 6. 19: Measured polarization distribution of the output field.

The polarization distribution of the output field can be constructed from the recorder

intensity patterns by, first, multiplying each intensity distribution with a vector corresponding to the polarization state taking into consideration the flip of the sign across the center of the pattern. These vectors are then added together to form the desired polarization distribution as depicted in Figure (6.19).

6.3.3. Characterization of the Transmission Loss on the HGW When Using the Polarization Converter Element

In chapter four, we mentioned that the polarization distribution of the output field is strongly dependant on the input polarization state. For instance, if the polarization converter element is oriented as in Figure (4.12) the polarization profiles for both horizontal and vertical input polarizations are depicted in Figure (6.20). As can be noticed, the polarization profile of the output field for the case of a vertically polarized input field matches the TE_{01} mode, while for the horizontal polarization it matches the TM_{01} mode. Thus, one expects a strong dependence of the transmittance of the HGW on the input polarization when using this polarization converter element. For a vertically polarized input field, the light is mainly coupled to the TE_{01} mode and thus the transmission loss is expected to be minimized. In contrast, for the horizontally polarized input field, the light is mainly coupled to the TM_{01} mode and thus the transmission loss is maximized.

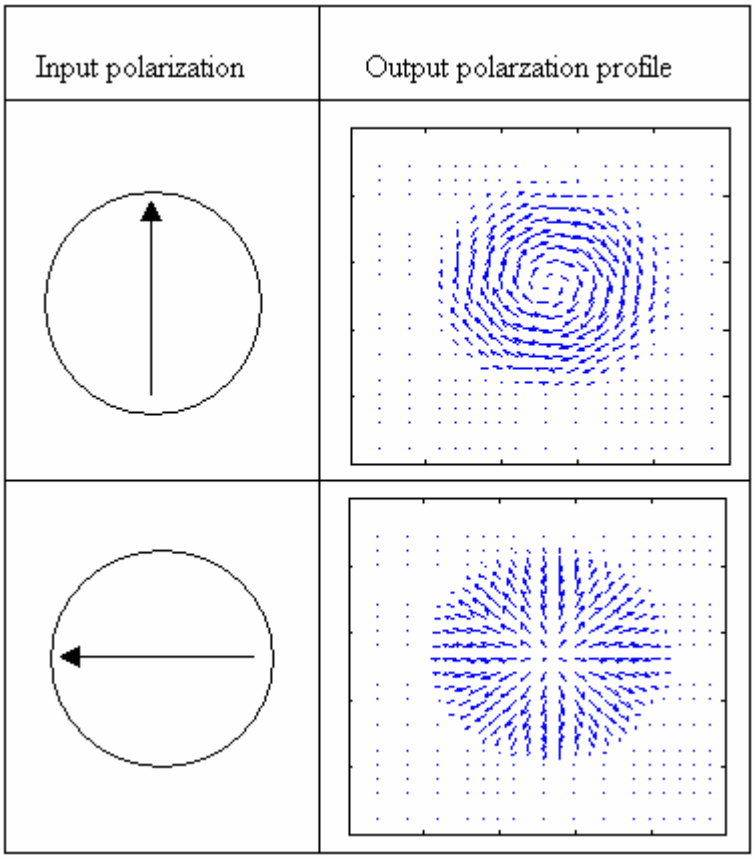

Figure 6. 20: The polarization profiles of the output field for two input polarization states: vertical (top) and horizontal (bottom).

In general, for a linearly polarized light with an angle ψ relative to the horizontal axis, the intensity absorption coefficient, with the support of equation (3.60), can be analytically written as

$$2\alpha = 2\alpha_{TE} \cdot \sin\psi + 2\alpha_{TM} \cdot \cos\psi \,, \tag{6.5}$$

where

$$2\alpha_{TR} = k_o \frac{8U_o^{\ 2}}{(k_o a)^3} \mathrm{Re}\{z_{TE}\}, \tag{6.6}$$

and

$$2\alpha_{TM} = k_o \frac{8U_o^{\ 2}}{(k_o a)^3} \mathrm{Re}\{y_{TM}\}. \tag{6.7}$$

where z_{TE} and y_{TM} are the normalized impedance and admittance of the multilayer structure of the HGW inner wall as defined in [27].

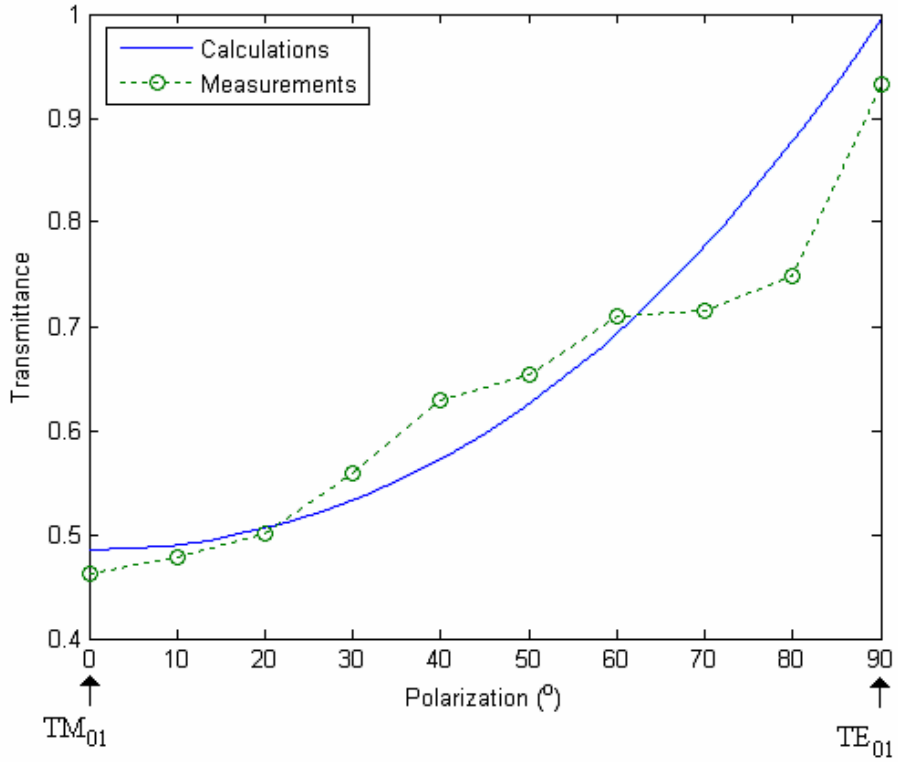

Figure 6. 21: The Calculated (solid) and measured (dashed) transmittance as a function of the input polarization angle measured relative to the horizontal axis.

Experimentally, this dependence of the transmittance inside the HGW on the input polarization can be measured by recording the transmitted power for different orientations of the element relative to the polarizer in the setup depicted in Figure (6.13). Figure (6.21) shows both the measured transmittance and the calculated one as a function of the angle of the polarization relative to the horizontal axis. The figure shows a good agreement between the measurements and the theory. In addition, one can notice from the figure that the transmittance for the TM_{01} case is almost the same when there is no element present. Thus, the light was mainly coupled to the TM_{01} mode in that case.

As a conclusion of this section, by placing the fabricated polarization converter element with a vertically polarized input field, the transmittance through a 0.915 m piece of the HGW increased from 46.3% to 93.2%. In other words, the transmission loss is decreased from 1.827 dB/m to 0.168 dB/m.

5.4. Characterization of the micro lens integrated on a fiber v-groove using the FIB system

For the substrate used herein, the calculated milling rate, from equation (5.5), was 0.168 ($\mu m^3 s^{-1} nA^{-1}$) for silicon. According to R.J. Young et al [51] those rates can be improved by almost a factor of 10, if gas assistant etching was used. Increasing the number of levels will improve the surface quality of the desired micro-optical surface; however, increasing the number of levels will increase the probability of the rings to be

shifted due to the machine error in allocating the center coordinates. Typical errors in centering the rings can be as high as 0.25 μm, which requires a balance between the number of rings and the error in their centers. We selected a radius of curvature of the spherical mirror to be 250 μm and a 78 μm diameter using the subtractive lithography resulting in 40 concentric circles. From equation (5.1), the mirror depth was 2.41 μm with a step thickness of 0.0603 μm. The calculated distance $r_{1(max)}$ and r_2 are 1.165 mm and 1.0385 respectively. We used a Ga^+ ion beam of 7nA current and an acceleration voltage of 30 kV to mill the mirror on the silicon v-groove. To mill on such tilted surface, the sample holder was tilted 54.7^o such that the ion beam in perpendicular to the v-groove wall. Figure (5.16) shows the SEM image of the fabricated spherical mirror. To measure the optical properties of the fabricated mirror, a 125 μm diameter optical fiber with a 9 μm core operating at a wavelength of 632 nm was used to illuminate the mirror as shown in the geometry of Figure (5.15). A CCD camera was placed at a fixed distance of 2.5 mm above v-groove. The Intensity of the reflected beam was recorded for different locations of the fiber facet relative to the micro lens. Figure (6.22) shows the measured x and y beam waists together with the designed beam waist and simulation results obtained using Zemax, which was modeled as a skew Gaussian beam incident at 36^o to the normal of the mirror axis. The results demonstrate good agreement between the measurements and the simulation. Astigmatism is a very pronounced feature in the curves as the light is incident off-axis to the mirror. However, this can be compensated for in the optical design if need be the case.

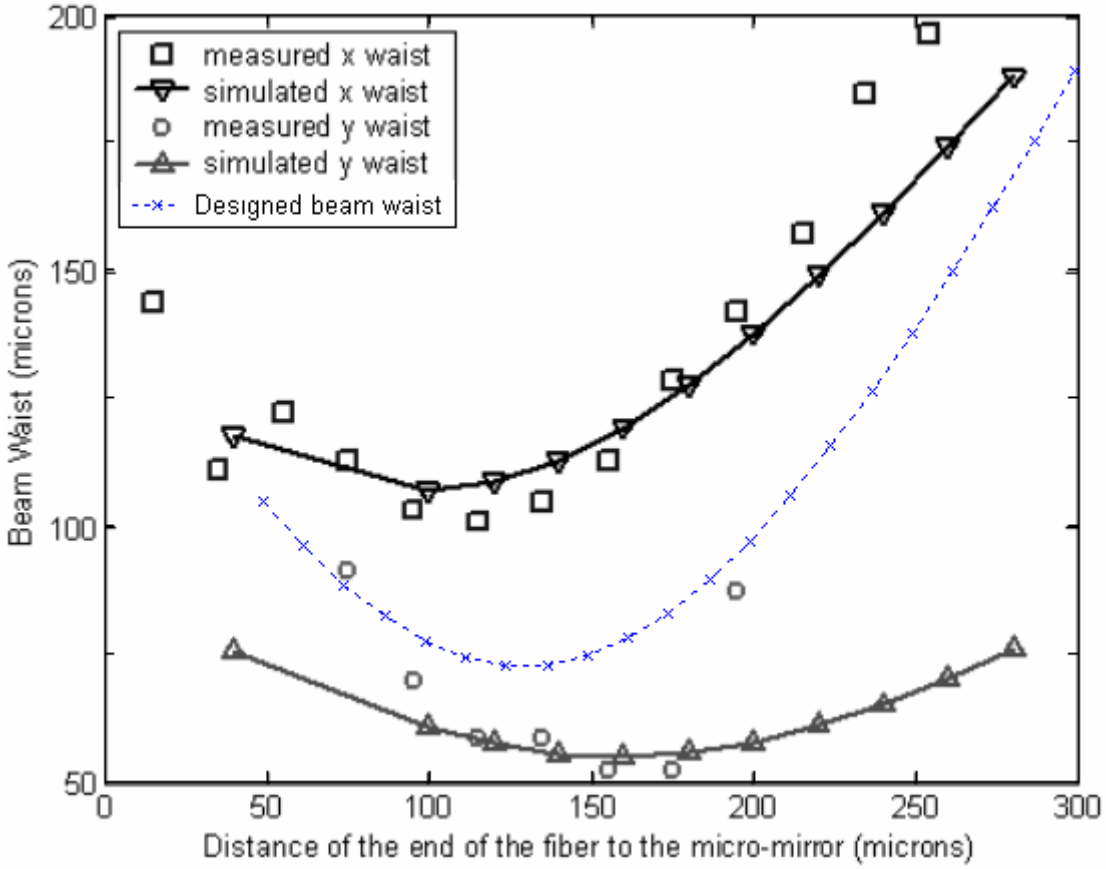

Figure 6. 22: The measured and simulated x and y beam waists at a distance of 2.5 mm above the v-groove using a single mode fiber at 623 nm.

CHAPTER SEVEN: CONCLUSION

The main scope of this research is the design, fabrication and analysis of optical components that selectively excite certain modes to improve the performance of selected optical fiber systems. Modeling the specialty fibers, we demonstrated different modeling techniques to predict the modal properties of step index fiber, multicore fiber, and cylindrical hollow waveguide. Based on these modal properties, we addressed the design of different coupling schemes. By directly coupling form a SMF to a MMF, only radially symmetric modes are excited inside the MMF. Using this coupling scheme, we demonstrated numerically and experimentally the use of this device as a wavelength tunable lens. In the second design we used a single phase element to selectively excite the LP_{11} and LP_{21} modes in a large core step index fiber that sustains few modes. A coupling efficiency of 81% was experimentally achieved for the LP_{11}. The element was fabricated using photolithography techniques. However, only 60% of the light was coupled to the LP_{21} when using a single phase element. Hence, we proposed the dual elements to match the phase and amplitude of the LP_{21} mode. Using this scheme, we illustrated numerically that more than 92% of the light is coupled to this mode. In designing this element, we used the least square error method. Additionally, we used the same coupling scheme to demonstrate the selective excitation of the last supermode in a seven cores MCF. We showed numerically that more than 96% of the light couples to this mode when designing these dual elements using the MOP.

In the third application, we demonstrated for the first time, to our knowledge, the use of a subwavelength structure to improve the transmission loss in HGW by selectively exciting the TE_{01} mode. The structure converts the input linearly polarized light into a rotating polarized one similar to the TE_{01} mode. This novel device was fabricated using EBL and dry etching in GaAs substrate using ZEP resist as a mask material. Using this device and coupling to a 300 μm bore diameter HGW, the transmission loss is decreased from 1.827 dB/m to 0.168 dB/m. These results match the theoretical predictions.

Finally, we introduced the subtractive milling technique to integrate micro elements into real devices using the FIB system. As an example, we demonstrated the fabrication of a micro lens on the tilted side of a fiber v-groove. By properly centering this lens in the side wall, the device worked as a passively aligned coupling element.

LIST OF REFERENCES

1. R. Ghosh et al, "Modal characteristics of few-mode silica-based photonic crystal fibers," Opt. and Quant. Elect. **32**, 963-970 (2000).
2. Alexander Figotin, Abel Klein , “Localization of light in lossless inhomogeneous dielectrics,” JOSA A, Vol. 15 Issue 5 Page 1423 (May 1998).
3. E. Centeno and D. Felbaq, "Rigorous vector diffraction of electromagnetic waves by bidimensional photonic crystals," J. Opt. Soc. Am. A **17** No. 2, 320-327 (2000).
4. J. C. Knight, T. A. Birks, P. St. J. Russell, J. P. de Sandro, “Properties of photonic crystal fiber and the effective index modelm,” JOSA A, Vol. 15 Issue 3 Page 748 (March 1998).
5. Albert Ferrando et al , “Vector description of higher-order modes in photonic crystal fibers,” JOSA A, Vol. 17 Issue 7 Page 1333 (July 2000).
6. Chih-Sheng Chang and Hung-chun Chang, “Theory of the Circular Harmonics Expansion Method for Multi-Optical-Fiber System,” Journal of Lightwave Technology, **12** No 3, 415-417 (1994).
7. M. Wrage, P. Glas, M. Leitner, “Combined phase locking and beam shaping of a multicore fiber laser by structured mirrors,” Optics Letters, Vol. 26 Issue 13 Page 980 (July 2001).
8. Ricky K. Nubling and James A. Harrington, “Hollow-waveguide delivery systemsfor

high-power, industrial CO2 lasers," App. Opt., Vol. 34, No. 3 ,1996

9. M. Miyagi and S. Kawakami, ''Design theory of dielectric-coated circular metallic waveguides for infrared transmis-sion,'' J. Lightwave Technol. **LT-2,** 116–126.
10. Mitsunobu Miyagi , "Bending losses in hollow and dielectric tube leaky waveguides Applied Optics, Vol. 20 Issue 7 Page 1221 (April 1981).
11. S. Abe and M. Miyagi, ''Transmission and attenuation of the dominant mode in uniformly bent circular hollow waveguides for the infrared: scalar analysis,'' IEEE Trans. Microwave Theory Tech. **39,** 230–238 119912.
12. Kyung Shik Lee, Joon Yong Cho, "Polarization-mode coupling in birefringent fiber gratings," JOSA A, Vol. 19 Issue 8 Page 1621 (August 2002).
13. L. Vaissie and E. G. Johnson, "Selective mode excitation by non-axial evanescent coupling for bandwidth enhancement of multimode fiber links," Optical Engineering 41 (8), pp.1821-1828.
14. P. St. J. Russell, R. Ulrich "Grating-fiber coupling as a high-resolution spectrometer ," Optics Letters, Volume 10, Issue 6, 291-June 1985 .
15. H. Ghafoori-Shiraz, T. Asano, "Microlens for coupling a semiconductor laser to a single-mode fiber," Optics Letters, Vol. 11 Issue 8 Page 537 (August 1986).
16. Fu Yong-Qi, Ngoi Kok Ann Bryan, Ong Shing , "Diffractive optical elements with continuous relief fabricated by focused ion beam for monomode fiber coupling," Optics Express, Vol. 7 Issue 3 Page 141 (July 2000).
17. E.G . Johnson, Jared Stack, and Charles Koehler,"Light Coupling by a Vortex Lens

into Graded Index Fiber" J. Lightwave Technology, Vol. 19, No. 5, May 2001.

18. Katsunari Okamoto, "*Fundamentals of Optical Waveguides*," Paul L. Kelley, Ivan P. Kaminow, and Govind P. Agrawal. Academic Press, 2000, pp. 60-64.
19. Tanya M. Monro, "Holey Optical Fibers: An effective Modal Method," Journal of Light Wave Technology **11,** 1093-1102 (1999).
20. T. A. Birks, "Endlessly single-mode photonic crystal fiber," Optics Letters **22**, 961-963, (1997).
21. Albert Ferrando, "Vector description of higher-order modes in photonic crystal fibers," J Opt. Soc. Am. A **17**, 1333-1336 (2000).
22. J. Yonekura, M. Ikeda, and T. Baba, "Analysis of finite 2-D photonic crystals of columns and light wave devices using the scattering matrix method," J. of Light wave Tech. **17** No 8, 1500-1508 (1999).
23. J. S. Sanghera, I. D. Aggarwal, "Infrared Fiber Optics." Boca Raton, Fla: CRC press, 1998.
24. Mohammed Mohebbi et al, "Silver coated hollow-glass waveguide for applications at 800 nm," Applied optics, Vol. 41, No. 33, 20 Nov. 2002.
25. C. A. Balanis, "Advanced Engineering Electromagnetics," Welly, 1989.
26. N. Croitoru, J. Dror, and I Gannot," Characterization of hollow fibers for the transmission of infrared raiation," Applied Optics, **29** No 12, 1990.
27. Yuji Matsuura, Todd Abel, and James. A. Harrington, "Optical properties of small-bore hollow glass waveguides," Applied Optics, **34**, No. 30, 1995.

28. Mitsunobu Miyaci, Akihito Honco, and Shojiro Kawakami,"Transmission characteristics of dielectric-coated metallic waveguide for Infra red transmission: Slab waveguide model," IEEE Jornal of Quantum Electronics, QE-19, NO. **2 ,** 1983.

29. Lucas B. Soldano and Erik C. M. Pennings, "Optical Multi-Mode Interference Devices Based on Self-Imaging: Principles and Applications," *Journal of Lightwave Technology*, Vol. 13, No. 4, April 1995.

30. J.E. Zucker, K.L. Jones, T. H. Chiu, and K. Brown-Goebeler, "Strained Quantum Wells for Polarization Independent Electro-Optic Waveguide Switches," *Journal of Lightwave Technology*, Vol. 10, No. 12, pp. 1926-1930, 1992

31. M. Bachmann, M.K. Smit, L.B. Solano, P.A. Besse, E. Gini, and H. Melchior, "Polarization-Insensitive Low-Voltage Optical Waveguide Switch Using InGaAsP/InP Four Port Mach-Zender Interferometer," Proc. Conf. Optical Fiber Commun. (OFC), San Jose, CA, 1993, pp.32-33.

32. A.G. Mignani, A. Mencaglia, M. Brenci, and A. Scheggi, "Radially Gradient-Index Lenses: Applications to Fiber Optics Sensors," *Diffractive Optics and Optical Microsystems*, Martellucci and Chester, Plenum Press, New York, 1997

33. Eric G. Johnson, Jared Stack, Thomas J. Suleski, Charles Koehler, and William Delaney," *Fabrication of Micro Optics on Coreless Fiber Segments*," Applied Optics, Vol. 42, No. 5, February 2003

34. R. Olshansky, "Mode Coupling Effects in Graded-index Optical Fibers," Applied Optics, Vol. 14, No. 4, 1975

35. Katsunari Okamoto, "*Fundamentals of Optical Waveguides*," Paul L. Kelley, Ivan P. Kaminow, and Govind P. Agrawal. Academic Press, 2000, pp. 60-64.

36. D. Marcuse, BSTJ, 1977, pp 703-718

37. A. Mehta, W. Mohammed, and Dr. Eric Johnson, "Multimode Interference Based Fiber Optic Displacement Sensor," *IEEE Photonics Technology Letters*, August 2003

38. Kenji Kawano, Tsutomu Kitoh, "*Introduction to Optical Waveguide Analysis*," John Wiley and Sons, Inc. 2001, pp 41-47

39. D. Marcuse, "Theory of Dielectric Optical Waveguide," Academic press Inc.,1991.

40. D. Marcuse, " Mode Conversion in Optical Fibers with Monotonically Increasing Core Radius," Journal of Lightwave Technology, Vol. LT-5, No. 1, January 1987

41. Katsunari Okamoto, "*Fundamentals of Optical Waveguides*," Paul L. Kelley, Ivan P. Kaminow, and Govind P. Agrawal. Academic Press, 2000, pp. 60-64.

42. Milton Abramowitz and Irene A. Stegun, "Handbook of mathematical functions," Dover publications, NY,1972.

43. Toshikazu Hashimoto et al, "Spot-Size Conversion of Guided Optical Wave With Gaussian Approximation," Journal of Lightwave Technology, 21,No **10**, 2340, October 2003.

44. Z. Bomzon, G. Biener, V. Kliener and E. Hasman, Optics letters, Vol 27, No. 13, July 2002.

45. Eric B. Grann, M. G. Moharam, Drew A. Pommet, JOSA A, Volume 11, Issue 10, 2695-October 1994

46. D. Raguin and M. Moris, “Antireflection structured surfaces for the infrared spectral region,” Applied Optics, Vol. 32, No. 7, March 1993.

47. Marc J. Madou, “Fundamentals of Microfabrication,” Second Edition, CRC press, 2002.

48. Alfred Kwok-Kit Wong, *Resolution Enhancement Techniques in Optical Lithography*, Vol TT47, SPIE Press, 2001, chapter 2.

49. James R. Sheats, Bruce W. Smith, *Microlithography (Science and Technology)*, (1998 by Marcel Decker, Inc.), chapter 2.

50. Y. Fu, “Investigation of microlens mold fabrication by focused ion beam technology,” Microelectronic Eng., 56 (2001) 333-338.

51. R.J. Young et al, “Gas-assisted focused ion beam etching for microfabrication and inspection, “Microelectronic Eng., 11 (1990) 409-412.

52. Z. L. Liau et all, “Fabrication of microleneses in compound semiconductors and monolithic integration with diode lasers,” SPIE vol. 1219 Laser diode technology and Applications II (1990), 276-283.

53. Fu Yongqi et al, “Experimental study of three-dimensional microfabrication by focused beam technology,” Review of science inst., Vol 71, no 2 (2000) 1006-1008.

54. S. Rennon et al, “Nanoscale patterning by focused ion beam enhanced etching for optoelectronic device fabrication,” Microelectronic Eng., 57-58 (2001) 891-896.

55. L. Vaissie, W. Mohammed, and E. G. Johnson,”Monolithic integration of dual-layer optics into broad-area semiconductor laser diodes,” Opt. Lett. 28, 651-653 (2003).

56. J. Orloff et all, “High resolution focused ion beams: FIB and its applications,” Kluwer academic/Plenum publishers, 2002.

57. R.J. Young, “Characteristics of gas-assisted focus Ion beam etching,”J. Vac. Sci. Technol. B 11(2), Mar/Apr 1993